Malte Peter Huhnt

Concept Design of a Floating Support Structure for Hydrophilic Crop

Master's thesis

NTNU
Norwegian University of Science and Technology
Faculty of Engineering
Department of Marine Technology

Master's thesis in Maritime Engineering (Nordic Masters's Program)
Supervisor: Professor Zhen Gao, Professor Pål Furset Lader, Professor Hans Liwång
July 2019

NTNU
Norwegian University of
Science and Technology

Malte Peter Huhnt

Concept Design of a Floating Support Structure for Hydrophilic Crop

Master's thesis in Maritime Engineering (Nordic Masters's Program)
Supervisor: Professor Zhen Gao, Professor Pål Furset Lader,
Professor Hans Liwång
July 2019

Norwegian University of Science and Technology
Faculty of Engineering
Department of Marine Technology

1 Acknowledgment

This thesis is written at the Department of Marine Technology at NTNU in cooperation with the Center for Naval Architecture at KTH under the supervision of Professor Zhen Gao, who's essential guidance I am deeply grateful for. My concerns were heard at all times and met with reassuring and constructive advice. My supervision was complemented by Professor Pål Furset Lader from NTNU who held good advice and is an excellent partner for a lively debate, as well as Hans Liwång from KTH, who I could always turn to in times of slow progress.

I furthermore like to express my gratitude for the people who offered this interesting thesis proposal, Tim Staufenberger at the Ocean Farm Kiel and Marina Gebert and Sebastian Rakers at the Fraunhofer EMB Institute Lübeck. Through them I discovered a whole field of marine engineering I was previously unaware of and now fascinated by. This extends to the staff of Coastal Research & Management who allowed me to lunch with them and managed to make me see my work from a multitude of directions.

Special thanks is also given to the Nordic 5 Program and the EU-Erasmus Program allowing me to study in different places and granting me the educational freedom to set my own educational compass. The courses I could choose at KTH and NTNU gave me the practical tools and critical mindset needed to engage in such a topic.

I lastly like to thank my family who enabled me to study in the first place, not minding me being far from home, as well as the friends I made and people I met over the years, making this period of my live a fun challenge.

2 Abstract

Aquatic farming of food- and non-food products is slowly entering the public attention as growing populations and living standards worldwide drive the demand for high-quality foods. The Ocean Farm Kiel (OFK) and the Fraunhofer Research Institute for Marine Biotechnology and Cell Technology Lübeck (EMB) are hence looking into the production of various food products within the German Baltic Coast. To help support this cause is a structure operating in the Bight of Kiel designed to enable the growth of *Salicornia europaea agg.*, an eatable salt loving plant irrigated with seawater. Engineering design tools are engaged to develop a concept design which is verified by analyzing the interaction between structure, mooring system and environment using potential theory and time domain simulations. The environment at the site of operation, the fundamental methods to carry out this analysis and their implementation in the necessary tools are described. The thesis concludes with the presentation of the results gathered about the rigid body motions of the structure and the reaction of the mooring arrangement interconnected with the structure's motion characteristic. The former prove to be beneficial for the intended purpose as the motion amplification is considered low overall. The mooring arrangement too demonstrated a positive behavior as it manages to fulfill the strict layout demands while moving natural motion periods beyond the wave frequency of the worst case seastate. The mooring arrangement analysis however also revealed the mooring arrangement being unfit for seastates beyond the survival condition, challenging the concept of implementing the structure designed in more exposed locations then the Bight of Kiel.

Contents

1 Acknowledgment **I**

2 Abstract **II**

3 Introduction **1**
3.1 Thesis Outline 2

4 Introduction into Aquaculture **3**
4.1 Halophyte Farming 4
4.1.1 Salicornia europea 5
4.2 Integrated Multi Trophic Aquaculture 6
4.3 Multi-User Aquaculture 8

5 Field of Application and Operational Environment **10**

6 Conceptual Design **11**
6.1 Reevaluation of previous Concepts 11
6.2 Development of the new Concept 13
6.3 Qualitative Concept Review 15
6.4 Weights and initial Stability 17

7 Hydrostatics & Stability **19**

8 Waves **22**
8.1 Wave Descriptions 23
8.2 Design and Survival Conditions 25

9 Hydrodynamic Loads and Responses **32**
9.1 The Equations of Motion 33
9.2 Radiation and Diffraction 34
9.3 Second Order Wave Loads 35
9.4 Time Domain Simulation 37
9.5 Frequency Domain Simulation 38

10 Mooring **41**

11 Tools **44**
11.1 HydroD Modeling 46
11.2 Panel Model 47
11.2.1 Meshing 48
11.3 SIMO-RIFLEX Modeling 50

12 Resulting Intact Stability **54**

13 Resulting Linear Wave Body Interaction **56**
13.1 Response Amplitude Operators in Heave, Roll and Pitch 56
13.2 Hydrodynamic Coefficients 61
13.3 Linear Motion Response 64

14 Resulting Nonlinear Body Motions and Mooring Response **67**
14.1 Natural Frequencies of the Moored Structure 67
14.2 Time Domain Analysis 71
14.2.1 Rigid Body Motions 72
14.2.2 Mooring Line Forces 79

15 Operability **84**

16 Conclusion **85**

17 Future Work **87**

A Mooring **92**

B HydroD Drag Coefficients **93**

C RAOs in Heave, Roll and Pitch **93**

D Simulation Time Series and Spectral Results **96**

E Operability **99**

Nomenclature

Initialisms

ALC	Accident Limit State
BC	Boundary Condition
BM	Vertical Distance between COB and Metacentre
COB	Center of Buoyancy
COG	Center of Gravity
CPU	Central Processing Unit
CRM	Coastal Research & Management
CW	Clump-Weight in the Mooring Arrangement
Des	Design
DNV	Det Norske Veritas (now DNV-GL)
DOF	Degree of Freedom
dyn	Dynamic
e.g.	exempli gratia, for example
EMB	Fraunhofer Research Institute for Marine Biotechnology and Cell Technology Lübeck
EOM	Equation of Motion
ESL	Element Side Length
etc.	Et cetera, and so forth
EU	European Union
FAST	Functional Analysis System Technique
FE	Finite Element
FEM	Finite Element Method
FFT	Fast Fourier Transformation
FLC	Fatigue Limit State
GM	Metacentric Height
GZ	Righting Leaver Arm

IMO	International Maritime Organization
$IMTA$	Integrated Multi-Trophic Aquaculture
$JONSWAP$	Joint North Sea Project
KB	Vertical Distance between Keel and COB
KM	Vertical Distance between Keel and Metacentre
LF	Low Frequency
M	Metacentre
$MU-IMTA$	Multi-Use Integrated Multi-Trophic Aquaculture
MUA	Multi-Use Arrangement
N	Nitrate
NOK	Nord Ostsee Kanal, Baltic-North Sea Canal or Kiel Canal
OFK	Ocean Farm Kiel (Kieler Meeresfarm)
OS	Site of Operation where the floating structure is to be installed
P	Phosphate
PBS	Performance Based Specification
PE	Polyethylene
PM	Pierson-Moskowitz
POM	Particulate Organic Matter
RAO_{ij}	Response Amplitude Operator for the respective ij-motion
RMS	Root Mean Square
SAR	Search and Rescue
Sur	Survival
TDS	Time Domain Simulation
TLP	Tension Leg Platform, a floating platform that is tethered to the seafloor
ULC	Ultimate Limit State
UN	United Nations
WAS	World Aquaculture Society
WBI	Wave Body Interaction
WF	Wave Frequency

Symbols

α	Current Profile Shape Parameter
ϵ	Measure for Nonlinearity
η_{1-3}	Translational motions
η_{4-6}	Rotational motions
γ	Peak Shape Parameter or γ-operator
λ	Wave Length
∇	Displaced Volume
ω	Frequency
ω_j	Wave Frequency of Wave Component j
ω_p	Peak Frequency
ϕ_1	First Order Velocity Potential
ϕ_2	Second Order Velocity Potential
ρ	Water density of the water in the Bight of Kiel
φ	Random Phase Angle
ζ_a	Wave Amplitude
A_{ij}	Added Mass for the respective ij-motion
B_{ij}	Linear Damping for the respective ij-motion
c	Cosine
C_D	Drag Coefficient
$C_{D.Body}$	The Drag Coefficient applied to the Structure
C_{ij}	Restoring Coefficient for the respective ij-motion
d	Depth at the OS
F_B	Buoyancy Force
F_G	Gravitational Force
Fn_{ij}	Natural Frequency for the respective ij-motion
g	Standard Acceleration due to Gravity
H	Wave Height
H_s	Significant Wave Height

H_ω	Transfer Function, see RAO
k	Wave Number
k_j	Wave Number of Wave Component j
$l_{floater}$	length of the Floater
m	Mass
m_0	Variance
n	Number of Wave Components
s	Sine
S_{MBS}	Minimum Braking Strength
T_p	Peak Period
u_f	Friction Velocity
U_{10}	Wind Velocity 10 m above the surface
v_0	Current Velocity at the Water Surface
$v_{avr.}$	Average Current Velocity
v_{max}	Maximum Current Velocity
X	Fetch
z	Position in the Watercolumn

List of Figures

4.1 Salicornia europaea agg. growing in the wild (Musselman and Wiggins, 2013). The young shoots are especially thought after 6
4.2 The current carries POM and nutrients from the fish-cages to the subsequent products. Each of the products grown after the fish culture consume differently, ideally extracting all nutrients fed to- and excreted by the fish from the water . . 7
4.3 Example of MU-IMTA concept between a IMTA and a wind-park. Products grown in an IMTA installation are attached the wind-farm structures and profit from close coastal proximity and the existing physical and operational infrastructure 8
6.1 The two preliminary concept design. The passive-passive method is installed on the left structure, while active-wave irrigation is watering the crop on the right structure 11
6.2 The FAST method applied to a floating structure to support Salicornia 12
6.3 The advanced passive-passive concept shows the frame facilitating the floaters with the flowerbed suspended by the frame beneath a greenhouse 13
6.4 The concept ready for in-depth analysis. The top view on the bottom right show the floater layout and the growing area. The flowerbed layout is shown on the right and the side views on top. 16
7.1 An idealized ship section is shown with the positions of the COB and the COG in a neutral- and heeled condition. The heeled condition on the right shows the change of displaced volume and the GZ along with M (Rosén, 2017) 20
7.2 A GZ-curve for a conventional vessel on the left and a GZ-curve for a listing vessel on the right (Rosén, 2017) 20
8.1 The JONSWAP spectrum given three different γ values applied to a seastate of $H_s = 4\ m$ and $T_p = 8\ s$. The value $\gamma = 1$ represents the PM spectrum (DNV, 2010) 23
8.2 The comparison between a linear sinusoidal wave (dotted line) and a higher order description of a wave (solid line) which is a more accurate representation of a regular wave (Brorsen, 2007) 24
8.3 The fetch at the OS in the Bight of Kiel given east-south-easterly winds is 2.3 km (Google, 2019) 26
8.4 The wave steepness is plotted against the shallowness (DNV, 2010). The blue dot represents the design wave, the red dot the survival wave at the OS. Both waves are considered deep but highly nonlinear 27
8.5 The left graph compares the PM- and the JONSWAP $\gamma = 3.3$ spectrum for the design condition to show how the the JONSWAP spectrum is more banded than the PM spectrum. The right graph compares the same JONSWAP design spectrum against the JONSWAP survival spectrum. The comparison shows how the band moves towards ω_p of the respective condition 28
8.6 The lefthand graph compares the anual average- and max. current velocity at the OS. The righthand graph depicts the current profile in the watercolumn as recommended (DNV, 2010) 29
8.7 The wind speed profile for the design and survival condition from 10 m above the still waterline downwards 30
9.1 The six DOF surge η_1, sway η_2, heave η_3, roll η_4, pitch η_5 and yaw η_6 exemplified on a TLP (Faltinsen, 1993) 32

9.2 The dominant loads on a structure can be estimated by the relation of the wave to the characteristic dimension of the body (Faltinsen, 1993). The blue dot represents the design condition, the red dot the survival condition indicating diffraction dominated loads 35
9.3 Varying drift forces in an irregular seastate cause slow low frequency motions of the moored ship that trigger peak loads on the mooring system (Greco, 2018) . . 36
9.4 The principle of the frequency domain wave body interaction estimation is presented as an operator translating an input into an output (Rosén, 2017) 39
9.5 The response spectrum $S_R(\omega)$ on the right is the result of the interaction of the the wave spectrum $S_\zeta(\omega)$ (left) and the RAO depicted between the two (Lewis, 1989) 39
10.1 Typical mooring systems used for offshore installations (e.g. Marine Energy Devices). From left to right: Catenary system, taut line mooring system with subsurface floaters, taut line mooring- and clump-weight mooring system (Weller et al., 2013) 41
10.2 The clump-weight mooring system attached to the structure at a water depth of 12 m with the anchors being 50 m apart. The CWs quickly lower the mooring line below the 6 m threshold 42
11.1 The SESAM tools that are used in this thesis are marked with red (DNV-GL, 2019) 44
11.2 The structural model as it is designed in GeniE. The blue spheres represent the mass of the flowerbeds and the plants 45
11.3 The panel model as it is used in HydroD to calculate the linear hydrodynamic coefficients. The mean whetted surface is shown on all floaters which move together as a rigid body 48
11.4 The graph shows how the accuracy of the parameter is not significantly improving after a certain mesh refinement is reached. Further mesh refinement only increases CPU time without significantly improving the results accuracy 49
11.5 Three meshes are compared against each other on the example of RAO_{33} over the whole wave frequency range. The coarsest panel mesh with an ESL of 600 mm (blue), the medium mesh with an ESL of 72 mm (green) and the finest mesh with an ESL of 50 mm(orange) 49
11.6 The panel mesh as it is used in HydroD. The max. ESL of each element is 72 mm. A total of 23888 elements at 68029 nodes is used 50
11.7 A typical setup of a slender system in RIFLEX composed of supernodes, elements, segments and lines, taken from SINTEF-Ocean (2018) 51
12.1 The GZ curve calculated by HydroD. The righting arm is evaluated against the heeling angle of the structure 54
12.2 The righting moment (blue) is compared against the wind heeling moment in design- (green) and survival condition (orange). The later two are multiplied by 100 to follow their trend 55
13.1 The RAOs for heave (blue), roll (green) and pitch (orange) are presented for a wave coming from the negative x-direction 56
13.2 Heave motion is canceled as the heave excitation on one column is equal but opposite to the heave excitation on the column on the other end of the structure. This phenomenon is experienced if the floaters waterline center are $\frac{\lambda}{2}$, or a multiple of this, apart 57
13.3 The RAOs for heave (blue), roll (green) and pitch (orange) are presented for a wave coming with a 45°-heading onto the structure 58

13.4 The heave excitation of the two wave crests of one wave cancel with the wave trough of that same wave if the structure's floater length matches with the wavelength λ or a multiple of it . . . 58
13.5 Explanation of the rocking motion of the structure . . . 60
13.6 The RAO in pitch and roll are compared. RAO_{44} (green) is interacting with a wave coming from 90° and RAO_{55} (blue) with a wave from 0°. Both graphs are identical . . . 60
13.7 The added mass in in heave $A33$, roll $A44$ and pitch $A55$ are compared with one another . . . 62
13.8 The non-dimensional added mass in heave $A33$ is plotted alongside the non-dimensional natural frequency in heave $Fn33$. The dotted orange diagonal represents the curve where input frequency and resulting frequency are equal . . . 63
13.9 The RAO in heave $RAO33$ is plotted alongside the non-dimensional radiation damping in heave $B33$ . . . 63
13.10 The RAO in heave is interacting with the survival seastate coming at a 0°-heading. Only part of the energy contained in the seastate is transferred to the body as the peak of $S_\zeta(\omega)$ does not align with RAO33 . . . 64
13.11 The linear un-moored heave response of the floating structure to the design- and survival seastate presented in section 8.2 . . . 65
13.12 The heave response in the survival condition is compared for waves with a 0°-, a 45°- and a 90°-heading. The dominant peak of the heave response to waves with a 0°-heading vanishes almost completely as the RAO for waves coming with a 45°-heading is moved from the frequency band the survival seastate carries most of its energy in . . . 66
13.13 The roll- and pitch motion response interacting with the design- and survival seastate. The fundamentally different behavior of the roll- and pitch motion is due to the peculiar shape of RAO_{55}, causing a large response in the survival seastate and a small response in the design seastate . . . 66
14.1 One factor contributing to the restoring forces introduced to the system is the displacement of the mooring line arrangement, in this case the straightening of the mooring line and the lifting of the CW. The gray model represents the system in equilibrium and the blue model when it is forced from its natural position . . 67
14.2 The heave motion decays quickly due to the large radiation damping. Small oscillations however are slow to die down due to the absence of viscous damping of the body motions. The natural frequency in heave can be measured as $Fn_{33} = 4.783\ \frac{rad}{s}$ . . . 69
14.3 The natural period is slightly larger then Tn_{33} at $Tn_{55} = 1.493\ s$ . . . 70
14.4 Both surge and sway motion are exactly the same due to the geometry of the structure. The low frequency motions give small motions velocities resulting in a low damping . . . 70
14.5 An extract of the TDS shows the wave elevation (blue-solid) alongside the heave motion of the structure (green-dashed) together with the mooring line tension at fairlead 3 (orange-dotted) interacting with a survival seastate . . . 72
14.6 Comparison between the TDS heave response to the design- (blue-solid) and the survival seastate (green-dashed). The scatter plots in the background show the peak response spectra while the lines represent the smooth response spectra . . . 74
14.7 Comparison between the TDS heave response and the linear theory heave response of the structure interacting with a design- (upper) and a survival seastate (lower) 75

14.8 TDS surge response spectrum of the structure interacting with the design (blue-solid) and the survival condition (green-dashed) 76
14.9 First- (blue-solid) and second order wave force response spectra (green-dashed) of the design seastate. The second order wave force response spectrum is multiplied by the factor 10 76
14.10LF and WF surge motion TDS of the structure interacting with the design- (upper) and survival condition (lower) 78
14.11LF and WF surge motion TDS of the structure interacting with the design- (upper) and survival condition (lower) 79
14.12TDS of the axial force acting in line 3 at the fairlead when the moored structure is subjected to the survival condition 80
14.13The axial force response spectra on fairlead 3 are presented for the structure in the design- (blue-solid) and survival condition (green-dashed) 81
14.14TDS pitch motion response spectra of the structure in the design- and survival condition 82
14.15The most probable mean- and max. axial forces on the mooring system taken from a total of ten runs measured at the fairlead and the CW in the design- and survival condition 82
A.1 The top- and side view of the clump-weigh mooring system. The footprint is a square area of 50 m x 50 m, indicated by the anchors (arrows) at the end of the mooring lines attached at the four corners of the arrangement. The round objects depict the clump-weights and their position. The red and blue marks show where the mooring line forces are measured in each mooring line 92
B.1 The two graphs depict the default drag- and block drag coefficient curve as it is used in the HydroD intact stability wizard. The default is chosen since there is no knowledge of the drag characteristics of the structure 93
C.1 The side view of the structure shows how the floater arrangement resembles the example case in figure 13.4 in section 13.1 93
C.2 RAO_{33} for waves coming from a 0° to a 360°-heading. The structure's response distinguished only between waves coming onto the sides of the structure and the waves coming onto the diagonal. 94
C.3 RAO_{44} for waves coming from a 0° to a 360°-heading. Only the RAOs from wave directions opposing each other are identical, e.g. 0° and 180° and 45° an 225° . . 94
C.4 RAO_{55} for waves coming from a 0° to a 360°-heading. Only the RAOs from wave directions opposing each other are identical, e.g. 0° and 180° and 45° an 225°. The difference to RAO_{44} is that the RAO_{55} is 90° phase shifted to RAO_{44} 95
D.1 The full TDS omitting the transient phase ($0s - 400s$) is presented for the wave elevation (left) and heave motion of the structure (right) in the survival condition 96
D.2 Comparison of the design and survival JONSWAP wave spectra as are generated by SIMO 97
D.3 The surge response spectra for the structure interacting with the design- (blue-solid) and the survival condition (green-dashed) 97
D.4 Comparison between the first order wave forces of the design- (blue-solid) and the survival seastate (green-dashed) 98
D.5 Full time series of the line tension in mooring line 3 interacting with the survival condition 98
D.6 The mean- and maximal period of the axial force in fairlead 3 subjected to the design- and survival condition 98

E.1 The heave acceleration spectrum of the structure subjected to the survival condition 99

List of Tables

4.1 Potential use of halophytic plants, divided into the two main applications: environment shaping and product growing (Ventura et al., 2015) 5
6.1 PBS with weightage (Huhnt, 2018) 17
6.2 Mass and initial stability attributes calculated from the mass-table prepared with Excel 18
7.1 IMO intact stability requirements taken from DNV (2011) 21
8.1 Design and survival criteria for wind and waves 26
10.1 Mooring line lengths used for the present mooring arrangement 43
11.1 The environmental information used for the HydroD intact stability calculations 46
11.2 Mooring line component specifications as specified by Engel-Netze (2019) 52
12.1 The design loadcase as it is calculated by Excel and HydroD 54
12.2 The characteristics from the GZ curve in figure 12.1 compared against the IMO intact stability requirements taken from DNV (2011) 55
13.1 The linear hydrodynamic coefficients C_{ij} and M_{ij} 62
14.1 The resulting natural periods and -frequencies from the numerical motion decay test in heave, pitch, surge and sway 71
14.2 The presented parameters govern the simulation procedure in SIMO-RIFLEX . . 71
14.3 TDS global motion response in the ULS and the design case, averaged from ten TDSs 73
14.4 The RMS of the exact wave spectra and the ones generated by SIMO respectively 73

3 Introduction

Saline agriculture is a field of growing importance in recent years with the global effects of climate change becoming increasingly visible. One billion hectares are already salinized globally and growing at a rate of 10 Mha per year, rendering this land useless for conventional agriculture, since the cultivation of standard food crops on salinized soil is only possible within limits or not possible at all (Hamed et al., 2014). Together with the steadily growing population worldwide who demands increasingly more space due to the thriving living standards, the competition for land is becoming intense. The United Nations (UN) estimate that 40% of the population live no further then 100 km from the next shore (Crossland et al., 2005), intensifying competition for coastal land. Finding ways to deescalate the competition for inhabitable land while still increasing the food production is hence a challenge taken up by many players world wide, including the UN and the European Union (EU).

The idea of saline agriculture emerged in the second half of the 20th century illustrating that the problematic of salinized soils forcing today's farmers into the direction of farming salt loving plants is a fairly recent one (Ventura et al., 2015). There is a high research demand for growing crop on salinized soil but also to use seawater to irrigate the crop, since seawater is a resource available in abundance compared to freshwater, given that the majority of the planet is covered with seawater. The OFK, a private enterprise focusing on the sustainable use of the ocean for the environmental friendly production of food products, along with the EMB is hence seeing possibilities in developing floating farms to produce halophytic crop.

The EMB is part of the life sciences group within the Fraunhofer Gesellschaft focusing on the development of new technologies in the fields of cell technology and aquatic biotechnology. The involvement of the EMB in this project is due to their focus on the utilization of organisms from marine aquaculture for the food- and biotechnology industry and they are involved here in the biotechnical aspect of choosing the correct crop to grow and on how to process the crop to further direct it to commercially beneficial applications on the market. The high research demand encouraged the OFK and the EMB to engage the challenge of growing food-products on the water together and to cooperate in a scientific study examining the possibility to grow *Salicornia europaea agg.* on floating structures in the Bight of Kiel, irrigated with seawater. Salicornia is a halophyt, a plant that is dependent on salinized soil to grow. The use of Salicornia covers a wide range, from bio-fuel potential to live-stock fodder. The OFK is nevertheless focusing on the cultivation of Salicornia for human consumption, since its core business is the marketing of locally produced seafood. The additional benefit is the uptake of nutrients by the plants, which has a positive influence on the levels of fertilizers dissolved in the Baltic See, as the high concentration of fertilizers results in its eutrophication with negative consequences for humans and marine life.

This new undertaking demands for new infrastructure to be developed and installed in the Bight of Kiel, which poses a challenge for both partners, since both have only limited knowledge of marine engineering and are hence dependent on out-of-house expertise. The development of a structure to support halophytic crop is therefore the focus of this master thesis. The design of the structure includes the optimization of the shape and dimensions in order to best support the crop as well as to analyze the design reached in terms of the stability-, motion- and mooring response characteristics to a defined environment. This can only be achieved by analyzing the fundamental mechanisms at work to get a good understanding of the tools used in order

to generate the performance characteristics of the proposed structure. The assessment of the structure hence engages the majority of marine engineering tools such as hydrostatic stability, wave body interaction and mooring system analysis, although detailed structural integrity- and hydrodynamic flow analysis are omitted. Instead other tools are applied, which are usually beyond the average marine installations design spiral, namely concept development techniques used to optimize the conceptual draft of the structure and to assure that the structure is fulfilling vital demands.

The work culminates into a description of the fundamental interaction between the environment, the structure and the mooring arrangement enabling a sound judgment of how- and in which operational context and environment the structure can be used. As it is desired by the OFK and the EMB the concept is worked out in great detail, already in correspondence with the manufacturer, to quickly build and install the structure. Hence is the present work already giving leads on which mooring hardware to use, the general dimension of the greenhouse to be used to improve growing conditions and which points are critically loaded with which force, e.g. the fairleads. However, the task to describe the structure in full detail was not achieved. Important factors and mechanisms exceed the scope- and time available for this thesis resulting in the negligence of the flowerbeds throughout the calculation and of the viscous damping on the structure. These and similar shortcomings are considered at the end of this work.

3.1 Thesis Outline

The thesis is structured into four parts of varying length. The first part presents the framework the structure to be designed will be working in, namely an introduction into aquaculture and halophytes. A short history of aquaculture, the description of the plant to be cultivated as well as the operational concepts the structure is integrated in and the purpose it serves are laid out.

The second part deals with the concept development of the structure. Section 6 covers the development history the concept has gone through and thereby summarizes the preceding project thesis. Previous designs are evaluated based on what was learned working at the OFK and on the concept development tools already used in the project thesis. A design capable of fulfilling the demands is presented to subsequently be analyzed in depth.

The adjacent work focuses on laying out the methods used to describe the interaction between structure and environment. This is the largest part of the present work and compromises sections 7 through 11. It covers the description of the environment and its effect on the structure, the methods of estimating and quantifying the interaction between environment and structure as well as an introduction into mooring analysis. The end of this part concludes the description of the tools used to apply the methods previously described on the specific problem of the wave body interaction.

The presentation of the results gathered constitutes the last part of the thesis. The rigid body motion characteristics are presented alongside the causes for specific motions of the structure. Two different methods are used to generate results which complement one another to accurately describe the interaction between the moored structure with the environment. A break down of these results and their effect on the structure's implementation and operation concludes the work. Lastly are impulses for future work presented covering important topics neglected by this thesis.

4 Introduction into Aquaculture

Aquaculture describes the production of products in an aquatic environment, be it on land based installations or in an marine environment. This excerpt is disregarding the advancements made using land based facilities for aquaculture and concentrates on the marine applications of aquaculture, as the structure being designed is intended for marine operations. The following introduction to aquaculture and halophyte farming as well as the description of aquaculture techniques are taken from the precursor report *Preliminary Concept Design of a Support Structure for Hydrophilic Crop* (Huhnt, 2018) written by the author and intended as a description of the framework the structure to be developed is planned for and supposedly operating in.

The variety of products produced in marine aquaculture is divided in two groups: Algae and seafood. The use of these products is as diverse as the amount of products grown in aquaculture around the globe ranging from food products over cash crops to fodder and biofuels. Some products, for example algae, can furthermore be grown as bioremediation in contaminated areas to clean up fertilizers or greenhouse gases. High expectations boost aquaculture making e.g the kelp production one of the fastest growing industries in western countries (Buck et al., 2017). The continuous search of an ever growing world population for new protein-sources and healthy food-supplements is driving aquaculture, leading to an increase not only in size but in product variety and output.

Where agriculture has taken thousands of years to transition from a hunting and gathering approach towards the wide-spread implementation of farming techniques, aquaculture has made this transition in just two generations. Till recent years most of the seafood supply came from fish travels, catching seafood globally using rather less sustainable fishing techniques. Today, half of the worlds seafood supply is coming from aquaculture (Holm et al., 2017). A shift in the marine industry can currently be witnessed, away from conventional fishing methods towards aqua-farming of all kinds of products, a change in its dimensions similar to the change currently taking place in the energy-production industry. For some it marks the long awaited change away from outdated techniques towards a more responsible use of the ocean resources, while others fear the mutilation of coastal areas and a devastation of local flora and fauna.

Since the widespread implementation of modern aquaculture in the 1960s, especially in South-East Asia (Buck et al., 2017), has aquaculture spread to the world. The challenges experienced and scientific progress have led to the creation of the World Aquaculture Society (WAS), bringing together scientists and producers. Although the cooperation is mostly symbiotic, friction arises regularly due to the different aims of the players involved (Holm et al., 2017). This becomes evident when looking at the future threads to the industry: the decreasing availability of space due to the increased utilization of the ocean by different stakeholders (shipping companies, oil companies, environmentally protected ares, etc.), the visual deterioration of the coastal areas due to aquaculture installations as well as the delusion of fodder and pharmaceuticals into the water to name a few. The potential negative effect on the environment from the widespread use of antibiotics and excrement from aquaculture is still little investigated and a threat to the ecosystem, the public acceptance of aquaculture and therefore to the industry itself.

4.1 Halophyte Farming

The steady population increase, especially the population growth in coastal proximity, leads to a generally growing demand of food products, particularly in coastal areas (Crossland et al., 2005). This demand is hard to meet as arable land in proximity of metropolitan areas grows increasingly scares due to the growing demand for urban land. The later problem can furthermore be intensified by salinized soil, as some countries in Central America and the Middle East had to realize, as salinized soil further decreases agriculture land in coastal- and metropolitan proximity. One billion hectares are salinized globally, an area that is growing at rate of 10 Mha per annum (Hamed et al., 2014). Furthermore is conventional agriculture of regular food crops, such as wheat, still not feasible on soils with a too high salt content, contrary to the high hopes that were put into the development of salt tolerant conventional food crops (Ventura et al., 2015). One solution is to turn to already salt tolerant crops instead, rather then developing conventional salt tolerant crops using wildly criticized techniques such as gene editing.

Halophytes, land based plants with the ability to grow in salinized conditions where conventional crops fail to grow, could however ease this dilemma. Halophytes are generally distinguished into two types: Faculative- and obligate halophytes. While the later prefer salt-free environments but are able to put up with salt-conditions when neccessery, obligate halophytes are dependent on salt in their direct surrounding to survive (Hamed et al., 2014). The search for halophytes which could be of use to humans is hence being pursued with increased vigilance, as food, cash crops or other applications. Although the concentration of salt a plant is able to tolerate varies strongly, even within one family of plants, several halophytes have been found that tolerate increasingly high levels of salt. The HALOPH database for example lists a total of 78 plants that are able to withstand 100% seawater (Ventura et al., 2015). This is beneficial not only for farming on already salinized soils, but also for farms, where salinized soils and the absence of freshwater is only allowing for irrigation with seawater. The plant does not only profit from the water but also from the dissolved nutrients. Hamed et al. (2014) have shown that almost all vital nutrients (11 out of 13) are existent in sufficient amounts in seawater.

However, the disadvantage halophyte agriculture has compared to conventional agriculture is the absence of a centuries long history of crop- and farming techniques refinement. Conventional agriculture is the result of taming the disorderly growth of certain plants delivering a fruit. Humanity has been able to master this art by strict growing techniques, optimal irrigation, and, since the 20th century, the large scale utilization of highly potent fertilizers. Furthermore were crops domesticated by selection and crossbreeding, emerging in an increasing yield per harvesting cycle and allowing for more harvesting cycles per year as the plants were grown under ideal conditions. Although halophyte agriculture is just at the beginning of this development the potential is large, given the already mentioned increase in salinized soil as well as the growing demand for high-quality food products. The prize fluctuation of globally traded food products could encourage countries with vast areas of salinized soil to explore the potential of halophyte agriculture as it would support the domestic food production, thereby making the country in question less disposed to the fluctuation of the global food speculation. The increased demand of high-quality food products, especially of so called health-foods, such as quinoa, is furthermore boosting the potential of halophyte farming (Huhnt, 2018).

The number of areas formerly reserved for conventional food crops halophytes are slowly finding their way in is staggering, as research continues. The coarsest division to make when elaborating

on the use of halophytes is between environment shaping- and commodity producing halophytes. The later describes the conventional growth of products, where the biggest economical potential of halophytes lies. The production of high-quality food products, as mentioned above, but especially the large scale production of cash crops and animal feed promise large revenue. Cash crops can be used to produce bio-fuels, something that is already pursued with conventional crops, such as corn and canola. However the biomass- and oil-seed yield per hectare is still small. Furthermore is the harvesting-cycle comparably long and the harvesting technique connected with several mechanical difficulties. The absence of matured growing protocols is also a major obstacle of economically feasible growth of halophytes as cash crops (Ventura et al., 2015). In contrast to this is the use of halophytes as fodder for animals more promising. The high salt concentration of halophytes is indeed an obstacle for conventional live-stock, which is however not a problem for fish. Fish in fish-farms have a generally higher tolerance to the salt content of their feed, making halophyt fodder a serious alternative for conventional fodder (Ventura et al., 2015).

Besides the local production of high-quality food products is the other use of halophytes targeted in the project this thesis is contributing to, the use of halophytes for bioremidation. The later is one of the big advantages the production of halophtes has over conventional crop. Halophytes can, to a certain degree, rid the soil they are growing in from salt, making this soil available for non salt tolerant plants (Hamed et al., 2014). Furthermore are halophytes, as most other plants, consumers of nitrate (N) and phosphate (P), the main components of fertilizers. Fertilizers lead to a multitude of problems, especially as much of the fertilizers used in agriculture get washed into the world oceans. The resulting algae blossom leads to a chain of undesirable consequences the marine environment and local communities are suffering from (Buck et al., 2017). Not only can the algea be toxic to the humans, but the eutrophication of the water can lead to a drop of oxygen in the water endagering oxygen relying fauna in the water, especially if the body of water is small as is the case in the Baltic Sea. Reducing nutrients in the water is hence vital for the health of a marine ecosystem. Bioremidation and other potetntial uses of halophytes, such as the cultivation of ornamental plants, is summarized in table 4.1 taken from Huhnt (2018).

Table 4.1: Potential use of halophytic plants, divided into the two main applications: environment shaping and product growing (Ventura et al., 2015)

Commodity Producing Cash Crop	Food	Environment Shaping
Biofuel/oil-seed crop	Oil-seeds deliver high quality fatty acids	Bioremidation of polluted areas
Forage for live-stock	Vegetables for human consumption	Diversifying habitats
Ornaments	Probiotics to improving digestion	Consume CO_2

4.1.1 Salicornia europea

One possible halophyte which growth should be supported by the here described structure is the halophyte *Salicornia europaea agg.*, commonly known as *Glasswort*. It can be summarized when following the preceeding project thesis that Salicornia grows in salt marshes and tidal zones all over the European central northern coasts. Salicornia flowers in August, its seeds ripen in September and it grows to be about 0.3 m tall (Yvonne et al., 2011b). Further is the plant

submerged twice a day by the tide, given its location in tidal marshes (Staufenberger, 2018b). The delicate nature of its brittle shoots require protection from strong environmental loads such as wind and waves, as the shoots could break of. Its frailness and the absence of established growing and harvesting protocols make it furthermore necessary to handle the plant manually (Staufenberger, 2018a).

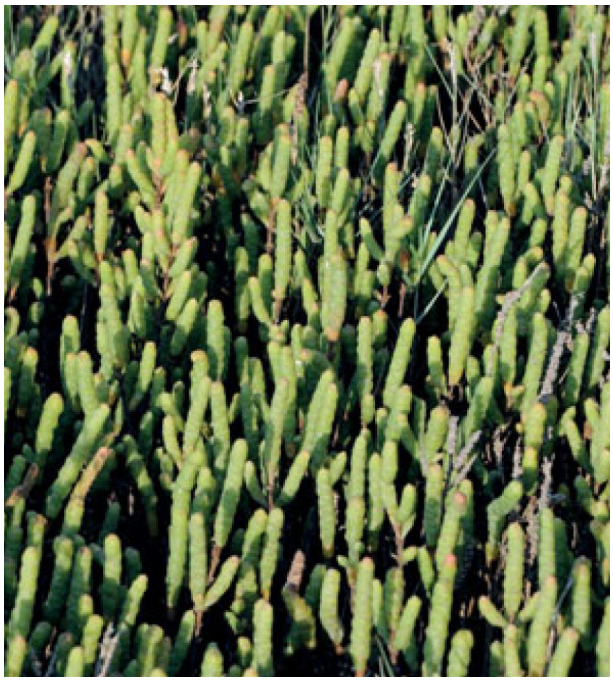

Figure 4.1: Salicornia europaea agg. growing in the wild (Musselman and Wiggins, 2013). The young shoots are especially thought after

The plant is chosen for its eatability and exemplary nutritional values: It has a $17 - 21\frac{mg}{g}$ total lipid contend, with 48.2% being $\omega 3$ fatty acids. The nutritional value together with the trend towards a healthier diet in developed countries might hence promote the demand for Salicornia further (Yvonne et al., 2011a), which could be well met by the year round availability of the plant (Ventura et al., 2015). Salicornia has long been an integral part of both the British and the Dutch cuisine, usually as a salad or served alongside seafood. The plant is already today sold for comperativley high prices as the *vegatable of the sea* or as *sea beans* on european markets (Ventura et al., 2015). To give an example: 1 kg sea beans is sold by an online vegetable delivering service for 30 $\frac{\$}{kg}$ (Delights, 2018). Abdelly et al. (2010) furthermore reported a biomass yield for Salicornia of about 20 t per hectare and a seed yield about 2 t per hectare, emphasizing the large economical potential of this crop, once growing techniques are furthermore refined and established.

4.2 Integrated Multi Trophic Aquaculture

Aquaculture is globally dominated by mono-cultures, the farming of one species on a more or less large scale. Furthermore the total variation of species raised in aquaculture is relatively small, coming down to only a couple fish species, such as salmon and other seafoods such as shrimp and mussels (Holm et al., 2017). The negative side effects of this practice are analogous to the consequences mono-cultures have in conventional agriculture: vulnerability to diseases,

degradation of the local environment and reduction of biodiversity (Altieri, 2016). There are nevertheless approaches to drive aqua- and agriculture towards a more sustainable future by making use of *synergy effects* between different species and products. The aim of Integrated Multi Trophic Aquaculture (IMTA) is to make use of these synergies by growing different species that are in a desired symbiotic relationship side by side or above and underneath each other. One species will help build a beneficial environment for its neighbor and the other way around.

Synergy effects are met in many different constellations throughout nature. The one this structure is aiming to exploit is not the direct interaction between different species but how the individual species support a beneficial environment of the other species by consumption and defecation. Knowledge about digestive behavior of the flora and fauna being produced is hence vital. Aquacultural products are differentiated into two groups: extractive species and fed species. The later species, such as fish, rely heavily on the supplement of undissolved fodder in the form of particulate organic matter (POM), which is given into the fish-cages to be (mostly partly) taken up by the fish. Extractive species on the other hand act as living filters and draw all the necessary nutrients from their surrounding by filtering the water. Extractive species are again differentiated into three groups: (a) filter feeders, such as mussels feeding on small POM, (b) deposit feeders, such as sea cucumbers feeding from whatever POM that sinks to the bottom and (c) dissolved nutrient absorbents, such as algae that feed from the nutrients dissolved in the water (Buck et al., 2017).

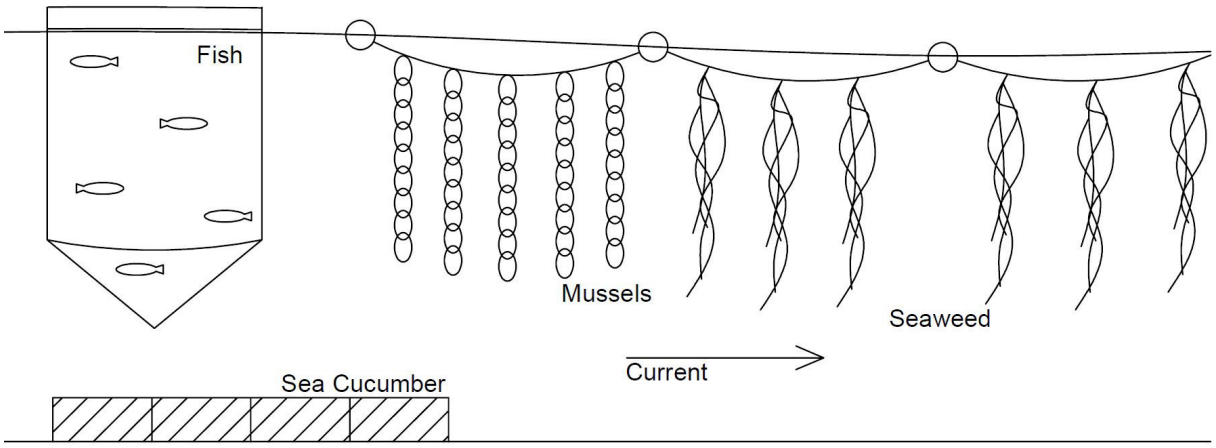

Figure 4.2: The current carries POM and nutrients from the fish-cages to the subsequent products. Each of the products grown after the fish culture consume differently, ideally extracting all nutrients fed to- and excreted by the fish from the water

Figure 4.2 shows an exemplary IMTA arrangement that utilizes similar synergies as the one used in this thesis. The fish will be fed with large POM that will partly be directly consumed. Whatever sinks down, not consumed fish feed and the POM excreted by the fish, will be taken up by the sea-cucumbers. Smaller POM and water solvent nutrients excreted by the fish and sea-cucumbers are carried by the dominant current to the mussels which are consuming the POM and lastly to the seaweed, which rid the water from nutrients by absorbing N and P. This set up could be able to generate large amounts of seafood without adding additional fertilizers into the water, given that the amount of products are in the correct relation to each other[1].

[1]Further Information on the species-ratio see S. Haas et al. (2015) (German)

4.3 Multi-User Aquaculture

Multi-use arrangements in aquaculture have been around since the 1990s with Germany starting its first sea trial of Multi-Use Aquaculture (MUA) arrangements in the north sea, followed soon by Russia, the Netherlands, France, Norway and the United States (Holm et al., 2017). MUA arrangements have since gained public attention, especially since offshore wind parks begin to cover vast areas of coastal waters all over Europe. The concept utilizes a similar concept as the IMTA, since it is making use of operational synergies between applications sharing the same site. A good example is the co-location of an oil rig and a fish farm. The oil rig is serving as an anchor point and operational platform for the fish aquaculure, while the oil rigs personal is profiting from the fish produced by the fish- aquaculture, a concept already tried in the Caspian Sea in 1988 (Lovatelli et al., 2016). This example shines light on the second advantage of MUA applications; the utilization of otherwise blocked spaces in proximity of the consumer. The growing competition for space, especially in coastal waters, makes this advantage noteworthy. Buck et al. (2017) emphasize that the ocean surface is already used to a greater extent as one might think: oil and gas infrastructure, subsea-cables and pipelines, shipping routes, fairways, marine-mammal migration routes, migratory bird flyover routes, fishing grounds and environmentally protected areas are all competing for space.

This competition for space, aggravated by the expansion of wind-parks as well as the foreseeable decommission of oil-rigs in the North Sea, drive the development of MUA applications. Wind parks are especially well suited for aquaculture or IMTA given their large extend and the absence of shipping routes. Especially wind-parks are placed in good coastal proximity, making frequent monitoring and short supply chains feasible. Figure 4.3 depicts a multi-use integrated multi trophic aquaculture (MU-IMTA) concept between a schematic wind-park and an IMTA. The products grown, such as fish, algae and mussels, are connected to the structures already implemented to harvest the wind energy.

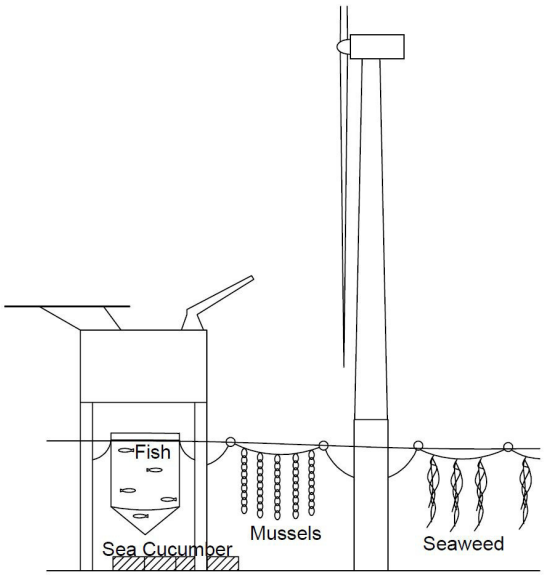

Figure 4.3: Example of MU-IMTA concept between a IMTA and a wind-park. Products grown in an IMTA installation are attached the wind-farm structures and profit from close coastal proximity and the existing physical and operational infrastructure

A substantial amount of studies of MUA in research-scale have already been made close to- as well as off-shore that have shown that the high-energy environment is currently the biggest technical challenge to overcome. High seas, wind- and current loads have led to loss or damage of either the installations or the product, one of many problems that are currently preventing the wide spread application of offshore MUA (Holm et al., 2017). The growing focus on offshore installations for both aquacultural- and energy production have nevertheless led to an optimism that these challenges can be overcome in due time.

5 Field of Application and Operational Environment

The OFK and the EMB have agreed to cooperate in a project to grow Salicornia in the Bight of Kiel by operating the structure that is to be designed and evaluated in this thesis, employing both MUA and IMTA principles. The structure's purpose is not to only grow Salicornia but also to act as a nucleus for a variety of application. The primary ambition is the production of high quality foods, in this case Salicornia, without the use of fertilizers, otherwise arable land and fresh water, since the plant is growing on otherwise unused space and the seawater the crop is irrigated with contains all nutrients necessary. Hence is the primary aim to enable the growth of Salicornia.

Further applications are however intended for the structure. The MU-IMTA profile of the structure is sharpened when considering the additional products the structure is to support or interact with. Primarily will the structure be integrated in the already existing mussel- and algae farm infrastructure. The structure will in that respect act as an operating platform to aid the harvesting and monitoring of the mussels and algae. There is furthermore the idea to grow mussels underneath the farm, as mussels are relatively independent from sunlight, making use of the water column beneath the structure. This however is intended for a later stage, as there is no existing procedure on how to grow and especially harvest the mussels growing under the farm.

The product which is already scheduled to grow in direct interaction with the farm is *Pistia stratiotes* or *water cabbage* and similar plants. Pastia is capable of entrapping air into the cells of its roots, once a certain growth stadium is reached, allowing it to float on the water-surface without attachment to the seafloor (Staufenberger, 2018a). The farming of water cabbage is not intended for human consumption but purely for the extraction of nutrients. The produced biomass is harvested and can subsequently be refined further, e.g. into bio-fuels. The planting is done on floating mats made of reed to allow for buoyancy during the plants infancy. These mats are attached to the structure and act as supports for Pastia until these are sufficiently buoyant on their own. The mats will later sink down to the seafloor as they soak up water and start to decompose.

The third mayor function the structure must fulfill is that of a research platform. The co-operation with the EMB is based on the prerequisite that the structure can be used to carry out- and monitor experiments. The EMB wishes to optimize the farming protocol of different plants to develop their potential as food, fodder and biomass while contributing to a balanced nutrient budget in the Baltic Sea. The structure must hence be highly modular and allow for changes of the applications attached while at the same time offering enough space for extensive research equipment. Ergo are the motion characteristics of the structure in a marine environment vital to allow for unhindered operation of the farm and the experiments.

6 Conceptual Design

The design of a working concept is the first step which simultaneously has the biggest impact, since it sets the direction, the strategy, on how to fulfill a given task as good as possible. A fundamental change of the concept at a later stage is costly and possible only within limits, as was pointed out in greater detail by the previous project report (Huhnt, 2018). The concept is furthermore tightly interacting with the environment it is subjected to and the operation it is designed for. Both have a fundamental effect on the design and decide if- and to what extend the design is a success. The difficulty at this stage is hence to come up with a design which offers the possibility to be adjusted at a point in time, where the details of the now still unfamiliar operation emerge. Modularity and applicability are therefore important approaches to keep in mind during the concept design.

6.1 Reevaluation of previous Concepts

The observation of the environment around the farm and the experiences made working on the farm quickly revealed that a revision of the designs reached in the preceding work is necessary. To recall: two concepts were presented, shown in figure 6.1. The passive-passive irrigation system on the left working with partly submerged flowerbeds and the active-wave irrigation concept on the right utilizing the waves passing the ocean farm to irrigate the plants. Both ensure a permanent water-exchange in the substrate of the flowerbeds, the former by the passive water particle circulation in and out of the flowerbeds, the later by active wave-wash to the flowerbeds from underneath.

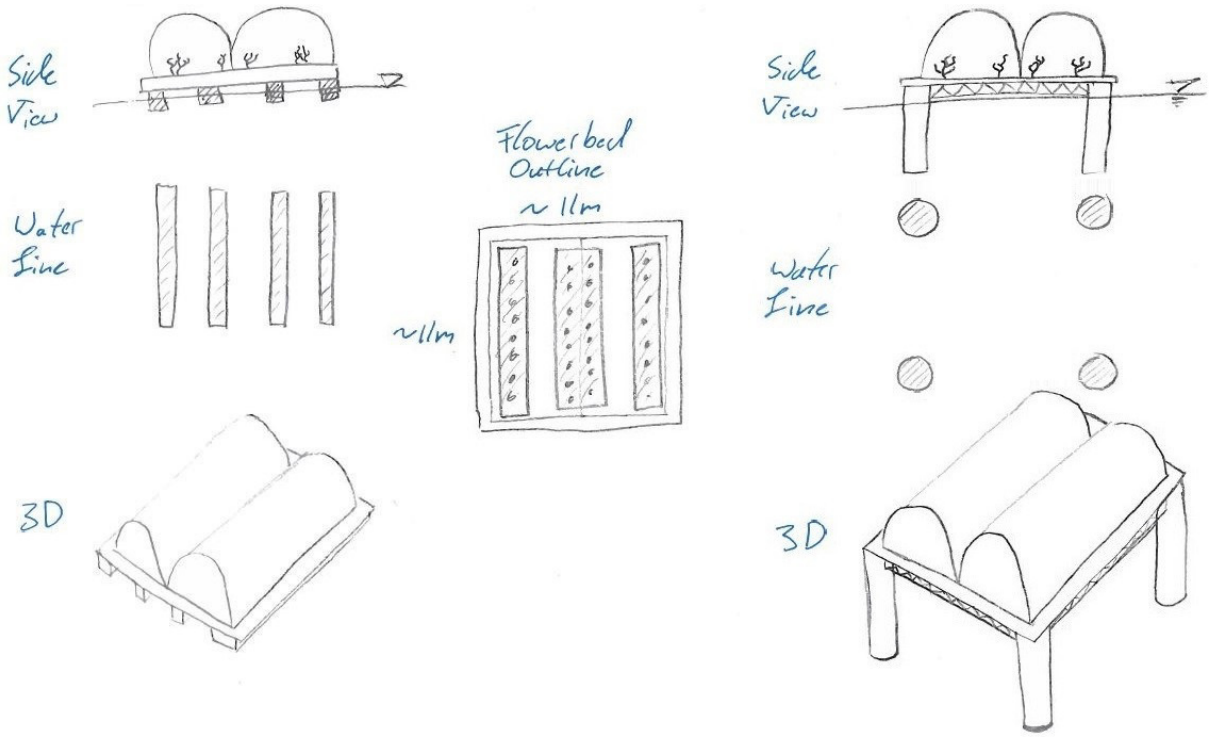

Figure 6.1: The two preliminary concept design. The passive-passive method is installed on the left structure, while active-wave irrigation is watering the crop on the right structure

Both concepts proved to be unfeasible after examining the conditions at the farm with respect to the structure. Multiple shortcomings lead to a redesign of the concepts but can be reduced to two main factors: A false estimation of the environmental conditions at the site of operation (OS) and a too high complexity of the structure, ergo too high manufacturing costs. The active-wave irrigation relied on waves frequently passing the platform to assure an adequate water supply to the flowerbeds. The wave crests would wash water to the substrate of the plants as they pass under the flowerbeds. This constant, periodic and predictable wave was to be generated by the seastate itself but especially by the passing pilot vessel, servicing the vessels entering the Baltic-North Sea Canal (NOK). However the seastate did proof to be much more diverse, with only limited waves of noticeable height for days, even though the observations where made during the winter season, which is usually the time of the roughest seas during the year. Furthermore was the passing of the pilot vessel far less frequent then expected and not predictable, since only the minority of vessels entering the NOK rely on pilot-assistance.

The failure of this design can be illustrated by referring to the Functional Analysis System Technique (FAST) analysis conducted in the preceding project report. The FAST diagram in figure 6.2 depicts the critical path, the backbone of any structure which is to be developed. The FAST diagram shows a collection of critical functions the design has to apply to in order to be functional. The individual functions are related with *How-* and *Why-* statements. The function to the right of a given function has to answer the *How-* question, while the function to the left has to answer the *Why*-question. This chain connects lower order functions with higher order functions, here supporting Salicornia. It becomes obvious when applying this strategy to the active-wave irrigation concept that this strategy violates the *provide water* function, which is indispensable for the next function *Grow Salicornia*, and so forth. The concept is hence not in agreement with the critical path.

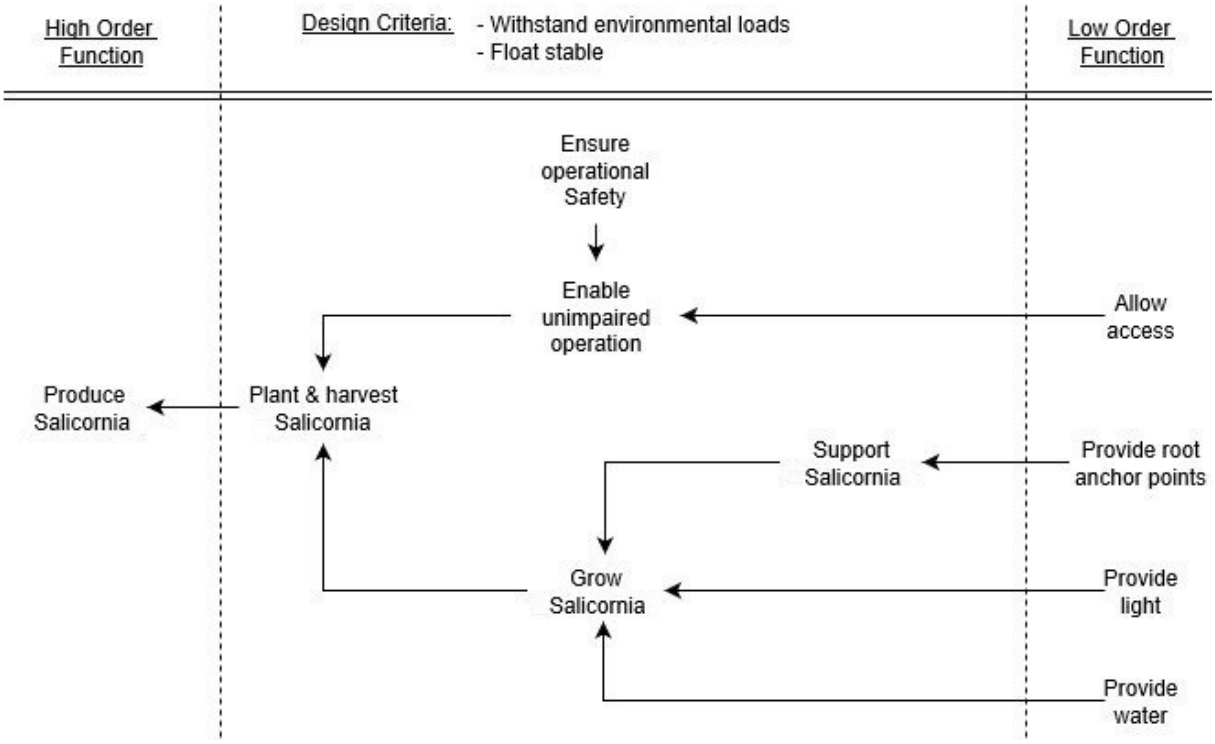

Figure 6.2: The FAST method applied to a floating structure to support Salicornia

The comparably high complexity of the design was another hindrance for the active wave irrigation. The manufacturer of the existing infrastructure at the farm is specialized in the construction of floating peers and pontoons for the yachting industry but has no experience with advanced floating structures. Hence would an elaborate design, such as the column stabilized structure, be a challenge to construct and accordingly expensive. The circumstance that the project for the bioremediation of the Baltic, this structure also is constructed for, is financed merely by scientific funds, led to disregarding the active-wave irrigation. The exclusion of the active-wave irrigation concept hence led to a more detailed analysis of the passive-passive irrigation concept.

6.2 Development of the new Concept

The wrong prediction of the environmental conditions rendered the active-wave irrigation concept unfeasible. The creative development process hence focused on developing the passive-passive irrigation system further. This concept focuses on the passive irrigation of the flowerbeds by the surrounding seawater. The particle movement on the surface ensures a sufficient water exchange so the water in the flowerbed does not become moldy. Different design concepts where sketched up and compared to one another, eventually leading to a frame-based design with walkways accommodating the floaters surrounding a growing area. The flowerbed is supported by the frame and can be altered in height, ergo grade of submergence, by either ballasting the floaters within the frame (crude manipulation) or changing the suspension-height of the flowerbed, a mechanism not described in greater detail here. A further iteration loop led to a downsizing of the structure. Instead of providing the 25 m^2 growing area demand on one structure, two structures with a growing are capacity of 12.5 m^2 each supply the required growing area. Figure 6.3 shows the advancements in developing the passive-passive irrigation concept. The flowerbed is suspended by the frame facilitating the floaters. The dimensions of the frame is already in vague agreement with the dimensions of the standard pontoon sub-structures of the manufacturer.

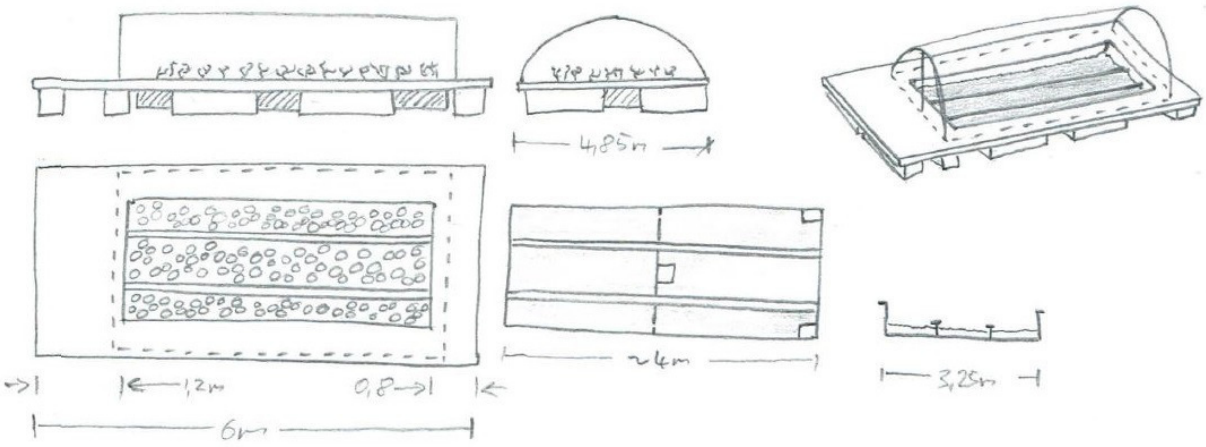

Figure 6.3: The advanced passive-passive concept shows the frame facilitating the floaters with the flowerbed suspended by the frame beneath a greenhouse

This change in design has multiple advantages compared to the previous concept illustrated in figure 6.1 and discussed in Huhnt (2018):

- The global bending moment in the frame is reduced as girders in the flowerbed carry part of the bending moment

- The individual parts the frame is made up from are smaller and hence easier and more cost-efficient to transport
- The higher modularity of the two structures together allows parallel testing of multiple farming techniques

The design as it is shown in figure 6.3 was further revived by multiple stakeholders within the operation. The first critic was Nikolai Nissen, head of operation of the OFK, who I interviewed concerning the accessibility of the farm (Nissen, 2019). His involvement led to a reconsideration of the accessibility of the flowerbeds as well as a reevaluation of the compartment referred to as *working platform* at the front of the structure. The later should be of sufficient size to enable loading and unloading of crop and sere as a storage area for research equipment to monitor the growth of marine products within the pontoon and the surrounding farm. The accessibility concept of the growing area was furthermore adapted as the crop needs to be easily and comfortably accessed, since planting and harvesting will be done by hand. First was the idea of one flowerbed only discarded in favor of multiple independent flowerbeds within the growing area. Further is the maximum depth a person can reach out set to 80 cm and the minimum walkway-width to 60 cm to make a comfortable working position possible. The walkway-width might seam wide, but it makes for safe movement in between the flowerbeds. The damage done when accidentally stepping on the plants during operation is seen as greater then the slight reduction of flowerbeds due to the higher space demand of the walkway.

The meetings that followed was with the the manufacturer AluBau GmbH in Büdelsdorf as well as with the EMB. The former meeting had the greatest impact onto the design. AluBau GmbH uses a patented concept of extruded aluminum-beams which are fit with groves to simply connect features, such as hand rails, to the outer and inner perimeter of the sub-structure. Those beams are manufactured with a standard length of 6.15 m which are assembled to pontoons with the dimensions 6.15 m $*$ 1.63 m. Each of these sub-structures is equipped with four floaters. Together make four sub-structures the frame. The way of arranging the sub-structures in this manner was envisioned together with Marina Gebert, Sebastian Rakers and Sebastian Kärst from the EMB. An important advantage of this arrangement is that each pontoon sub-structure is individually stable. The four sub-structures can be floated to the construction site and assembled at the OS, which would not be possible with the concept from figure 6.3, since the narrow gangway parts on the long sides of the structure would capsize when floating. The resulting gross growing area (including walkways, flowerbeds and gaps) spanned by the four sub-structures is 4.52 $m*$ 4.52 m $=$ 20.43 m^2. This is important since the maximum span of a standard greenhouse arch is 4.5 m, making a pricey custom greenhouse solution obsolete.

The farming technique utilized to grow Salicornia as well as the layout of the flowerbeds was discussed in greater detail with Martina Mühl, project leader Baltic Blue Growth at OceanBASIS and Marina Gebert along with Sebastian Rakers at EMB. The questions discussed with Martina Mühl where focusing on the growing technique of the crop, in particular about the water-demand and substrate configuration of Salicornia. The results are two techniques which are to be established alongside each other: the first one uses small flowerpots filled with ceramic granulate which are arranged in a grid and placed into the flowerbeds. The ceramic granulate, similar to the granulate used in conventional decoration plants in office spaces, allows the roots of the plant to attach and the water to migrate to the roots. The flowerpots on the other hand prevent the substrate from being washed out, away from the roots. The second method incooperates the reed-mats, already planed to grow Pastia on around the structure. These mats

are roughly 10 *cm* thick and buoyant for an extended time period, until the reed-fibers have soaked up too much water and lose their buoyancy. The aim is that Salicornia is planted onto these mats floating within the flowerbed. The mats will eventually lose buoyancy as they soak up water and the plant gains in mass. The mats together with the crop will subsequently sink down to the bottom of the flowerbed, where Salicornia is growing partly submerged until harvest. Both growing techniques differ from the manner Salicornia naturally grows. The plant grows in tidal marshes and is usually submerged by tides twice a day, which is difficult to simulate by an energy independent system. The chosen farming techniques rely on the fact that Salicornia is used to being submerged and growing in wet soil.

The flowerbed design to accommodate the two growing techniques was then discussed in depth with a small consortium of people at EMB, namely Marina Gebert, Sebastian Rakers, Sebastian Kärst and Tim Staufenberger. The first problem quickly identified is the size of the flowerbed depicted in figure 6.3 and the material it is supposed to be made of. A steel flowerbed with the dimensions given in figure 6.3 is too heavy, too difficult to manufacture and most of all; too difficult to transport to the OS. Instead are two walkways attached to the inner perimeter of the sub-structures, thereby dividing the remaining growing area into three flowerbeds, two small ones and one big one, in a way that each flowerbed is easily accessible. The individual flowerbeds should furthermore be manufactured from polyethylene (PE), a material the EMB has good experiences with given that most of their aquatic testing equipment is build from PE. Its durability, manufacturing properties and water resistance are of advantage for the flowerbeds.

Each flowerbed consists of vertical walls and a grid as a bottom for water to flow in and out of the flowerbeds unhindered. Figure 6.4 shows the concept in design draft condition. The bottom left of the drawing depicts the top view of the structure and how the growing area is divided into the three flowerbeds, the largest one in the center, along with the walkways. The width of the small flowerbeds is set to 70.5 *cm* since the two small flowerbeds are only accessible from one side, given the greenhouse. The total flowerbed area adding the two small flowerbeds and the center flowerbed amounts to 11.75 m^2. This is 6 % less then is required by both the OFK and the EMB. However would the construction of the sub-structures in non-standard length make the whole structure more costly. The bottom right shows how the frame supporting the flowerbeds is made up from four sub-structure, each equipped with four floaters. The connection between the sub-structures making up the frame is nevertheless a rigid one, forcing the the four sub-structures to move as one large frame. The side view on top further shows how the greenhouse spans the whole growing area.

6.3 Qualitative Concept Review

The qualitative validation of the concept design is done using the tool already implemented in Huhnt (2018), namely the Performance Based Specification (PBS) and the FAST method already used in section 6.2. The PBS were in the preceding project thesis identified as the ones shown in table 6.1. The PBS state that the structure must provide a stable platform for the crop to grow and the crop needs to be passively irrigated by seawater. It is furthermore important to allow easy access for planting and harvesting and, if possible, to enable extensions within an MU-IMTA approach.

A qualitative review of the structure confirms the first point, given the estimated low center of gravity (COG). The small size of the flowerbeds allow the altitude of each flowerbed to

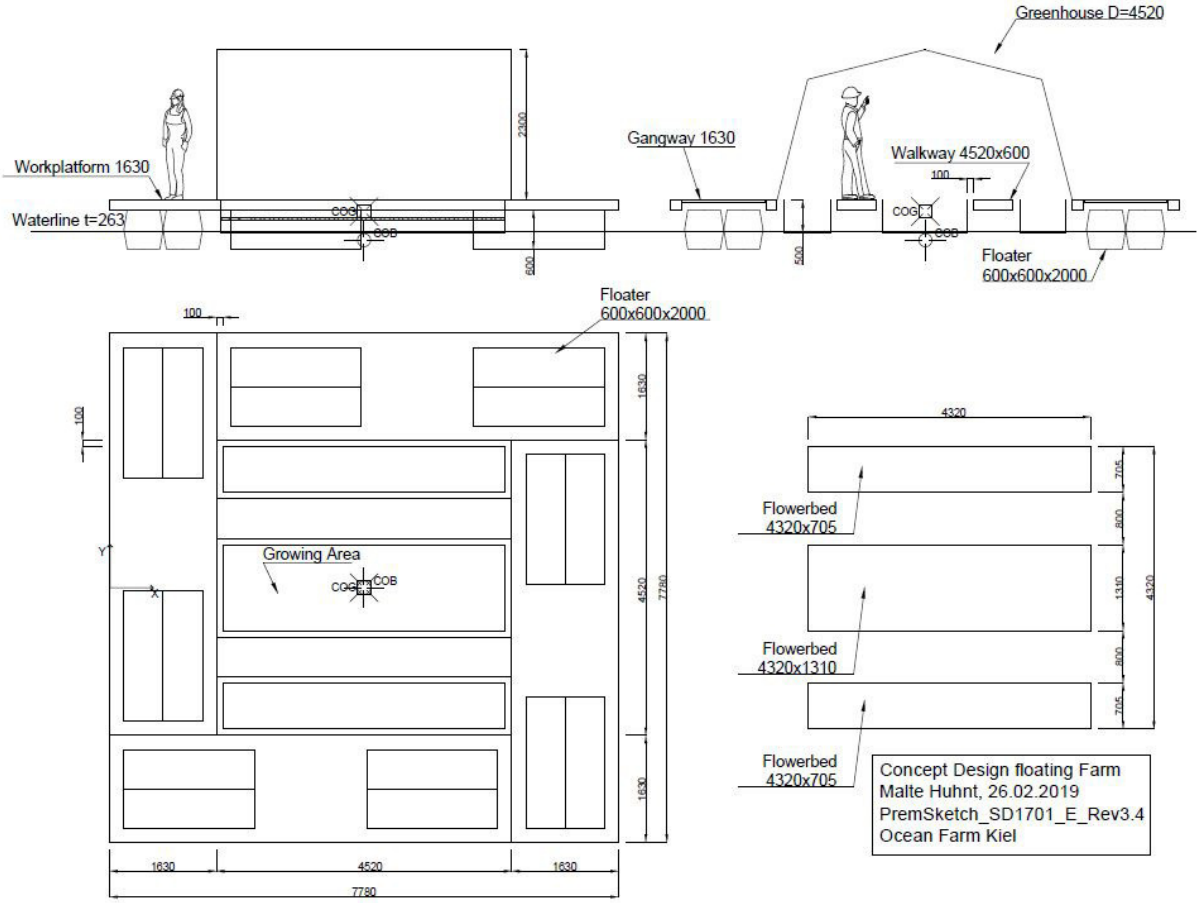

Figure 6.4: The concept ready for in-depth analysis. The top view on the bottom right show the floater layout and the growing area. The flowerbed layout is shown on the right and the side views on top.

be altered, changing the level of submergence of the plants without changing the fundamental stability of the structure. The second point of passive irrigation is hence met as well.

The third point is fulfilled when looking at the width of the frame surrounding the growing area. The width of the individual sub-structures allows for easy storage of products harvested in- and around the platform as well as loading and offloading of the service vessel. The last point in table 6.1 emphasizing MU-IMTA applications to be installed on the farm is fulfilled as well. The structure is offering an abundance of deck space to work on applications other then Salicornia (such as Pastia growing on mats around the farm), and the floaters offer enough buoyancy for different flowerbed arrangements and different growing techniques to be applied as well as other products to be grown hanging on- or suspended by the structure.

The second method used to evaluate the design qualitatively is the FAST method. This method is used to check for the basic conceptual feasibility of the structure, to ensure the critical path is existent in the new design. Figure 6.2 in section 6.1 shows that the the critical path is being followed by the structure, from the low order functions up to the high order function. The wide gangway around the growing area allows for easy access, the substrate as well as the mats provide an anchor for the crop to attach to, the open flowerbeds assure an ample supply of seawater and the greenhouse protects from wind while letting the sunlight pass through. Further allows

Table 6.1: PBS with weightage (Huhnt, 2018)

#	Performance Based Specification	Weightage
1	Offer enough space, buoyancy and stability to grow Salicornia while being able to withstand the environmental loads	35
2	The plants are passively irrigated by seawater without human support	30
3	Allow enough space for convenient planting, servicing, harvesting and fastening of the service vessel	20
4	Enable the expansion of the pontoon to serve as the nuclei for a MU-IMTA	15

the arrangement of flowerbeds, walkways and frame unimpaired operation on the farm. What has to be confirmed is if the structure is able to float stable when subjected to the environmental loads expected at the farm.

6.4 Weights and initial Stability

The estimation of the weight of a floating structure is one of the biggest challenges and economically one of the greatest risks in naval architecture. The weight has an influence on almost every aspect of the performance of a floating structure. The monetary impact can be devastating, if a certain aspect agreed upon in the building contract is not met. The difficulty is that the weight estimation is connected with much uncertainty and its accuracy depends usually on the experience a shipyard or an engineering firm has gathered. An additional difficulty is that the weight of the structure changes as the design changes within the development spiral. The weight estimates are consequently vague during the initial design phase and narrow down as the design progresses.

There are in general two approaches when it comes to weight estimation. If the structure to be designed is large and conventional, the use of approximation formulas is commonly applied. The advantage of these formulas is the minimal input needed while giving a good indication of the weight of the structure, especially if the structure's purpose, design and size are within conventional limits. These weight estimations can be refined as known weight contributors, such as main engine and payload, are added during the design spiral. The calculation of the steel-weight fraction of the light ship weight is nevertheless vague and can only be met with the experience a manufacturer has gathered from previous projects. The disadvantage is that the structure needs to be within conventional limits, as approximation formula are empirical and represent a trend line for ships or structures build in the past with certain main dimensions and purposes. Using these formulas if the design is out of the ordinary must hence be treated with utmost caution, since the type of structure the approximation formula is based on and the structure that is to be designed diverge.

The second method and probably the more intuitive one is the listing of all weight components and their position on the structure. The advantage is that the result is an accurate representation of the models mass and inertia characteristics. The disadvantage is usually the amount of work and knowledge of details this method requires. The details of the structure are usually unknown in the early design phase and the amount of weigh contributors usually so large, that an accurate representation of them within a table is not possible. The application of this method furthermore contains the risk of forgetting crucial weight groups. It hence should only be applied to small structures of manageable complexity.

The size of the structure to be designed and the absence of historical examples nevertheless suggest the utilization of the second method, the weight list. The structure deadweight consists out of the light ship weight and the payload. The light ship weight is divided into three sub-groups: the frame structure, the greenhouse and the flowerbeds. The payload consists of the plants plus the substrate to grow the plants. The information for the frame structure as well as the greenhouse are gathered from the respective manufacturers while the weight of the flowerbeds is calculated given the flowerbeds material properties and dimensions. The weight of the payload is estimated at the end of the growing-cycle of Salicornia. The plant being fully grown weighs about 0.5 kg growing in a small flowerpot filled with substrate weighing about 0.5 kg. Given the flowerpots diameter of 15 cm and the growing area of11.75 m^2 fit the three flowerbeds 1985 plants amounting to almost 2 t of payload. The total mass amounts to 4592.7 kg which is supported by the 16 floaters. The total displaced volume is 4.538 m^3, since the water density (ρ) in the Baltic Sea, especially in the Bight of Kiel, is lower compared to the global standard density of 1025 $\frac{kg}{m^3}$. At the OS is ρ estimated to be $\rho = 1010\ \frac{kg}{m^3}$ due to the large fresh water ingress from the river Schwentine and the NOC (Staufenberger, 2019).

The approach chosen to account for the mass in the wave body interaction (WBI) and stability calculation program HydroD was to model the full structural body and to account for the flowerbeds and payload using point masses. Since the geometry modeled at this stage is to be used throughout this thesis is the accuracy of importance. Hence was the initial stability, the initial distance between center of gravity and metacentre (GM_0), calculated here in order to compare the mass properties of the model geometry against the weight list prepared in Excel (how to calculate stability is explained in section 7). The resulting mass- and initial stability characteristics are found in table 6.2. The draft of the structure is low, which results in a low center of buoyancy (COB). And since the mass is concentrated close to the waterline is the center of gravity (COG) close to the stillwaterline as well. This circumstance, together with the large horizontal distance between the floaters, leads to a high initial stability of $GM_0 = 29.3\ m$.

Table 6.2: Mass and initial stability attributes calculated from the mass-table prepared with Excel

Deadweight $[kg]$	Displacement $[m^3]$	Draft $[m]$	COB (x,y,z)$[m]$	COG (x,y,z)$[m]$	GM_0 $[m]$
4592.7	4.538	0.234	(3.89, 0, 0.117)	(3.89, 0, 0.576)	29.3

7 Hydrostatics & Stability

Stability is achieved if a floating body is able to return to a neutral floating position after being forced out of this position by an external force or moment. The floating position is considered neutral if the body's gravitational force (F_G) is equal and opposite of the buoyancy force (F_B) exerted by the volume the floating body displaces (∇). Again is the body analyzed assumed as rigid, ergo moving in one, as the influence of hydroelasticity, the flexible fluid-structure interaction between a body and a marine environment, would falsify the hydrostatics of the body.

$$F_G - F_B = mg - \rho \nabla g = 0 \tag{7.1}$$

F_G is exerted by every small mass-share the way F_B is exerted by every vertical fraction of every hydro-static force vector. Hence are both F_G and F_B summarized in a COG and a COB by summarizing each individual mass and each individual buoyancy contributor. Equation 7.2 shows how the vertical COG and COB are calculated by summing up all force contributors given their vertical distance to the origin and dividing it by the sum of all force contributors. This is done in all spatial dimensions x, y and z.

$$COG_z = \frac{\sum_n z_n dm_n}{\sum_n dm_n} \quad , \quad COB_z = \frac{\sum_n z_n d\nabla_n}{\sum_n d\nabla_n} \tag{7.2}$$

When working with marine application is the equilibrium position considered positive, if the body floats upright, ergo if the body is able to fulfill its purpose. Most floating marine applications have two stable equilibrium floating positions from which one is considered positive, aside from self righting Search And Rescue (SAR) vessels and keel vessels, which have only one stable equilibrium floating position. Conventional vessels having two neutral floating positions is due to the circumstance that the COG is above the COB when floating in operation and below the COB when capsized. Compared to *unconditionally stable* self righting vessels mentioned above (SAR- and keel vessels), are most merchant ships *conditionally stable*. The floating body will return to a positive equilibrium position if a certain heeling angle is not surpassed and will capsize if surpassed.

The moment returning the vessel to a neutral position, either positive or not, is F_B multiplied with the *righting leaver arm* (GZ), which is the distance between the line of action of F_G and F_B. The distance GZ is due to the change of displaced volume of the heeled body which is causing the COB to relocate to the side the body is heeling to, enabling a separation of the line of action of F_G and F_B. The correlation between GZ and the heeling angle is nevertheless highly non-linear. This can only be understood when introducing the concept of the *metacentre* (M). M is the point of intersection between the line of action of F_B and the local vertical center line of the ship. The location of M in not fixed and moving as the COB relocates sideways. The distance between the M and the COG is an important parameter too in order to asses the initial stability of the vessel. This metacentric height (GM) can tell the designer how vulnerable a vessel is to small heeling moments and how stiff the vessel reacts to a heeling moment. The vertical distance between the COB and M denoted BM of a vessel can be calculated by dividing the geometrical moment of inertia of the waterplane are around the x-axis (I_{xx}) by ∇. The GM can consequently be estimated as the distance between keel and M (KM) minus the vertical COB, here denoted KG.

$$BM = \frac{I_{xx}}{\nabla} \quad , \quad KM = KB + BM \quad , \quad GM = KM - KG \tag{7.3}$$

Figure 7.1 shows an idealized ship cross section along with the COB, the COG, the heeling angle (η), M and the GZ in a neutral and heeled condition. The figure exemplifies a conditionally stable system as the COG is located above the COB when in the operational floating condition and below the COB when capsized.

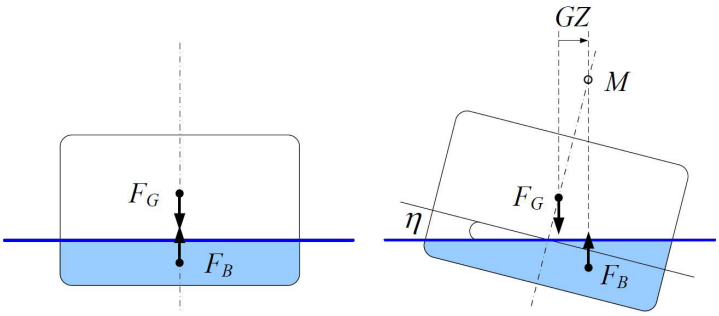

Figure 7.1: An idealized ship section is shown with the positions of the COB and the COG in a neutral- and heeled condition. The heeled condition on the right shows the change of displaced volume and the GZ along with M (Rosén, 2017)

As GZ is directly linked to a body's capability to straighten itself from a heeled position, is the development of GZ over η used by naval architects to judge a vessel's stability. Figure 7.2 shows two GZ-curves. The left one is exemplary for a conventional ship. The more the vessel is heeled, the larger GZ grows till a maximum is reached. The GZ is decreasing from this point until it reaches zero. The system is again in equilibrium at this point, but an unstable one. The vessel would capsize if heeled beyond this point, since GZ would become negative, turning the vessel until the COG is below the COB. The right GZ curve shows a vessel in a damage condition, e.g. an unsymmetrical flooding. The vessels neutral position is heeled but some stability is left before the vessel capsizes.

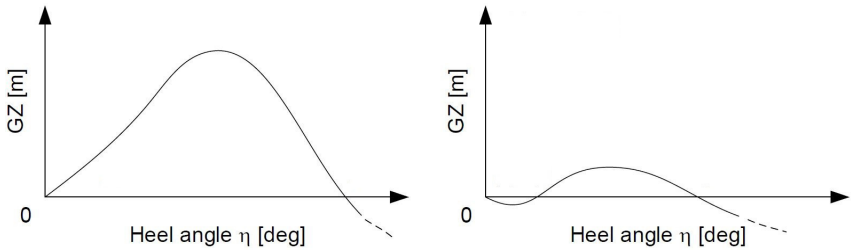

Figure 7.2: A GZ-curve for a conventional vessel on the left and a GZ-curve for a listing vessel on the right (Rosén, 2017)

The GZ-curve is probably the most important measure of stability for conventional floating structures and hence analyzed in detail to asses the intact and damage stability of a vessel. Not only the shape and range is assessed but also the area under the curve, the maximum GZ and the tangent at the origin. Having a good understanding of the GZ-curve can tell a designer much about the structure, hence is a good understanding of the GZ-curve vital. Classification societies worldwide as well as international organizations such as the International Maritime Organization (IMO) have defined standards the GZ-curve has to comply with in order for the structure to be considered save. The intact stability of this structure is assessed according to

the intact stability requirements of the DNV-GL offshore structures rule book DNV-GL (2015) to ensure safe operations. Table 7.1 lists the intact stability requirements formulated by IMO taken from DNV (2011).

Table 7.1: IMO intact stability requirements taken from DNV (2011)

	Required	Unit
Area 30°	0.055	$[mrad]$
Area 40°	0.9	$[mrad]$
Area 30° − 40°	0.03	$[mrad]$
GZ 30°	0.2	$[m]$
Location GZ_{max}	25	[°]
GM_0	0.15	$[m]$

8 Waves

The sea environment is a multifaceted system with a multitude of factors interacting with each other. The combination of global position, water temperature and density, depth, wind, currents and tides influence the sea environment and thus the interaction of marine installation with the surrounding body of water. This mosaic of parameters define the structure's position in the water and the loads it is subjected to. The largest loads acting on the structure and usually the most important ones to consider are however loads exerted by waves, followed by wind- and currant loads, especially when analyzing dynamic phenomena and mooring arrangements.

The wave environment with all its characteristics is summarized under the concept of *seastate*. A seastate is a random disorderly system of momentary waterlevel variations around a mean water surface (waves). These waves have different origins, from tidal waves to waves generated by winds or earthquakes. The most important waves for naval architects and mariners are waves generated by wind at the location of interest and waves that have been created in a distant location traveling through the observed location. The former waves are referred to as *wind seas* while the later are called *swell*. Wind seas are parallel to the dominant wind direction, while a swell is generated by a wind-system far away that may not even be existing anymore.

The resulting seastate is described by a significant wave height (H_s), the mean of the highest third of all observed waves, and a peak period (T_p). This measurement is usually in good agreement with the wave height and period observed by experienced mariners. It does however not imply that only this wave is present in the seastate. On the contrary is a seastate a combination of multiple waves with different height and period interacting with a different phase, where H_s and T_p describe the wave with the largest energy contribution to the seastate. This can be described by a wave spectrum.

The use of a wave spectrum is a stochastic method to establish the wave conditions to be considered when designing a marine structure by mathematically listing the waves, defined by the wave period and wave height, that make up the seastate and give their individual energy contributions. These formulas have been found empirically by measuring real-life seastates and extracting the waves the seastate is made up from. Therefore can a seastate be described by the right choice of formula based on only a limited number of parameters. The right formula to describe the seastate is up to the designer since it depends on the characteristics of the seastate in question. Seaspectra recorded out at sea can be used to condense information of a seastate onto only a limited number of parameters, most importantly H_s and T_p. The knowledge of these two and the wavespectrum formula used can further enable the designer to reproduce the wave time series, a time domain realization of a random seastae described in greater detail in section 11.3, with the characteristics of the measured seastate. The connection between these wave-parameters and the seastate is the variance m_0, the area under the curve of the seastate as its square root gives the deviation from the mean of the spectrum (Greco, 2018). How to develop e.g. H_s from the spectrum using m_0 is shown in equation 8.1 (Faltinsen, 1993).

$$m_0 = \frac{H_s^2}{16} \tag{8.1}$$

The Pierson-Moskowitz (PM) spectrum describes a disorderly seastate comparable to a seastate found on the open ocean. The Joint North Sea Wave Project (JONSWAP) spectrum on the other hand can be used to describe more orderly seastates such as a seastate dominated by wind

seas with little swell-interaction. The peak of this wave spectrum is hence more concentrated on a smaller band of frequencies compared to the PM spectrum. Both spectra the PM- and the JONSWAP spectrum are compared in figure 8.1. The peak in the dotted JONSWAP spectrum is governed by the γ operator that usually moves between $\gamma = 1$, representing the PM spectrum, and $\gamma = 5$ (DNV, 2010). The higher this operator, the more pronounced the peak and the more orderly the seastate since most of the energy is being transmitted by only a few waves.

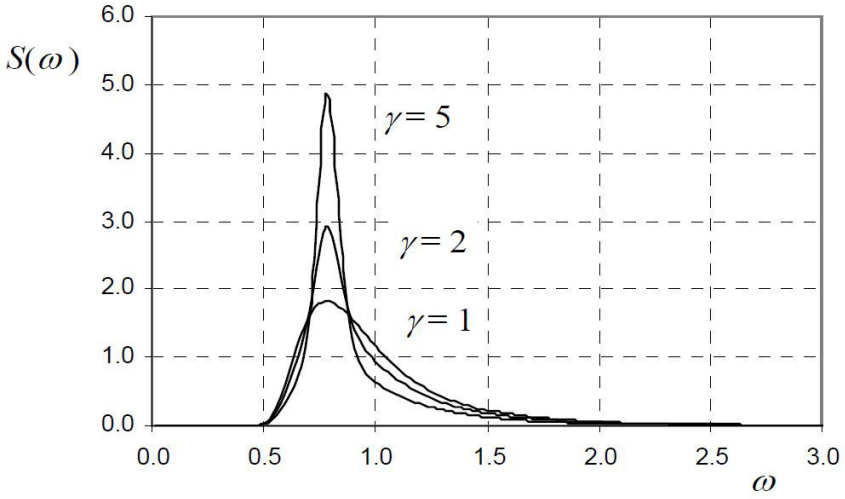

Figure 8.1: The JONSWAP spectrum given three different γ values applied to a seastate of $H_s = 4$ m and $T_p = 8$ s. The value $\gamma = 1$ represents the PM spectrum (DNV, 2010)

One has to be aware that the description of a seastate using a wave spectrum is already a simplification. The wavespectrum assumes that the seastate can be split up into waves which are super-positioning each other. Waves are not only super-positioning each other but are also influencing each other, hence is information about the seastate lost as soon as superposition is assumed. The amount of information lost is however highly dependent on the seastate.

8.1 Wave Descriptions

Seastates need to be described mathematically to extract information vital to the structure being designed, such as excitation- and pressure loads. It is crucial to remember that simplified mathematical descriptions of seastates are automatically leading to a loss of information. The amount of information lost depends on the method used and the nature of the seastate itself. It is in the hands of the designer to decide upon an accuracy the environment is to be represented with. The description accuracy comes at the price of computational expense and the applicability of the description. The more defined the environment is the less can these results be transferred to other locations and different environments. Describing rough seastates with high accuracy is time consuming and prone to possibly hard to detect errors. Due to these difficulties is model-testing still one of the most accurate and reliable methods to predict loads on floating structures interacting with waves.

The linear description of waves is the simplest mathematical representation. Linear theory assumes the first order velocity potential (ϕ_1) of the fluid particles to be proportional to the amplitude of the wave (ζ_a) by linearizing the free surface condition yielding the combined free surface condition. The combined free surface condition, a combination of of the kinematic- and

dynamic condition, ensures that the pressure at the mean wave surface is equal to the ambient pressure. Equation 8.2 shows how ϕ_1 of a wave propagating in x-direction can be found using the wave frequency (ω) and the wave number (k). Equation 8.3 shows how the corresponding wave profile can be developed (Faltinsen, 1993).

$$\phi_1 = \frac{g\zeta_a}{\omega} e^{kz} cos(\omega t - kx) \tag{8.2}$$

$$\zeta = \zeta_a sin(\omega t - kx) \tag{8.3}$$

The linear assumption can only be made if the water is regarded as in-compressible, inviscid and irrotational (Faltinsen, 1993). The description of waves using linear theory is the most accurate if the nonlinearities within the wave itself are small, ergo if ζ_a is small compared to the wave length (λ). The measure of nonlinearity (ϵ) is hence the ratio between ζ_a and λ. The wave shape is well approximated by a sinusoidal wave if $\epsilon = \frac{\zeta_a}{\lambda}$ is small. The wave tends to lose its sinusoidal shape if the waves steepness increases. Figure 8.2 shows that the wave peaks of real waves are more pronounced and the wave troughs more shallow. This phenomenon can be captured when using higher order theories to describe waves such as 4^{th}- or 5^{th} order Stokes Theory, which is not attempted by this thesis.

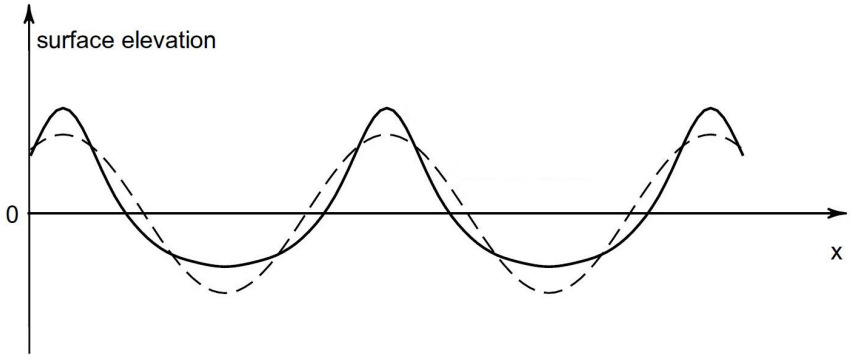

Figure 8.2: The comparison between a linear sinusoidal wave (dotted line) and a higher order description of a wave (solid line) which is a more accurate representation of a regular wave (Brorsen, 2007)

The advantage of using linear wave theory is that a seastate can be described as a superposition of a multitude of waves with different heights, periods and phase shifts which are nevertheless not interfering with each other. This makes the representation of a seastate with a wave spectrum, such as PM- or JONSWAP spectrum, possible. The first differentiation that is made when describing a seastate is between regular and irregular as well as short- and long-crested gravity waves. Irregular waves state that the energy within a seastate is distributed within a range of frequencies, not carried by one frequency only, while long crested means that the energy propagates in one direction instead of waves interacting from multiple directions. The term gravity waves referrers to the λ of the individual waves. Waves with λ greater then 1 cm are governed by gravity as waves with $\lambda \leq 1$ cm are noticeably influenced by the surface tension of the water.

The linear wave theory, or Airy Theory, is the first approximation that satisfies the free surface boundary condition. The first order approximation is nevertheless prone to higher order errors proportional to ζ_a^n that are neglected when solving the linear velocity potential. This can be

improved by introducing the first *Stokes Expansion* that solves the velocity potential up to the second order, sharpening the wave crest and making the wave trough more shallow, as depicted in figure 8.2. Equation 8.4 shows how the surface elevation of a wave can be described with greater accuracy using the first stokes expansion.

$$\zeta = \zeta_a sin(\omega t - kx) + \frac{1}{2}\zeta_a^2 kcos[2(\omega z - kx)] \tag{8.4}$$

Following DNV (2010) however can the quasi static response of ocean structures be sufficiently analyzed using linear wave descriptions predicted by statistical methods, such as H_s and T_p. Second- and higher order wave theories become important for slender structures in the realm of the mean wave-surface interacting with an environment dominated by viscous forces, as higher order wave theory better predicts the flow speed of water particles in the wave enabling a more precise estimation of viscous loads on the structure. This is not the case here. Furthermore are preliminary calculations of the linear response of ocean structures much quicker to computed using linear theory.

8.2 Design and Survival Conditions

The idea is to establish a design and a survival condition for the given seastate. The design condition should be the limit for operations while the survival condition represents the highest loads to be expected. The OS in the Bight of Kiel is protected in a way that the seastate is governed by wind. Only easterly winds generate waves worth considering since the site is sheltered from any swell coming in from the Baltic Sea by the orifice between the lighthouse Friedrichsort and Laboe, which acts as a barrier.

Wind seas are created by the friction between the two fluids water and air. Although the viscosity of air and hence the ability to transfer shear in the vertical direction is limited, the vast area the wind acts on and the high wind velocities are capable of generating noteworthy waves. The farms OS in the Bight of Kiel is of little interest for the commercial shipping industry and hence are reliable measurements in this specific area not existent to the author's knowledge. The wave conditions are considered small throughout the Bight of Kiel and local mariners base the decisions about sailing or not on the observation of the on-site conditions. The most reliable information about local wind- and wave conditions can be gathered from the pilot-association servicing the commercial fleet going through the outer Bight of Kiel and through the NOC. This method is applied here: the information given by a high ranked member of the pilot-associations Captain Finnberg is checked against the predictions of a mathematical model. The *Coastal Engineering Manual* (Engineers, 2008) recommends the use of the following formula derived from the JONSWAP growth law for peak frequencies to estimate the characteristics of a wind sea:

$$\frac{gH_s}{u_f^2} = 4.13 * 10^{-2} \left(\frac{gX}{u_f^2}\right)^{\frac{1}{2}} \tag{8.5}$$

$$\frac{gT_p}{u_f^2} = 0.751 \left(\frac{gX}{u_f^2}\right)^{\frac{1}{3}} \tag{8.6}$$

Equations 8.5 and 8.6 enable the calculation of the significant wave height H_s and the peak period T_p given the gravitational acceleration (g), the fetch (X) and the friction velocity (u_f). The later is calculated given the drag coefficient (C_D) and the wind velocity 10 m above the surface (U_{10}):

$$C_D = 0.001(1.1 + 0.035U_{10}) \tag{8.7}$$

$$u_f = (C_D U_{10}^2)^{\frac{1}{2}} \tag{8.8}$$

The fetch X, the straight line distance the body of water in question is exposed to the wind, is measured at the location of the farm. Figure 8.3 shows the maximal fetch that could reach the OS given an east-south-easterly wind.

Figure 8.3: The fetch at the OS in the Bight of Kiel given east-south-easterly winds is 2.3 *km (Google, 2019)*

Once it is made clear that the wave conditions are dominated by wind seas can a design- and a survival condition be defined based on the wind speed. The design wind, up to which the operation of the platform is to be feasible, is set to 6 bft, the survival condition to 10 bft. Both values represent conservative estimates given the protection by land, which should make especially the survival condition very unlikely. These estimates enable the definitions of H_s and T_p using equations 8.5 and 8.6. Table 8.1 lists the conditions the structure is subjected to, which match up closely with the wave characteristics Finnberg (2019) estimated.

Table 8.1: Design and survival criteria for wind and waves

	Wind Speed $[bft]$ / $[\frac{m}{s}]$	H_s $[m]$	ω $[\frac{rad}{s}]$	T_p $[s]$	λ $[m]$
Design	6 / 14.40	0.365	3.489	1.801	5.062
Survival	10 / 28.81	0.837	2.646	2.375	8.805

Besides H_s and T_p are also the wave steepness and the water-shallowness important parameter when characterizing waves, as they define the calculation-strategy to be applied. Figure 8.4 depicts a handy tool to categorize waves according to their steepness and shallowness to recommend a wave theory to use. The depth at the OS is $d = 12$ m, the blue dot representing

the design condition and the red dot representing the survival condition however show that the water can be assumed deep. More critical is the wave steepness. The Baltic Sea is known for its short and steep waves, which is coherent with the figure. Both waves are highly nonlinear and especially the survival wave is close to the breaking limit. This has to be accounted for when conducting in-depth calculations, which is not attempted since an approximate estimation of the wave loads on the structure is sufficient here.

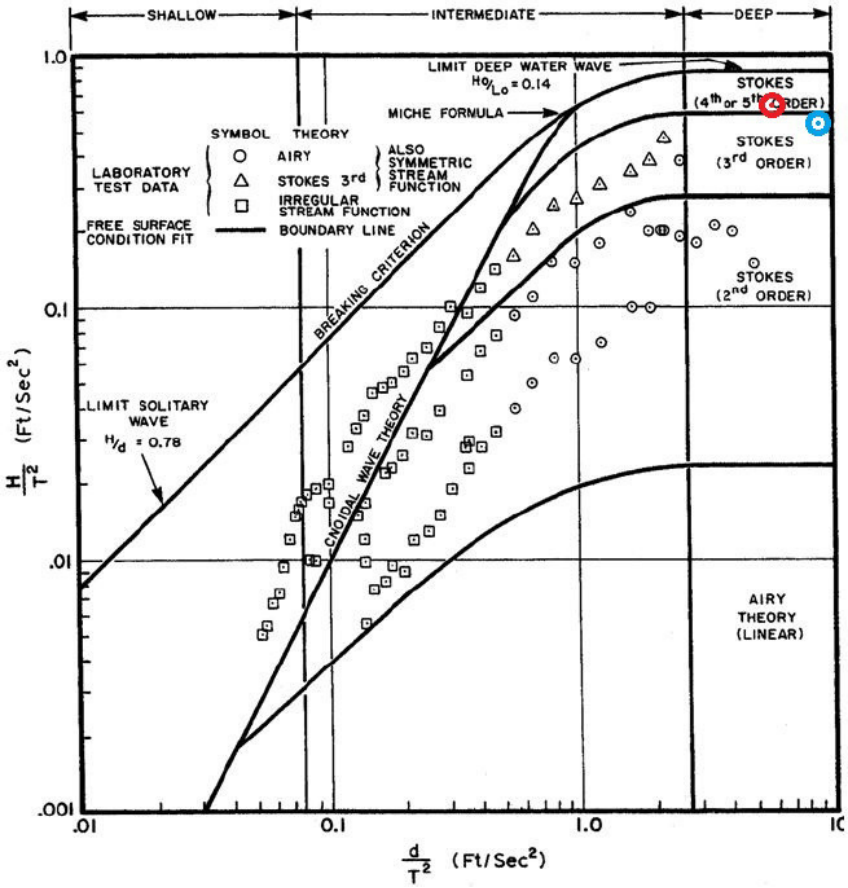

Figure 8.4: The wave steepness is plotted against the shallowness (DNV, 2010). The blue dot represents the design wave, the red dot the survival wave at the OS. Both waves are considered deep but highly nonlinear

The seastate is represented using a JONSWAP spectrum described in section 8 as this spectrum is good in representing fetch limited wind seas, ergo seastates where the generation of waves is governed not by the time the wind is acting upon a surface but the length of the surface, the fetch. The advantage is that the energy distribution within the spectrum can be manipulated using the γ-operator to better represent the seastate at the OS. This is important, since Captain Finnberg attested a very orderly seastate with little variance, which indicates that the energy within the seastate propagates only within a narrow frequency band. Hence is $\gamma = 3.3$ chosen. The wave spectrum is calculated following DNV (2010) as:

$$S_J(\omega) = A_\gamma \frac{5}{16} H_s^2 \omega_p^4 e^{-\frac{5}{4}\left(\frac{\omega}{\omega_p}\right)^{-4}} \gamma^{e^{-0.5\left(\frac{\omega-\omega_p}{\sigma\omega_p}\right)^2}} \tag{8.9}$$

with A_γ calcualted as:

$$A_\gamma = 1 - 0.287ln(\gamma) \tag{8.10}$$

The left graph in figure 8.5 compares the characteristics of the PM and the JONSWAP spectrum given the design condition specified in table 8.1. The peak for the JONSWAP spectra is much more pronounced then for the PM spectra, an indication for an orderly seastate. The graph on the right compares the two conditions, design and survival, against each other. The JONSWAP survival spectrum shows how the energy contained in the seastate is much higher and how the peak moves towards the peak frequency (ω_p) of the survival seastate.

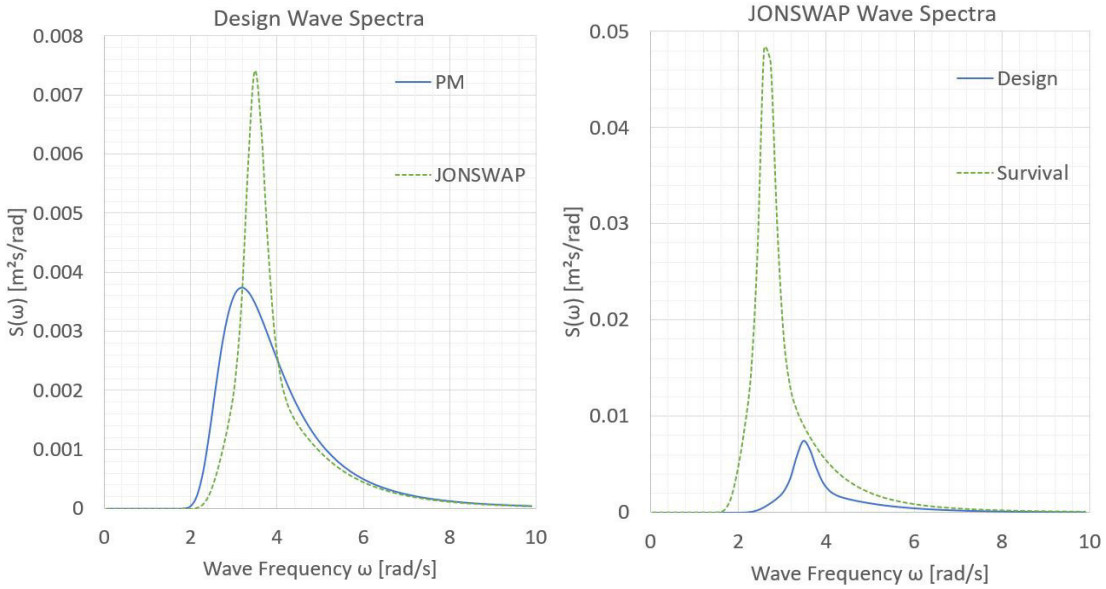

Figure 8.5: The left graph compares the PM- and the JONSWAP $\gamma = 3.3$ spectrum for the design condition to show how the the JONSWAP spectrum is more banded than the PM spectrum. The right graph compares the same JONSWAP design spectrum against the JONSWAP survival spectrum. The comparison shows how the band moves towards ω_p of the respective condition

Assuming that the analysis in question requires a first order velocity potential only can ϕ_1 following Faltinsen (1993) be extracted from the wave spectrum using the number of wave components (n) as well as the wave amplitude ζ_a taken from the wave spectrum using equation 8.11, where β is the angle between wave propagation direction and x-axis, ω_j the wave frequency in question and k_j the wave number of of the wave component j. The random phase angle is captured by φ_j.

$$\phi_1 = \sum_{j=1}^{n} \frac{g\zeta_{a.j}}{\omega_j} cos(\omega_j t - k_j x cos(\beta) - k_i y sin(\beta) + \varphi_j) \tag{8.11}$$

Current is another important factor when assessing the environment the structure is to interact with. Peak current velocities in the Bight of Kiel are strongly connected with winds coming in from the east. The wind forces water in the shallow west Baltic Sea and into the Bight of Kiel. Significant currents are measured during storms when deep water layers start flowing opposite to the wind driven surface current. The strongest current is nevertheless measured shortly after the storm, when the water flows back out of the Bight of Kiel. The current is in this case flowing

in an north-north-easterly direction, almost perpendicular to the wind. In order to design the mooring of the structure for the worst case possible, the maximum current velocity is used for the survival condition and the mean current for the design condition.

The currents were measured at the OS in the Bight of Kiel from mid August 2017 to mid August 2018, as the left-hand graphs in figure 8.6 shows. The average current velocity is low throughout the year, with an overall average velocity of $v_{avr.} = 0.021\ \frac{m}{s}$. The maximum current however varies substantially, as a comparison between April and Mai 2018 shows, due to the weather events mentioned above. The maximum current velocity chosen for the survival case is $v_{max} = 1.17\ \frac{m}{s}$ in a north-north-easterly direction.

The current profile the mooring system is interacting with depends on a multitude of factors, such as tides, wind, water density, water depth and water temperature. A detailed knowledge of the current profile and the factors influencing it is hence vital, if current loads are expected to be dominating. This is not the case in this thesis. The survival current profile on the right hand side of figure 8.6 is hence calculated following a simple power law presented by equation 4.1.4 in DNV-RP-C205 (DNV, 2010). Equation 8.12 shows how the current profile is calculated.

$$v(z) = v(0)\left(\frac{d+z}{d}\right)^{\alpha} \tag{8.12}$$

The current is a function of the vertical position in the watercolumn z (positive upwards) and the water depth d at the OS. The velocity $v(0)$ is the current velocity at the still waterline, in this case equal to v_{max} and α is an exponent influencing the shape of the current profile. Due to the lack of information is α chosen to be $\alpha = \frac{1}{7}$, the default value from DNV (2010). Equation 8.12 ensures that the maximum current velocity is met right at the still waterline and that the current goes to zero at the sea-floor.

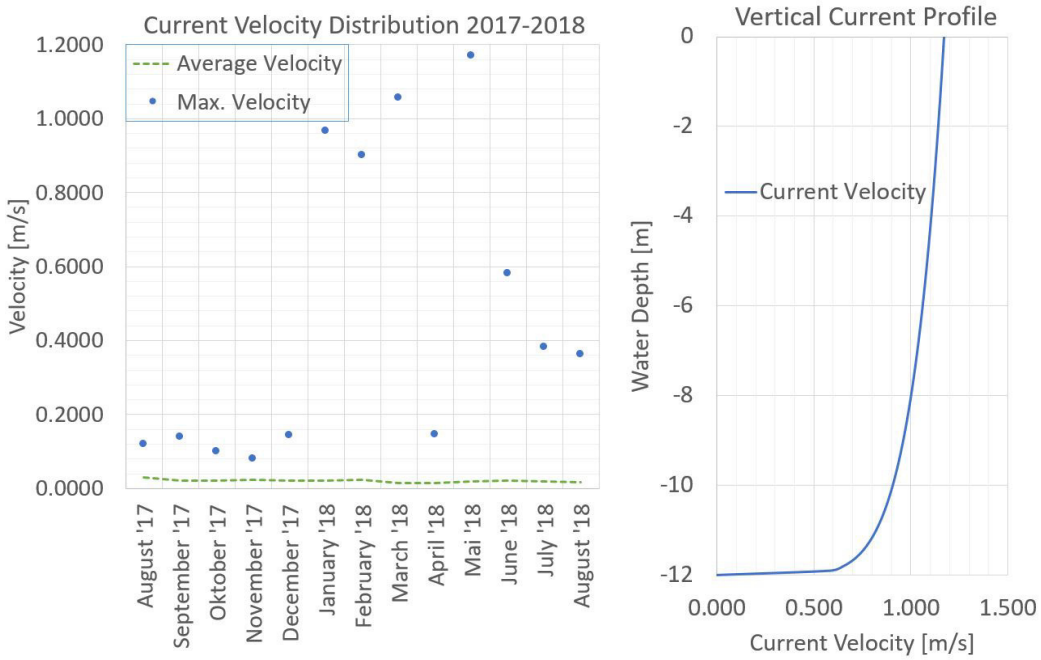

Figure 8.6: The lefthand graph compares the anual average- and max. current velocity at the OS. The righthand graph depicts the current profile in the watercolumn as recommended (DNV, 2010)

The last environmental influence that is modeled is the wind. The wind is in this case taken to be a non-fluctuating static force acting onto the structure from the wave direction. The force is estimated by taking the sideways profile of the structure as the relevant sail area, as this side givse the biggest obstacle to the wind. The wind spectrum is modeled following DNV (2010) using the equation for the logarithmic wind speed profile shown in equation 8.13. The friction velocity (u_f) is taken to be $u_{f.sur} = 1.32\ \frac{m}{s}$ for the survival case and $u_{f.des} = 0.58\ \frac{m}{s}$ for the design case following equation 8.8. The hight above the water surface is represented by z, k_α is the *von Karman's constant* at $k_\alpha = 0.4$ and the roughness of the water surface is accounted for using the roughness parameter z_0. The later parameter depends strongly on the location and varies between $z_0 = 0.0001$ and $z_0 = 0.010$ for an open sea with waves, depending on the seastate. In this case was $z_0 = 0.0016$ chosen, for the profile to be in line with the wind generating the survival- and design seastate respectively according to the JONSWAP growth law.

$$U(z) = \frac{u_f}{k_\alpha} ln \frac{z}{z_0} \tag{8.13}$$

The wind profile is shown in figure 8.7. The design and survival wind spectra are depicted from 10 m above the waterline downwards, with both of them reaching the wind speed as defined in table 8.1 10 m above the waterline.

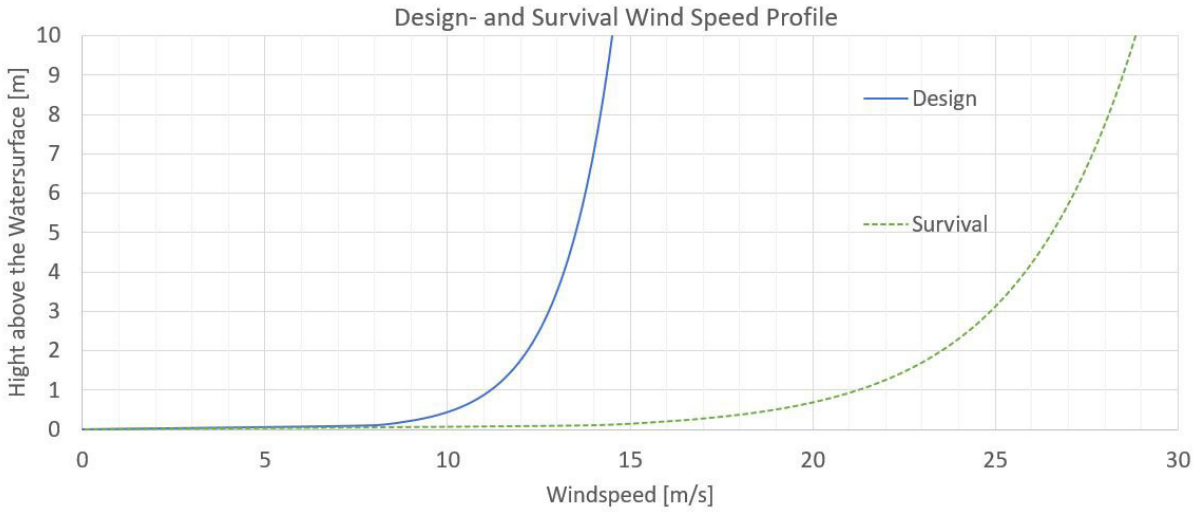

Figure 8.7: The wind speed profile for the design and survival condition from 10 m *above the still waterline downwards*

Integrating the wind speed over the area of the structure, most importantly the greenhouse, gives a steady force to be applied onto the structure. The force is found by simply applying the drag equation for a body interacting with a fluid, in this case air, with an air density taken as $\rho_{air} = 1.225\ \frac{kg}{m^3}$ and a drag coefficient $C_{D.Body} = 1.28$, corresponding to a flat plate (Hall, 2015). The total area (A), greenhouse plus structure, is taken as $A = 14.21\ m^2$. The formula on how to calculate the drag of the structure is presented in equation 8.14. The wind speed is applied using the wind profile described above.

$$F_D = \frac{1}{2} \rho_{air} U(z)^2 C_{D.Body} A \tag{8.14}$$

The resulting drag force for the survival case is $F_{D.Sur} = 4.99\ kN$ and $F_{D.Des} = 1.38\ kN$ for the design case, acting at the center of area of the total sideways area. The drag of the greenhouse contributes 87% of the total drag force emphasizing the importance of the greenhouse for the wind resistance. However, by applying a $C_{D.Body}$ of $C_{D.Body} = 1.28$ is a conservative approach taken as the drag coefficient chosen marks the upper end of the drag range a flat plate lays in.

9 Hydrodynamic Loads and Responses

Structures interacting with an ocean environment are loaded with a combination of hydrostatic- and hydrdynamic pressure. This pressure exerts a force on the body trying to move or rotate it in its six degrees of freedom (DOF). The body is in the following assumed to be rigid, ergo that individual components of the body are stiffly connected to each other allowing the forces to move the arrangement of sub-structures as one body. These forces are acting on a body whether the body is fixed or floating, here however will the focus be on floating structures. The DOF are defined to describe any movement of a floating body by decomposition of the movement. Those DOF are the three special dimensions surge (η_1), sway (η_2) and heave (η_3) as well as the rotations around these vectors; roll (η_4), pitch (η_5) and yaw (η_6). Figure 9.1 shows a tension leg platform (TLP) with its six DOF.

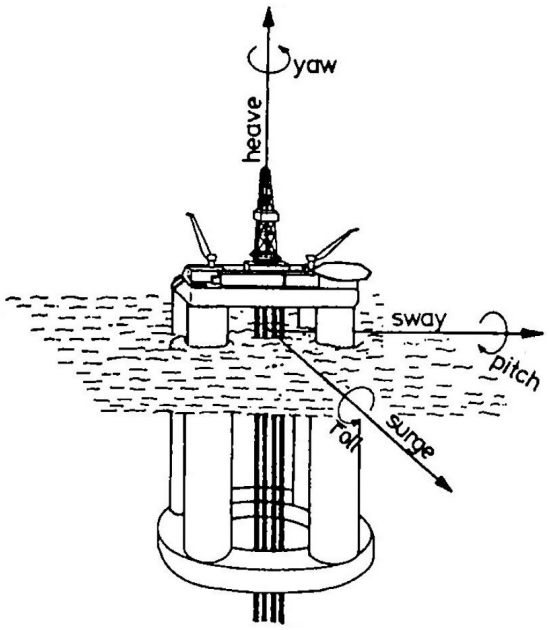

Figure 9.1: The six DOF surge η_1, sway η_2, heave η_3, roll η_4, pitch η_5 and yaw η_6 exemplified on a TLP (Faltinsen, 1993)

Section 7 already described the static interaction of a floating body with the water surrounding it. The difference between WBI and intact stability is that intact stability assumes a flat water surface while WBI aims on estimating the body's response as it is interacting with a seastate. The calculation of the forces and moments acting on the body is hence more complex as it is depending on many factors. The gross of wave induced motions can be described using linear potential theory (Faltinsen, 1993) but as with linear wave theory are some higher order effects waves have on floating bodies omitted when applying this method. For example are vertical motions as well as rotational motions around η_1 and η_2 captured well using linear theory, while non-linear effects can not be omitted when regarding surge, yaw and sway due to the coupling of these motions with the mooring arrangement. Other higher order loads, such as large period difference-wave frequency oscillations, can also play a major role, especially when these are close to the natural surge- or sway period of the structure, possibly leading to resonance phenomena. The basic assumption of the fluid being inviscid and incompressible is also automatically neglecting all loads connected with the friction between the body and the surrounding water.

Loads, such as eddy-making damping on corners, are not captured by linear potential theory. If these simplifications are tolerable depends on the structure and the environment.

While higher order WBI accounts for the change in whetted surface area and the combination of multiple waves acting upon a body is linear theory only regarding the mean whetted surface area and each wave component individually. Potential theory further implies that the response of the structure is proportional to the wave amplitude analog to ϕ_1 being proportional to ζ_a in linear wave theory. Furthermore is the response of the floating body oscillating with the frequency of the incoming wave (Greco, 2018). The advantage is that the response to each individual wave fraction allows the analysis of a body interacting with a seastate in *frequency domain*. The way an irregular seastate can be described as the superposition of many waves of different frequency and height can the response of the structure to this irregular seastate be described as the superposition of the response of the body to each of the individual waves within the irregular seastate. Finding a solution in frequency domain yields the advantage of greatly reducing the computational expense compared to a time domain solution. Instead of generating a time-series of waves, subjecting the body to this seastate and then extracting the bodies response from the measured movement of the body in real time, can the linear WBI in potential theory be extracted directly using wave spectrum and *response amplitude operators* (discussed in section 9.5). Time domain simulations are on the other hand able to capture effects that are neglected when working in frequency domain, such as the effects from second order wave loads mentioned above.

9.1 The Equations of Motion

The equations of motion (EOM) are the tool translating forces to motions, in this case excitation forces to the accelerations and motions witnessed on the structure, by establishing a force equilibrium between excitation forces of the environment and the force response of the structure. The EOM is derived from Newtons Second Law, that a bod's rate of change of momentum is directly proportional to the force applied. The change applied depends on the direction the force is applied from, which makes the definition of this law in all six DOF necessary. This is presented in equation 9.1 where $k = 1,\ 2, ...,\ 6$ with M_{jk} being the mass, $\ddot{\eta}_j$ the acceleration and F_{jk} the force with F_1 to F_3 denoting the the x-, y- and z components and F_4 to F_6 the moments around the corresponding axes.

$$\sum_{j=1}^{6} M_{jk}\ddot{\eta}_k = F_k \quad , \quad k = 1...6 \tag{9.1}$$

The decomposition of the force acting upon the body and the assumption of a steady state sinusoidal motion, as is usually the case for motions engaging a restoring force, enables the formulation of equation 9.1 in terms of the hydrodynamic coefficients A_{jk}, B_{jk} and C_{jk}. Equation 9.2 shows the EOM to calculate the body motions in all DOF.

$$\sum_{j=1}^{6}[(M_{jk} + A_{jk})\ddot{\eta}_k + B_{jk}\dot{\eta}_k + C_{jk}\eta_k] = F_k e^{i\omega_e t} \quad , \quad j = 1...6 \tag{9.2}$$

Hydrodynamic coefficients are associated with mass-, damping- and restoring loads, depending on the property the resulting load is proportional with respectively, be it $\ddot{\eta}_k$, $\dot{\eta}_k$ or η_k. Added mass A_{jk}, proportional to acceleration $\ddot{\eta}_k$, can be pictured as a loosely defined body of water oscillating with different fluid-particle velocities. The oscillation of the body causes

waves, and therefore energy, to radiate away from the structure, which acts as damping B_{jk} on the structure's movement, proportional to the velocity $\dot{\eta}_k$. Both, added mass and damping, are steady state hydrodynamic forces due to the forced harmonic body motions. Furthermore are both highly dependent on the frequency the structure is forced to oscillate with and hence the frequency of the incoming wave exciting the structure to oscillate. A good example is the added mass in heave as it portrays a very diverse behavior over the frequency range: when using linear theory is A_{33} considered $A_{33} \to \infty$ for $\omega \to 0$ and $A_{33} \to constant$ for $\omega \to \infty$. The restoring C_{jk} however is connected with the change of submerged volume, the displacement of the body η_k, ergo the change in pressure acting on the body due to its motions (Faltinsen, 1993). The restoring is necessary in the first place to trigger an oscillatory motion and hence mass- and damping loads. Hydrostatic pressure is nevertheless not the only contributor to the restoring loads, since mooring lines also supply stiffness to the system.

All three coefficients are governed by the shape of the body and the change of the waterline area. The movement of complex bodies with little symmetry leads furthermore to the coupling of hydrostatic motions. A coefficient is considered coupled, if the indices i for the force direction and j for direction of movement are not equal $i \neq j$. This leads to a coupling of motions, as e.g. a coupled added mass A_{ij} for $i \neq j$ will cause a change in j of the structure as soon is i is changed. Coupling between heave and pitch for conventional vessels is a good example. Here, a coupling of the added mass in heave and pitch causes a change in heave as soon as the pitch of the vessel changes and vice versa.

9.2 Radiation and Diffraction

The loads acting upon a floating structure are complex. Linear theory however offers a tool that allows a comparably simple and quick analysis of the loads acting upon a body due to the concept of superposition. The structure is influenced by the waves interacting with the structure, the waves passing the structure and the waves the structure itself generates when oscillating in the water. The characteristics of this interaction depend on the body's geometry and its dimensions relative to the incoming wave. Figure 9.2 is a good example of this as the figure compares the dominant wave defined by λ and the wave height (H) against the characteristic dimension (D) of the body. The larger the structure is compared to the wave, the more are diffraction loads, ergo loads generated by the body diffracting the incoming wave, becoming dominant. The WBI is on the other hand dominated by viscous effects caused by the water-particles flowing passed the structure if the wave becomes very large and steep. The diagram shows that the structure's response is governed by diffraction loads as the blue dot (design condition) and the red dot (survival condition) show. Although the tool allows the rough classification of the loads dominating the WBI should it be treated with caution due to the small draft of the structure, a factor not regarded by figure 9.2.

Linear potential theory offers the possibility to look at the steady-state forces acting upon the body separately by force-decomposition once the transient phase has died out. The first differentiation is made between diffraction and radiation loads. The radiation problem can easily be pictured as the body being forced to oscillate in still water thereby generating waves *radiating* away from the body representing the energy taken out of the system. Radiation loads are hence connected with added mass-, damping- and restoring loads, A_{jk}, B_{jk} and C_{jk}. Diffraction loads on the other hand represent the wave loads acting upon the structure, which is assumed fixed in the diffraction case.

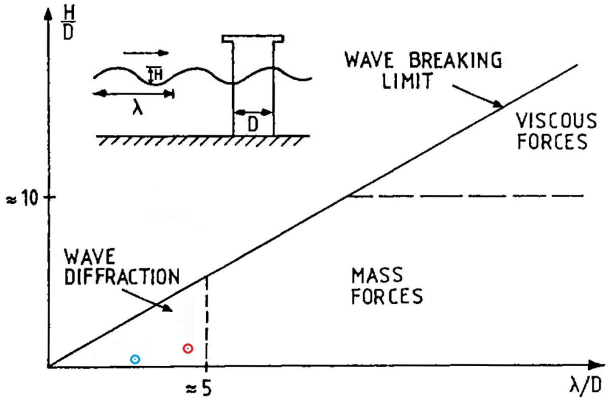

Figure 9.2: The dominant loads on a structure can be estimated by the relation of the wave to the characteristic dimension of the body (Faltinsen, 1993). The blue dot represents the design condition, the red dot the survival condition indicating diffraction dominated loads

The diffraction loads are divided into a diffraction- and a Froude-Kriloff force. Other then the radiation loads do both forces, diffraction- and Froude-Kriloff force, assume the body to be fixed and interacting with external waves. The Froude-Kriloff load estimates the forces the wave exerts on the body, ergo the dynamic pressure acting on the structure. It is important to remember that the wave is not altered by the presence of the body, the force is hence estimated as if the body is not there. This is the opposite for the diffraction load, as this load is caused by the alternation of the pressure field of the wave by the presence of the body. The structure causes the wave to alter its shape, ergo the wave's pressure distribution, by reflecting- or partly reflecting the wave at this point, which again causes loads on the structure. Both, diffraction- and Froude-Kriloff loads, are hence denoted *excitation loads*, as these are the loads consequently exciting the body to move.

9.3 Second Order Wave Loads

The structure is not only effected by first order wave loads but also by second- and higher order wave loads. The importance of these loads onto the seaworthyness of the structure however depends on the structure itself and the effects these loads have onto the motion behavior and hence the operability of the structure. The impact higher order loads have on the motion profile of the structure generally decreases the higher the order, by how much this impact is decreasing depends on the structure. The following aims on introducing second order wave loads as these can largely be estimated without overboarding computational effort and without introducing viscosity into the system, as would have been the case when regarding third- and higher order loads.

Faltinsen (1993) states that the solution of the second order problem results in mean forces causing a drift of the structure and oscillating sum- and difference frequency forces, oscillating with high- and low frequency compared to the first order loads. The body in potential flow theory can either transmit waves, deflect waves or do a combination of both. The mean load is caused by the structure's ability to reflect waves, ergo the ratio between reflected and transmitted incident wave. Naturally is the mean load the greatest when the full incident wave ζ_a is reflected as A_R by the body, resulting in the following adaptation of Maruo's formula: the interaction between an infinite long wall with a beam-sea regular wave, shown in equation 9.3.

The second order velocity potential ϕ_2 is however not contributing to the mean load, given no current and no forward speed, since ϕ_2 is proportional to $sin(2\omega t)$, which has a zero mean value over one period.

$$F = \frac{1}{2}\rho g A_R^2 \tag{9.3}$$

The second order WBI becomes critical as soon as the mean loads described above start oscillating. Depending on the oscillation frequency and the structure the wave is interacting with can these loads cause resonance phenomena, exciting rigid body motions that can severely impair operations, especially when the damping is small, which is often the case as is explained later.

Sum- and difference frequency motions mentioned above refer to the mechanics causing these motions. Sum frequency effects can be caused by a single regular wave resulting in a load oscillating with 2ω, which is especially critical for very stiff structures as these usually have a lower natural period (T_n) which can be excited by sum frequency loads. A typical phenomenon is the springing of TLPs, a resonant high frequency heave oscillation due to the high natural heave frequency caused by the tethers anchoring the vessel to the seafloor causing the structure to have a high C_{ij} in heave. Sum frequency loads are however not assessed further here as the high frequency oscillations are expected to be negligible for the structure in question.

Motion excitation more relevant for the floating structure discussed here are caused by difference frequency motions. Difference frequency motions are slow oscillations that are likely to lay in the realm of the natural frequencies in surge, sway and yaw of the moored structure. Those motions are of importance due to the potentially large motion amplitudes. Caused are slow-drift motions by varying drift forces from individual waves within an irregular seastate. This illustrates an important difference between sum- and difference frequency effects: Difference frequency effects need at least two waves with different frequencies to be caused and are hence generally occurring when the structure is interacting with an irregular seastate (Greco, 2018).

Horizontal translations and rotation at the resonance frequency are furthermore long period motions that only cause minimal linear wave-radiation damping due to the negligible change in whet-surface area, which makes way for large period motions. Viscous damping gains more importance in this case, generally however can damping be considered small. Problematic are the high mooring line tensions triggered by the large motions, as is depicted in the example of a moored ship in figure 9.3. The figure compares three graphs, first the wave elevation at the OS, second the horizontal motion of the moored ship and at last the anchor line tension. The graph in the middle shows the effect of the slowly varying drift loads caused by the irregular waves in the first graph on the ship resulting in large low-frequency motions.

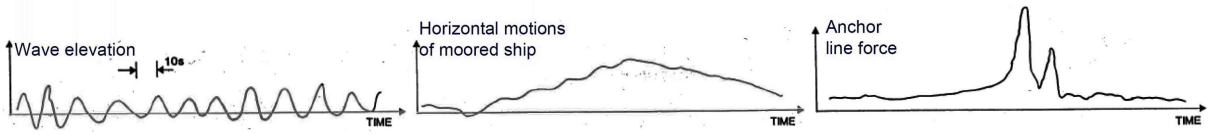

Figure 9.3: Varying drift forces in an irregular seastate cause slow low frequency motions of the moored ship that trigger peak loads on the mooring system (Greco, 2018)

It is generally required to solve not only the first order velocity potential ϕ_1 but also ϕ_2 when estimating sum- and difference frequency loads. The solution of ϕ_2 is however not straight forward, as the loads are usually much smaller than the first order solutions and the estimation of these loads comes at a higher computational cost. The relevance of the solution of ϕ_2 will however be discussed later. Assuming the first- and second order velocity potential is known, the slow drift excitation loads following Faltinsen (1993) are formulated in equation 9.4.

$$F_i^{SV} = \sum_{j=1}^{n}\sum_{k=1}^{n} \zeta_{a.j}\zeta_{a.k}\left[T_{jk}^{ic} cos[(\omega_k - \omega_j)t + (\epsilon_k - \epsilon_j)] + T_{jk}^{is} sin[(\omega_k - \omega_j)t + (\epsilon_k - \epsilon_j)]\right] \quad (9.4)$$

The coefficient $\zeta_{a.i}$ in equation 9.4 represents the incident wave amplitudes, ω_i the wave frequencies, ϵ_i the random phase angles and n the number of wave components used to describe the irregular seastate, as mentioned in the description of the deep water first order velocity potential in equation 8.11. The coefficients T_{jk}^{ic} and T_{jk}^{is} can furthermore be interpreted as the transfer functions of the second order drift loads, as they are independent of the incident wave amplitude ζ_a and give the amplitudes of the *cosine* and *sine* part of the loads, hence the superscripts c for *cosine* and s for *sine*, per unit incident wave amplitude, similar to a RAO (Faltinsen, 1993). The expression above contains both the mean drift- and difference frequency loads.

Estimating the second order transfer functions T_{jk}^{ic} and T_{jk}^{is} nevertheless requires the solution of ϕ_2. Newman (1974) however offers a simple solution to this dilemma. He realized that T_{jk}^{ic} and T_{jk}^{is} do not change much with frequency and that the most interesting results, motions of large period, occur when $\omega_k - \omega_j$ is small. The second order transfer functions can henceforth be estimated with reasonable accuracy with T_{jj}^{ic}, T_{kk}^{ic}, T_{jj}^{is} and T_{kk}^{is} using Newmans Approximation, which is formulated in equations 9.5 and 9.6.

$$T_{jk}^{ic} = T_{kj}^{ic} = 0.5(T_{jj}^{ic} + T_{kk}^{ic}) \quad (9.5)$$

$$T_{jk}^{is} = T_{kj}^{is} = 0 \quad (9.6)$$

Although Newmans Approximation is greatly reducing the necessary computational effort, the summation of the frequency terms of equation 9.4 is still time consuming. There are furthermore other flaws in this method, as is the case for oscillations near the natural heave period together with small heave damping, as can be the case for SPAR platforms as the natural periods are large but sometimes not as large as horizontal motions. In this case are large motions likely to occur. Greco (2018) also points out that Newmans Approximation is generally not recommended for the assessment of vertical motions due to their relatively short natural periods.

9.4 Time Domain Simulation

The loads acting on the structure need to be translated into motions, velocities and accelerations to evaluate the structure's interaction with the seastate on the one hand and to derive other information, such as mooring line tensions, on the other. As mentioned above is this done by finding the equilibrium of forces in the EOM. The probably most instinctive way to do this is by evaluating the structure's response at every time instant, ergo in the time domain. The EOM is solved at every time step of the predefined duration of the simulation giving excitation forces and body motions at every time instance.

The structure is subjected to the environmental loads such as wind, waves and current. Especially the former is varying in time and hence applied as a random sequence of wave heights, -periods and -phases, governed by the wave spectrum, onto the structure. This offers the possibility to capture effects neglected by other methods, such as transient effects, and enables a more precise estimation of body motions if added mass and damping are strongly frequency depended. Furthermore are time domain simulations able to incooperate higher order loads into the solution. Not only can second order effects be captured but also the instantaneous friction damping acting on the structure.

The method is hence able to produce very accurate and reliable results, given that the boundary conditions are chosen correctly and the environment, such as the seastate but also wind and currents, is defined with sufficient precision. This level of detail however comes at a cost. The designer must be in full control of the parameters involved to judge the accuracy of the simulation and must furthermore be aware of the duration a time domain simulation needs in order to present reliable results. Multiple factors influence this duration: For one needs the time step to be chosen small enough for the change between two subsequent steps to be small enough in order for the solution algorithm to converge, which has a fundamental impact on the computation time used. For another must the time simulation be chosen long enough. The reason here is for one to reduce the statistical uncertainty of the results, ergo to allow for a sufficient amount of motion- or load peaks to accumulate, and for another to cut out the *transient phase* at the beginning of each simulation. The transient phase is the time span during which the influences of the body being previously at rest are noticeable, ergo when steady state phenomena, such as long period motions, did not fully establish yet. The time used to conduct a time domain simulation is further increased by the necessity to conduct multiple simulations with identical boundary conditions but different random arrangements of waves to further decrease the statistical uncertainty. The best results are hence generated by an infinite number of simulations all being infinitely long with an infinitesimal short time step. This is impossible, hence is it up to the designer to judge at which point the simulation is considered sufficiently accurate.

9.5 Frequency Domain Simulation

Estimating the wave body interaction in frequency domain is a way to quickly gather data on the motion characteristics of a floating body. To solve the EOM in frequency domain must linear theory be applied as the response of the structure is assumed to be linearly proportional to the wave height. Instead of solving the EOM at every time instance is the EOM solved in frequency domain, ergo is the structure's response oscillation calculated for a number of excitation oscillations. Hence is the response the product of an input and an operator as is pictured in figure 9.4. The graphic shows how the an external oscillation causes an internal oscillation. The nature of the response oscillation depends on the operator used to translate the exciting oscillation into the response oscillation. Applying this principle to the WBI between a wave and a floating structure can the input on the left be seen as a regular wave and the output on the right as the resulting oscillation of the structure.

Only analyzing regular waves one by one is however not sufficient since a seastate is a culmination of different regular waves. The solution can be expended by the principle of superposition. The way a seastate can be represented as the superposition of a number of regular waves can the output, the motion response of the structure, be represented as the superposition of the

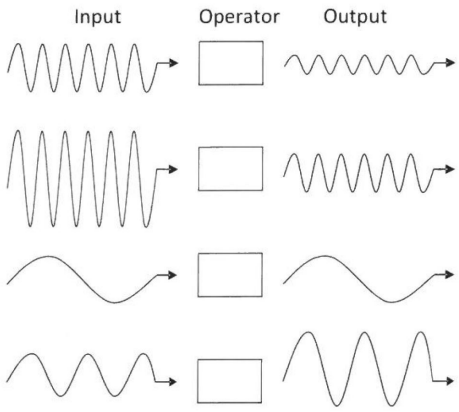

Figure 9.4: The principle of the frequency domain wave body interaction estimation is presented as an operator translating an input into an output (Rosén, 2017)

individual response of the structure to the individual regular waves. Ergo is the linear response of a body to a wave spectrum ($S_\zeta(\omega)$) described with a motion response spectrum ($S_R(\omega)$). Both are connected by a so called response amplitude operator (RAO), sometimes also denoted transfer function ($H(\omega)$), refered to as the Operator in figure 9.4. A RAO defines the structure's response per unit wave amplitude at a certain frequency in the DOF in question. RAOs however only exist in a specific DOF, if the motion in question engages a restoring load, ergo is a RAO in surge for a freely floating structure non-existent due to the missing restoring force.

The way $S_\zeta(\omega)$, RAO and $S_R(\omega)$ play together can be seen from figure 9.5. The wave spectrum on the left $S_\zeta(\omega)$, the RAO in the middle and $S_R(\omega)$ on the right. The RAO already indicates that waves of a wave frequency $\omega \approx 0.55\ \frac{rad}{s}$ cause the largest motion response of the structure which is proven by $S_R(\omega)$ on the right. It is important to notice that the response to the wave carrying the most energy within $S_\zeta(\omega)$ is not dominant. It is hence vital to know the shape of both the structure's RAO and $S_\zeta(\omega)$ at the OS.

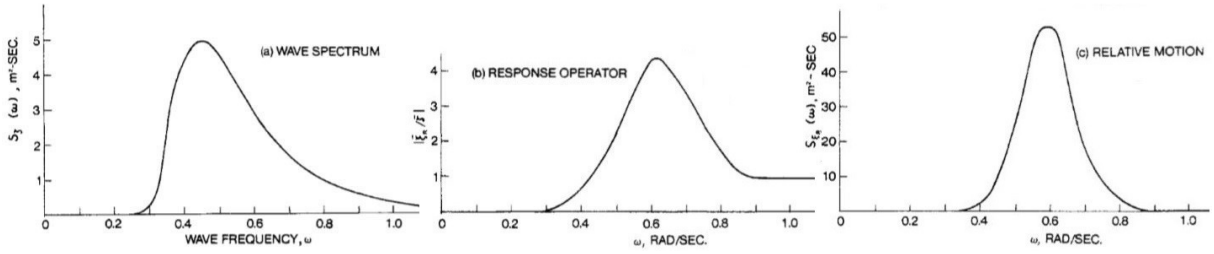

Figure 9.5: The response spectrum $S_R(\omega)$ on the right is the result of the interaction of the the wave spectrum $S_\zeta(\omega)$ (left) and the RAO depicted between the two (Lewis, 1989)

RAOs can be found by different methods which nevertheless all employ the same mathematical principle: A RAO is the ratio between the response amplitude (η_j) divided by the incident wave amplitude ζ_a and can be calculated as the square root of $S_R(\omega)$ divided by $S_\zeta(\omega)$. While $S_\zeta(\omega)$ is relatively easy to define by either measuring a seastate out at sea or applying a JONSWAP seasate description, the estimation of $S_R(\omega)$ is much more complex. It can either be measured by conducting model- or full-scale trials, or it can be estimated using mathematical models such as linear potential theory. The bodie's response is calculated as the real part of the

solution of the EOM for every frequency in $S_\zeta(\omega)$ and applied to the relevant rigid body motion using equation 9.7 and the coordinate system defined in figure 9.1.

$$s = \eta_1 i + \eta_2 j + \eta_3 k + \omega x r \quad with \quad \omega = \eta_4 i + \eta_5 j + \eta_6 k \quad and \quad r = xi + yj + zk \tag{9.7}$$

The response amplitude is linked to the damping of the structure. Unfortunately is damping one of the more vague estimations, especially when using potential theory as it only regards potential damping, entirely neglecting viscous damping. Furthermore become the response characteristics of a system increasingly nonlinear the higher the response amplitude. Linear theory can in this sense only give an indication about the amplitude of the response. On the other hand can it more importantly indicate the frequency band within which large response amplitudes of the structure are to be expected.

The frequency band resulting in large response amplitudes is around T_n of the motion in question. The knowledge of T_n is hence important as it decides if a structure is suitable for a specific location or condition. Avoiding incoming wave frequencies close to T_n is vital since this could trigger large amplitude resonant motions hindering operations and possibly damaging the structure. T_n is calculated solving the EOM omitting excitation- and damping forces acting on the body, as damping at T_n is considered small. Equation 9.8 shows how T_n for an uncoupled and undamped structure can be calculated using the mass of the structure (M_{ii}), the added mass in the respective motion (A_{ii}) and the engaged restoring coefficient (C_{ii}). As with the RAOs are there no T_n for unmoored structures in surge, sway and yaw (Faltinsen, 1993).

$$T_{ni} = 2\pi \left(\frac{M_{ii} + A_{ii}(\omega)}{C_{ii}} \right)^{\frac{1}{2}} \tag{9.8}$$

10 Mooring

Position keeping is an integral part of any offshore installation. Time brought forth a multitude of position keeping techniques, divided into static- and dynamic positioning systems. Dynamic positioning systems utilize thrusters and position-coordinates to actively counteract environmental influences such as wind, waves and current that force the floating body from its desired position. Passive positioning systems on the other hand are installations physically connecting the body to the seafloor with anchors and mooring lines. This study focuses on the later method due to economical reasons and the absence of energy to power thrusters on the floating structure. Figure 10.1 depicts a range of mooring arrangements which present reasonable mooring-solutions for the floating structure.

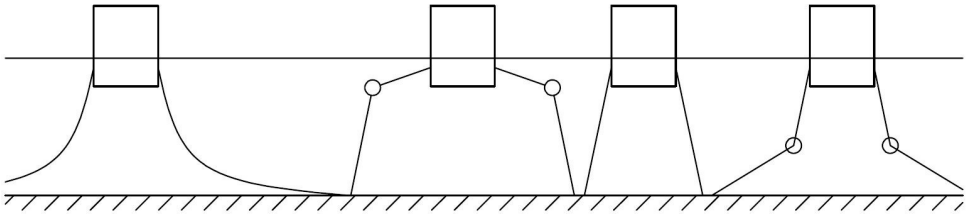

Figure 10.1: Typical mooring systems used for offshore installations (e.g. Marine Energy Devices). From left to right: Catenary system, taut line mooring system with subsurface floaters, taut line mooring- and clump-weight mooring system (Weller et al., 2013)

The mooring system keeps the structure's position by the introduction of a restoring force. This restoring force introduces oscillatory motions and the corresponding problems into the system, since resonance phenomena can be excited. The oscillatory behavior can however be influenced by the mooring system too as it also introduces damping to the system. Chakrabarti (2005) already emphasized that "It is essential that floating offshore vessels have fit-for-purpose mooring systems", which extends the task of mooring systems beyond station keeping and controlling of natural frequencies. This is especially the case if the structure's OS is in the vicinity of other applications, as is the case in this project. The floating structure is operating in close proximity to the algae- and mussel collectors, cramped between the shoreline of Kiel-Holtenau and the shipping route guiding traffic in and out of the Bight of Kiel. The specific requirements on the mooring systems are, in no particular order, the following:

- *Layout*:
  The mooring system is not to collide with any of the other installations at the OS. Further is the mooring-footprint required to stay within the area granted to the operations of the OFK

- *Strength*:
  The mooring system is to be strong enough to weather the survival condition. The breaking strength of each member of the mooring arrangement has to be well above the expected loads

- *Damping and Stiffness*:
  The damping of the mooring arrangement has to be high enough to limit the horizontal and vertical motions of the structure to an acceptable amplitude while the stiffness has to be calibrated in a way to avoid the natural frequencies to be within the range of the expected seastates

The development of the mooring arrangement is initiated with the geometrical restriction present at the OS. For one is the mooring footprint not to be greater than a 50 m radius. The second requirement is for the mooring line to quickly reach a depth of > 6 m, in order to avoid conflict with the mussel collectors surrounding the structure. Other factors influencing the mooring arrangement are weight, investment cost and maintenance. Two of the requirements already exclude the subsurface floater mooring arrangement and the catenary system, since the buoys would interfere with the mussel collectors and the catenary lines would require a footprint far greater than 50 m. Following Chakrabarti (2005) is the horizontal stretch a catenary mooring line covers five to ten times as large as the water depth. Ergo would the anchor be at least 460 m of the side of the structure, given the water depth of 12 m at the OS, and therefore out of the allowed mooring footprint. Furthermore would the weight of the catenary mooring chain be critical for the structure's hydrostatics, keeping in mind that the structure's freeboard is only 36.6 cm.

The mooring arrangements remaining from figure 10.1 are a taut line- and a clump-weight (CW) mooring system. Both have the advantage of a reasonably small mooring footprint and limited interference with the installations surrounding the structure. The taut line mooring is however not suited for the OS due to another reason: Taut mooring, especially when installed using synthetic-fiber lines, absorb the imposed dynamic motions through an elongation of the lines. Synthetic-lines have the capability to extend significantly without causing excessive dynamic tension (Chakrabarti, 2005). This is however only possible if the mooring line is of sufficient length in order for the imposed motions to be small compared to the total line-length, which is not the case given the water depth at the OS. The inadequacy of a taut mooring system becomes in this regard obvious when recalling that the water level is likely to change with an amplitude of up to 2 m, depending on the wind conditions, something a taut mooring system at such a water depth is unsuited for.

The remaining mooring arrangement is ergo the CW mooring system. The concept of this mooring arrangement is presented in figure 10.2 showing the structure attached to the mooring system, which quickly reduces the vertical extent of the mooring lines below the 6 m threshold. The water depth is 12 m and the anchors are 50 m apart. The structure is uniformly moored with the mooring lines attached to fairleads at the four corners of the working platform, as depicted in figure A.1 in appendix A.

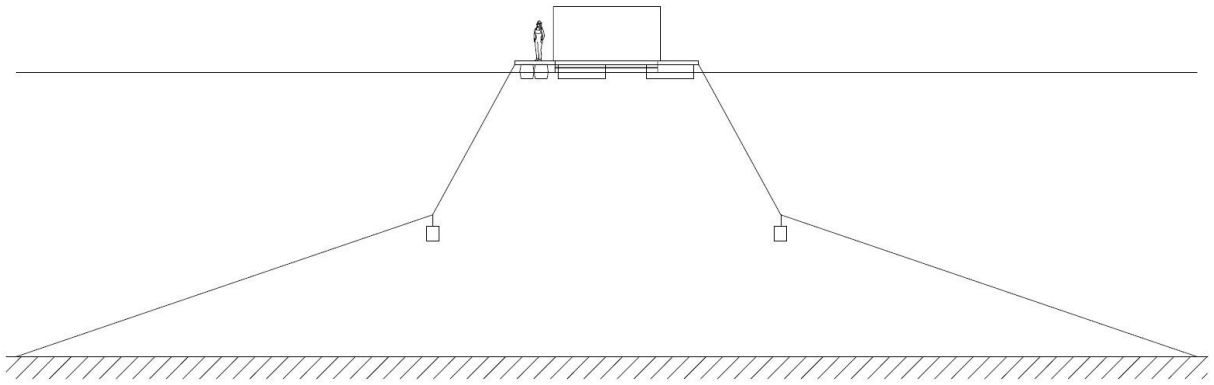

Figure 10.2: The clump-weight mooring system attached to the structure at a water depth of 12 m *with the anchors being* 50 m *apart. The CWs quickly lower the mooring line below the* 6 m *threshold*

There are however further considerations that need to be made. One is that the OFK requires the part of mooring line from the CW upward to be of steel chain. Experience has shown that the high number of load-cycles the mooring line goes through is leading to a fast accumulation of fatigue damage in the connection between mooring line and CW. The connection between mooring line and CW is however a much more resilient one, if the upper part of the mooring line is made from steel chain, ergo if the CW can directly be spliced into the steel chain. A further noteworthy advantage is that the chain simplifies regular maintenance. Pulling up the mooring line is much easier if the maintenance vessel's crane hook can be placed into the chain links to pull up the mooring line little by little, until the connection between synthetic mooring line and chain is reached at the location of the CW, as this connection needs to be checked regularly for wear. This requires the chain to be a long link chain type to assure that the crane hook fits easily into the chain links. Another requirement is the weight of the CW. For one, as pointed out earlier, is the capacity of the structure limited. More importantly however is that a CW weighting more than 100 kg cannot be handled by the maintenance vessel of the OFK and would require for external personal to lift and deploy the CWs, which would be less profitable for the OFK. Table 10.1 lists the two mooring line components used in the present mooring line setup, ergo the synthetic line and the long link chain. The precise make-up of the mooring arrangement is found later in table 11.2.

Table 10.1: Mooring line lengths used for the present mooring arrangement

		Synthetic Rope	Long Link Chain
Length	$[m]$	26	8

Generally is the mooring system utilized for this structure unconventional and rather similar to anchoring of yachts and pleasure crafts. The anchors the structure is moored to the seabed with are helical anchors. These anchors consist of rods with helical threads on both ends of the rod and are drilled into the sediment. This anchoring method is chosen due to its limited impact on the ecosystem in the sediment, avoiding the costly implementation of ecological compensation areas required otherwise if concrete weights were to be used. The sealed seafloor area when using helical anchors is minimal. A further advantage is the loading capability, as the anchor is able to take both horizontal- and vertical loading, which is vital for the a taut-line mooring system. The capacity on the other hand is unknown due to the strong dependence on the seabed and the quality of installation.

Summarizing the information above: the mooring arrangement is made up from a helical anchor at the seafloor connected to a synthetic fiber line that ends at a CW. The CW marks the transition from the synthetic fiber line to the long-link chain that attaches to the fairlead on one corner of the structure.

11 Tools

The SESAM Software Package from DNV-GL is utilized to generate numerical results of the linear potential WBI and to carry out time domain simulations. The first version was published in 1969 by DNV and extended its application portfolio ever since. Figure 11.1 shows the structure of the SESAM package. The rough differentiation into a pre-processing-, a calculation- and a post-processing part makes the modular approach of the program obvious. The specific tools that are used in this thesis are marked with red.

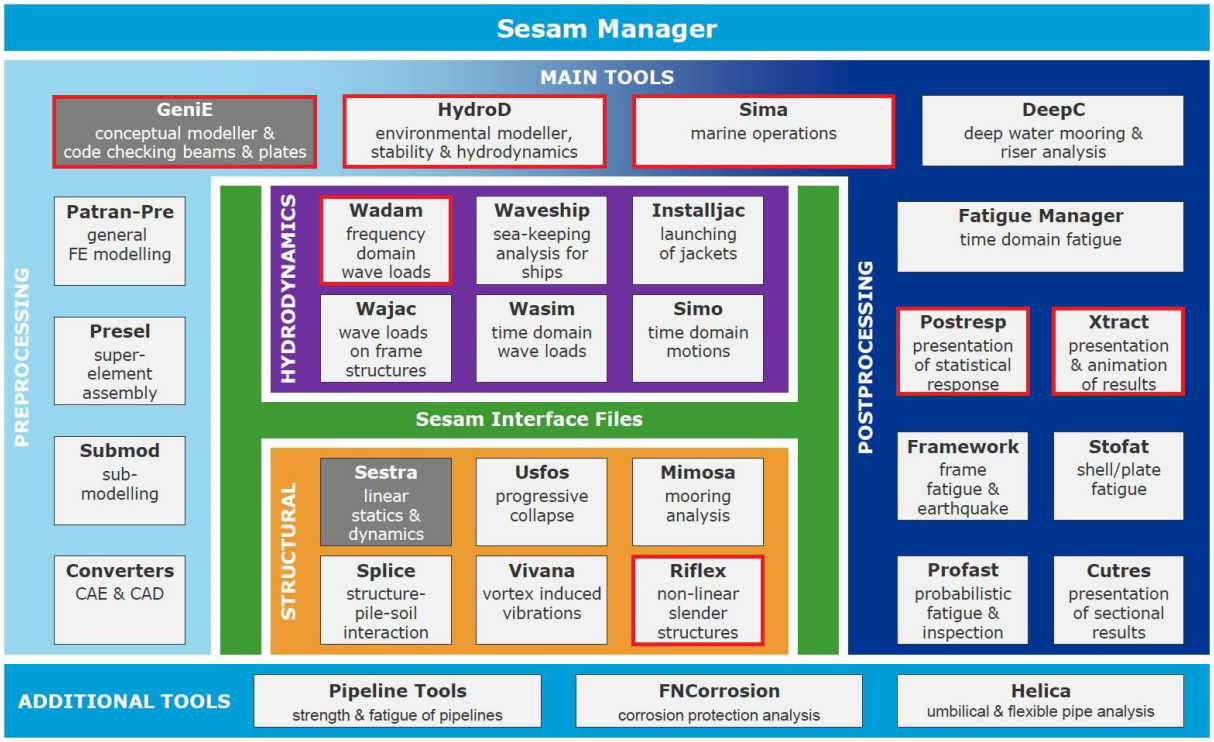

Figure 11.1: The SESAM tools that are used in this thesis are marked with red (DNV-GL, 2019)

The tool GeniE is the origin of every analysis since the geometry is created in this program. The program lets the designer assign material properties to the features of the model as well as it enables the implementation of point masses. The components mass and their global positions are defined in such detail to make the formulation of a mass matrix obsolete. It is furthermore important to place the origin of the model in the longitudinal and transversal center of gravity to ensure a good communication with the subsequent tool HydroD. Figure 11.2 shows the structural model of the floating farm. The frame structure as well as the floaters are designed from EN-Aw 5083 marine-grade aluminum. The structure of the greenhouse is designed from structural steel (St235) and the foil covering the flowerbeds from 0.12 *mm* PE80B plastic foil (Jahn, 2019). The point masses at the corners, marked as blue spheres, are accounting for the flowerbeds and plants, which are not modeled. Two errors are hereby committed: for one alters the negligence of the flowerbeds the friction damping of the structure, which can however be tolerated as the loads on the structure are diffraction dominated, given the small wave height compared to the structure's dimensions. For another changes the definition of point masses at the inner corners of the structure the moment of inertia, increasing it from the correct value. This shifts the structure's reaction in roll an pitch towards a slower response. The error hereby

committed is however considered small, given that the divergence from the overall moment of inertia is modest. The model that is created by defining materials and weights is referred to as the structural model, as it makes the calculation of the body's structural integrity possible. The later is however not attempted by this thesis. The structural model is here used only to represent the mass of the structure since this makes the definition of a separate mass matrix obsolete, as is previously pointed out.

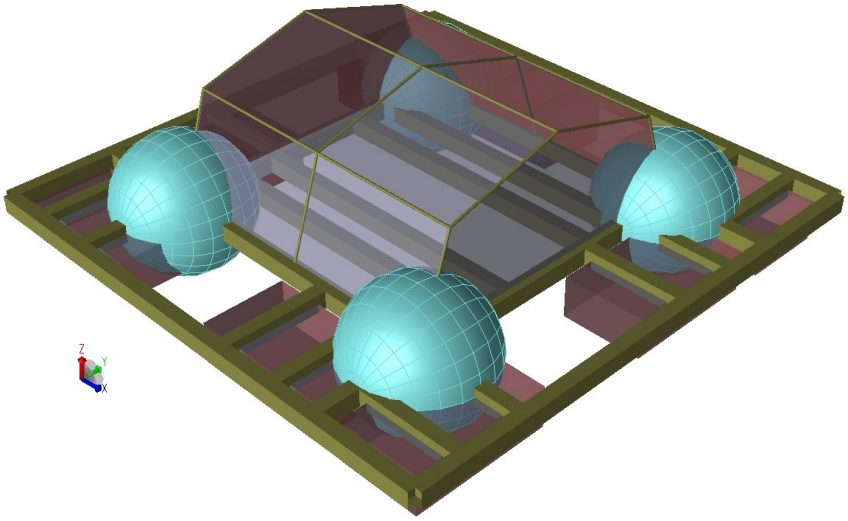

Figure 11.2: The structural model as it is designed in GeniE. The blue spheres represent the mass of the flowerbeds and the plants

The models created in GeniE are exported as Finite Element Method (FEM) models to HydroD. The FEM models are mass- and panel FEM models, for the definition of the structure's mass and the calculation of intact stability and WBI respectively. HydroD is the platform hosting the program Wadam to perform frequency domain analysis. Furthermore is the intact stability analyzed using HydroD. Working with HydroD is fairly straight forward, once the wizard functions are understood. The stability-wizard as well as the Wadam-wizard are used to calculate the intact stability of the structure as well as the linear hydrodynamic loads in frequency domain. The stability-wizard allows furthermore to account for heeling moments acting on the structure, in this case the wind heeling moment in the design- and survival condition. Moreover are offbody-points defined in HydroD to help with the visualization of the free surface surrounding the structure.

The offbody points are four-node shell elements and must be chosen small enough in order to properly model small wave frequencies, as the panel size greatly influences the minimum wave length that can be modeled. The smallest wave length that can be reasonably visualized by the offbody points using the chosen element size of 14.5 cm x 14.5 cm is $\lambda = 1.23$ m corresponds to a wave frequency of $\omega = 7.08$ $\frac{rad}{s}$, following the DNV mesh requirement for panel methods (DNV, 2010). Ergo can smaller waves not be accurately visualized given the current offbody-point definition. It is important to notice that the floaters appear 34% larger when looking at the free surface since the offbody-points do not exactly touch the floaters, a result of the offbody-point definition in HydroD.

The results calculated in HydroD are then exported to Postresp and Xtract for post-processing. Postresp allows the extraction of the RAOs as well as further relevant linear hydrodynamic coefficients such as added mass, potential damping and restoring coefficients. Xtract enables the visualization of the results, e.g the rigid body motions and the free surface elevation using the Wadam offbody-points around the structure.

Detailed analysis of the WBI and especially of the mooring arrangement is carried out in a Riflex coupled analysis. SIMO-RIFLEX is a powerful tool to analyze the nonlinear response of slender structures, such as umbilici, risers and mooring lines supported by a floating body interacting with a seastate. SIMO-RIFLEX permits two types of analysis to be carried out. The static analysis enables the evaluation of the equilibrium configuration of the floating body and chosen mooring arrangement interacting with the quasi-static forces such as current and wind. The second analysis is the dynamic analysis allowing for motion response analysis of the floating body and mooring system interacting with an irregular seastate. Further applications from RIFLEX such as an eigenmode analysis are possible but not engaged here.

11.1 HydroD Modeling

The modeling in HydroD is conducted using the wizard functions. Three wizards are used, two to calculate the design- and survival condition intact stability and one to estimate the linear WBI and the second order difference frequency transfer functions. The first step when using the stability wizard is the definition of the environment. Water, air- and wind parameters are set, prior to implementing the panel- and structural model. Table 11.1 presents the environmental conditions at the OS. Some values, such as the drag block coefficient and the drag coefficient, are left at the default parameter and can be found in Appendix B.

Table 11.1: The environmental information used for the HydroD intact stability calculations

Water		
Water Density ρ	1010	$\frac{kg}{m^3}$
Water Depth d	12	m
Wind		
Air Density ρ_{air}	1.225	$\frac{kg}{m^3}$
Wind Reference Height	10	m
Wind Profile Exponent	2	
Wind Speed (Design/Survival)	14.40/28.81	$\frac{m}{s}$
Drag Block Coefficient	$Default$	
Drag Coefficient Curve	$Default$	

The structural model accounts for the mass of the structure and contributes to the sail area. The panel model with the hydrostatic pressure applied all around the floaters, a HydroD requirement, is then rotated around the x-axis and the resulting stability properties are calculated at every degree of rotation. The x-axis is chosen as the structure gives the greatest obstacle to the wind if the wind is blowing along the y-axis, ergo can the greatest heeling moment be expected around the x-axis. The wind heeling moment is also calculated by rotating the model around the x-axis and evaluating the wind heeling moment every 5°. The results are extracted using the report function which generates a list of the results which again can be read using Excel.

The procedure to estimate the linear WBI is slightly different. The Wadam-wizard uses the same environmental information as the stability wizard does, except the information about the wind. It requires furthermore the definition of a frequency- and a direction set. The frequency set defines at which wave-frequency intervals the linear WBI is to be estimated. The first frequency was chosen to be 0.05 $\frac{rad}{s}$ going up to 10 $\frac{rad}{s}$ in 0.2 $\frac{rad}{s}$ steps. The frequency band around the design- and survival wave frequencies $\omega = 2.65$ $\frac{rad}{s}$ to $\omega = 3.49$ $\frac{rad}{s}$ however was refined with $\Delta\omega = 0.1$ $\frac{rad}{s}$ steps to resolve the frequency band the peak wave loads are expected in with greater precision. The direction set is going from 0° to 360°. This is for one representing the response of the structure in all direction and furthermore making the validation of the results much easier. Although a direction set from 0° to 180° is sufficient given the square shape of the structure is the whole 360° range analyzed. This makes it possible to compare the hydrodynamic coefficients, e.g. added mass for roll and pitch with each other, examining their symmetry behavior and checking for errors in the results.

The second order results are calculated by specifying a far field integration, which is convenient as it does not require a water surface description. This allows the calculation of difference frequency loads, while omitting sum-frequency loads, which can nevertheless be tolerated, as is pointed out in section 9.3. HydroD is using the far-field- or momentum-conservation method to estimate the drift loads on the structure and then applies Newmans Approximation to estimate the second order difference frequency wave load transfer functions. The required CPU time is substantial, hence are only uni-directional waves regarded in the calculation. The purpose of this calculation is to import the second order transfer functions into SIMO to estimate low-frequency body motions of the moored structure. In comparison to HydroD however will the structure in SIMO be loaded only from one direction, ergo is the second order load approximation using only uni-directional waves sufficient.

The results of the Wadam-wizard are extracted using Postresp. The program allows the display of the results as well as the extraction of the results in list format. The later allows the implementation of these results into Excel for data post-processing. A handy tool for post-processing is the WADAM1.LIS file created by Wadam. This file collects all the information used to calculate the WBI results. Specific parameters and coefficients, e.g. the restoring coefficients C_{ij}, can be read from this file. The WBI is then displayed either as a scalar value, as for the frequency independent restoring coefficient C_{ij}, or as a parameter changing over the wave frequency range, such as added mass. Furthermore can other parameters like the natural period at a certain ω be calculated from this data using equation 9.8.

11.2 Panel Model

Panel methods, also referred to as boundary element methods, represent the structure with a combination of sources and sinks distributed over the mean whetted surface of the structure. Sources and sinks are mathematical singularities that define points with a flux out of- or into a point, hence the term. Panel methods assume potential theory, which limits the applicability of these methods, as potential theory can only be applied with good accuracy, if the wave oscillation amplitudes are small relative to the structure's cross section. Flow separation and other viscous effects are neglected limiting damping, reducing it to potential damping only. Damping is hence depending only on the waves radiated from the body due to the forced body oscillation (Faltinsen, 1993).

The panel model is designed in GeniE and a mesh applied to the surfaces of the structure, ergo the floaters and the greenhouse, since the greenhouse is contributing majorly to the sail-area of the structure. The outer surfaces of the floaters are assigned a wet surface property as well as a dummy pressure as the first and only loadcase in GeniE. This dummy pressure is vital for the subsequent analysis in HydroD, as it indicates the location of the whetted surface area. HydroD is able to generate the mean whetted surface given the information from GeniE and the loading condition specified in HydroD. Figure 11.3 depicts the panel model as it is used in the Wadam calculation. It clearly shows how the body is cut of at the design waterline, emphasizing how potential theory only regards the mean whetted surface area.

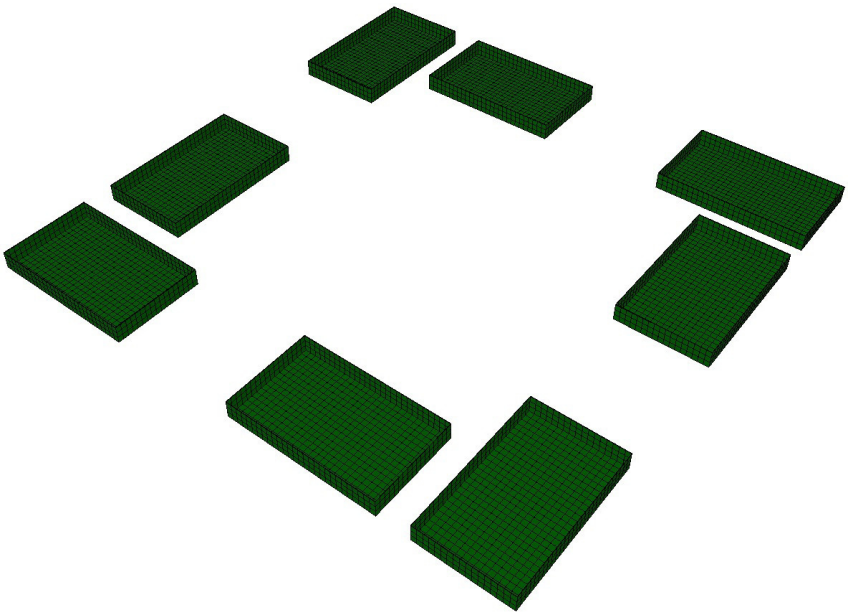

Figure 11.3: The panel model as it is used in HydroD to calculate the linear hydrodynamic coefficients. The mean whetted surface is shown on all floaters which move together as a rigid body

11.2.1 Meshing

The element size is of up-most importance for any FEM applied. The size of the mesh is a compromise between accuracy and CPU expense, thus the computation time used. The denser the mesh, the better is the geometrical representation, the more accurate are the results. The panel mesh size is chosen following DNV-RP-C205 (DNV, 2010) which recommends the diagonal of the biggest element to not be greater then a sixth of the smallest incoming λ. The wave spectrum applied spans from $\omega = 0.05\ \frac{rad}{s}$ to $\omega = 10\ \frac{rad}{s}$ resulting in the smallest wavelength to be $\lambda = 0.616\ m$. Ergo is the maximum element side length (ESL) set to 72 mm.

A sufficient mesh density is tested by conducting a mesh convergence study. Figure 11.4 shows the principle of mesh convergence. The accuracy of a result parameter, e.g. the restoring coefficient of a floating body, is not improving significantly after a certain stage of mesh refinement is reached. Further increasing the mesh refinement will only increase the CPU time without giving significantly more accurate results. When a sufficiently dense mesh is reached depends on the designer. In this case is a 5% rule applied, ergo is the mesh considered accurate enough, if the increase in accuracy between two subsequent mesh-refinement steps is below 5%.

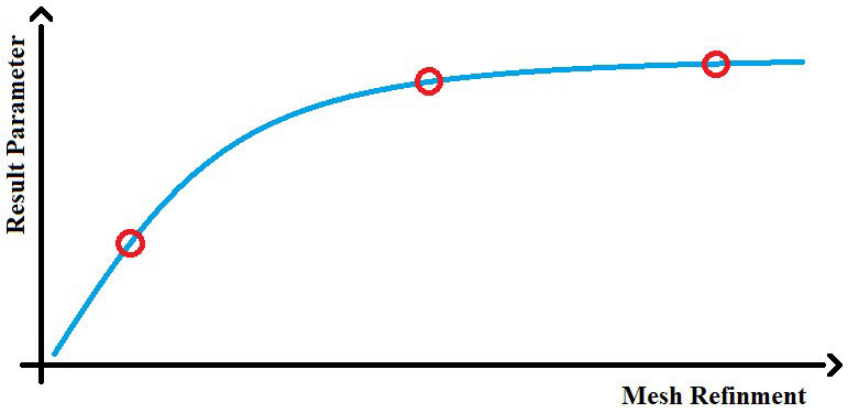

Figure 11.4: The graph shows how the accuracy of the parameter is not significantly improving after a certain mesh refinement is reached. Further mesh refinement only increases CPU time without significantly improving the results accuracy

The mesh convergence study is performed on the RAO in heave. This is benefitial as this allows the evaluation of the mesh over the whole wave frequency range. The mesh refinement is especially important when analyzing small λ, as pointed out by DNV (2010). The mesh elements where reduced in three steps from an ESL of 600 mm to 50 mm. A smaller ESL is not possible with the given setup, since the maximum number of elements HydroD can handle is 50 000 elements. To further reduce the number of elements for this study is the greenhouse omitted.

Figure 11.5 shows the development of RAO_{33}. The graphs for the course panel mesh and the fine mesh are essentially indistinguishable for low wave frequencies, yet is the difference growing the higher the wave frequency. The difference between the finest mesh and the medium mesh with an ESL of 72 mm is however small throughout the whole wave frequency range. The medium ESL of 72 mm is hence chosen linear WBI calculations within HydroD.

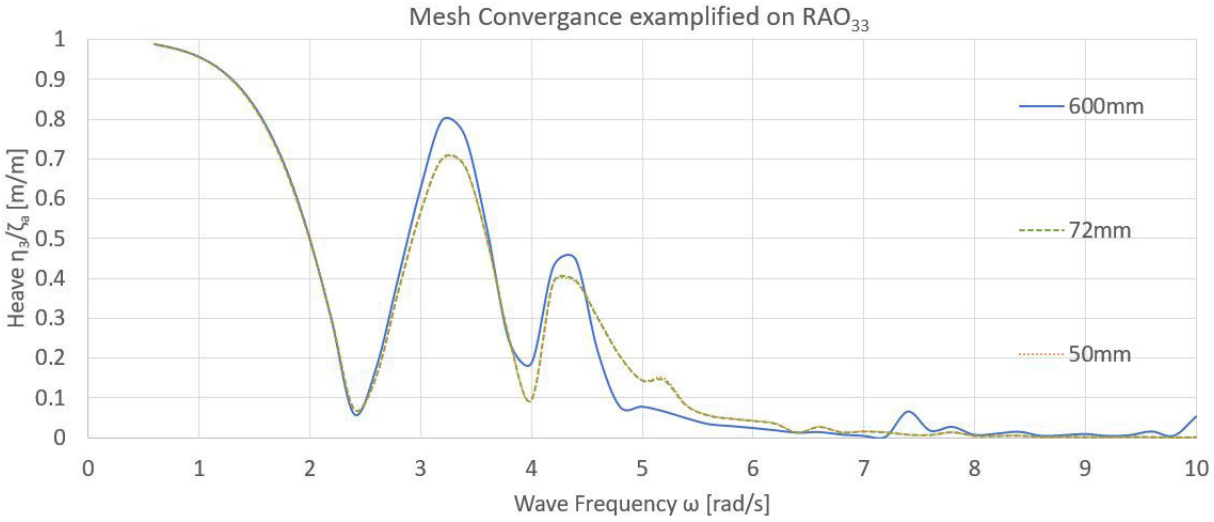

Figure 11.5: Three meshes are compared against each other on the example of RAO_{33} over the whole wave frequency range. The coarsest panel mesh with an ESL of 600 mm (blue), the medium mesh with an ESL of 72 mm (green) and the finest mesh with an ESL of 50 mm(orange)

The mesh chosen to calculate the linear WBI in HydroD is presented in figure 11.6. The mesh is applied to the floaters as well as to the greenhouse, the later is to calculate the wind heeling moment when assessing the intact stability of the structure in the design- and survival condition. Further are quad-elements enforced for two reasons: first of all is the structure suggesting this element formulation, since most surfaces are rectangular. Second of all are quad elements, if applied on a suiting structure, resulting in a very orderly mesh and clean elements. Each element and therefore the mesh is hence less prone to error and giving more accurate results. Furthermore are higher order elements used to represent the geometry. The difference when using higher order elements is that the nodes used to calculate the elements response are not only located at the four corners of the element but also at the midpoints of the sides connecting the corner nodes. This comes at the price of a higher CPU time but improves the accuracy of the computation. The mesh used in the subsequent calculation presented in figure 11.6 uses 23888 elements at 68029 nodes, including 1868 beam elements representing the structural model (not shown).

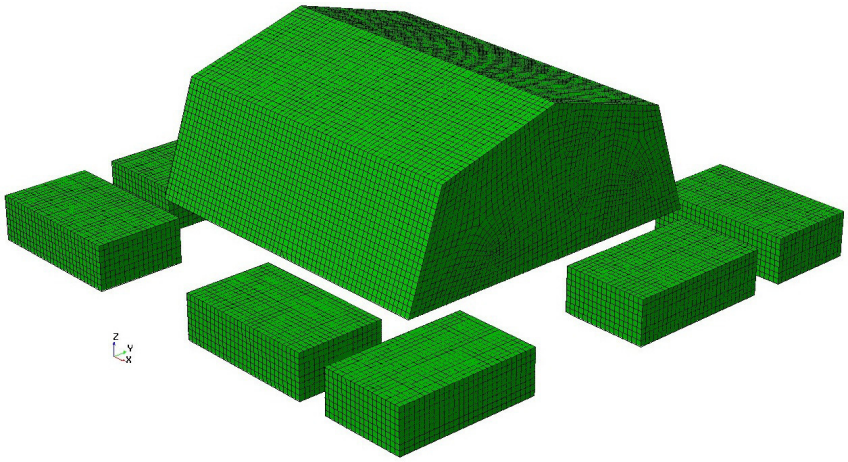

Figure 11.6: The panel mesh as it is used in HydroD. The max. ESL of each element is 72 *mm. A total of* 23888 *elements at* 68029 *nodes is used*

11.3 SIMO-RIFLEX Modeling

The accurate modeling of a moored structure interacting with a random seastate and other environmental loads, such as wind and current, is done in time domain. The method chosen is in this case a coupled RIFLEX simulation, ergo a simulation of a floating body connected to a slender elastic structure, the mooring arrangement, in an marine environment. The *coupled* term refers to the two mechanisms at work. SIMO is used to calculate the rigid body motions caused by the environmental loads while RIFELX applies the same environmental loads together with the loads resulting from the rigid body motions onto the slender structure and feeds back this response to SIMO to adapt the rigid body motions.

The information about the floating body is drawn from HydroD, which includes not only the mass- and stiffness matrix but also the frequency dependent added mass- and damping matrices. Analog are the first- and second order motion transfer functions imported into the body description. SIMO is using this data to define a retardation function based on the frequency dependent added mass of the body which is vital for time-domain simulations. Ogilvie (1964)

declared the free surface as the "memory of the physical system", as the current event influences all later events. Cummins (1962) showed a way on how to implement the retardation function in the EOM in order to discretize it in time domain, thereby giving the solution this memory, allowing events in the past to influence current and future reactions of the structure.

The floating body is connected to the slender structure, here the mooring system, using a *slender system connection*. The motions of the floating body and the slender structure are channeled back and forth through the slender system connection. The slender element system itself is described by a series of supernodes connected by a specified mooring line, which again is defined by a set of cross sections. The supernodes are defined as either free or slaved in specific locations of the predefined environment. As an example are the anchor-supernodes defined at the seafloor, while the fairlead-supernodes are defined as slaves to the slender system connection at the four corners of the platform. A typical setup of a slender system is shown in figure 11.7, which depicts a slender structure made up from supernodes, elements, segments and lines.

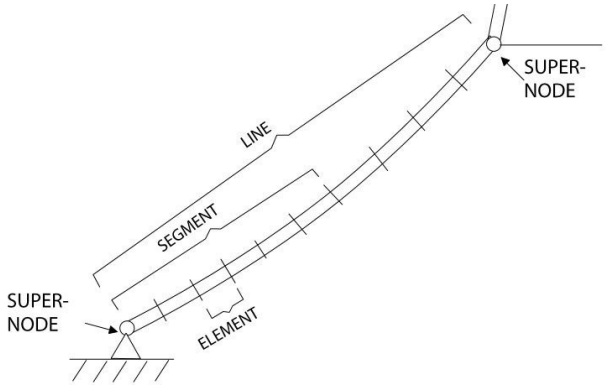

Figure 11.7: A typical setup of a slender system in RIFLEX composed of supernodes, elements, segments and lines, taken from SINTEF-Ocean (2018)

The slender system relies on a finite element (FE) approach that uses information from the predefined cross sections that allow the fully non-linear calculation of mooring line motions, forces and tensions. The system is hence defined by a number of elements with specific properties embedded in the cross section defined. The cross section definition itself grants non-linear behavior, e.g. by the definition of non-linear material parameters. The FE method to calculate deformation and stresses relies on the small-strain theory, ergo the approach that the deformation of the structure, in this case the element, is small compared to the dimension of the element.

The use of small-strain theory together with a CW mooring system, as it is used in this thesis, justifies the implementation of long elements since the overall curvature of the mooring lines is considered small, which is typical for taut line mooring systems. Ergo is the expected bending of the slender elements in the chosen mooring arrangement small compared to a catenary mooring, ensuring small curvatures and therefore allowing an element length of 2 m. The mooring line consists, as described in section 10, from the anchor upward out of 26 m synthetic mooring line weighting 1 $\frac{kg}{m}$, a CW weighing 100 kg (70 kg when submerged) and 8 m mooring chain weighting 5 $\frac{kg}{m}$. The specififcations of the components used in the mooring line are captured in table 11.2.

Table 11.2: Mooring line component specifications as specified by Engel-Netze (2019)

	Mass Coefficient $[\frac{kg}{m}]$	External Area $[\frac{mm^2}{mm}]$	Gyration Radius $[mm]$	Axial Stiffness $[\frac{MN}{m}]$	Tension Capacity $[kN]$
Synthetic Rope	1	314.2	5	0.379	68.3
Long Link Chain	5	530.9	6.5	807.5	392.4

The simulations carried out in SIMO are structured into a static- and a dynamic step. The static step is carried out to find an equilibrium position of the body and the slender element structure subjected to the static environmental forces, in this case mass-, current and wind forces. The environment is specified by means of a wave spectrum, a current profile and a wind force derived from the wind profile as is specified in section 8.2. The static equilibrium is vital for the subsequent dynamic calculation. Its aim is to find an equilibrium between mass-, volume-, current- and wind forces acting on the slender system and the floating body. This requires an initial- and static position of the defined supernodes, in this case the anchors, as the iteration of the equilibrium position needs to start from a stress free configuration, which is defined by the initial position. The node will then, during the iteration, move to the predefined static position, changing the shape of the mooring line as the line settles into its neutral position thereby approaching the static equilibrium.

The process of finding the static equilibrium is iterative. RIFLEX enforces a Newton-Raphson method to find the equilibrium, ergo to balance the forces interacting with each other, e.g. mass- and buoyancy. The starting point of such an iteration is vital and has a large influence on the convergence rate. RIFLEX is hence performing caternay-calculations prior to the iteration procedure. The catenary-calculation quickly gives a good starting point for the static equilibrium iteration, non regarding it neglecting the bending stiffness of the slender structure. The forces themselves are applied in a user defined order, steps and iterations. Furthermore is there a possibility to apply static forces which can either be used to balance the weight of the mooring arrangement or to conduct a motion decay test when performing the dynamic analysis.

The dynamic analysis in RIFLEX allows the study of natural periods, mode-shapes and dynamic loads acting on a slender structure connected to a floating body and is recommended if transient effects are important or if added mass and damping are strongly frequency dependent. A dynamic analysis is usually realized by integrating the EOM in time. RIFLEX uses the numerical integration scheme Newmark-β, governed by the factors γ and β, to solve the EOM in time domain. The later two factors have a drastic influence on the stability of the scheme. The method is either explicit or implicit, depending on the values of γ and β. This thesis uses the implicit *Constant Average Acceleration* method with $\gamma = \frac{1}{2}$ and $\beta = \frac{1}{4}$. As the name already indicates is the acceleration assumed to be constant between two discrete points in time, which results in an undamped unconditionally stable scheme that is beneficial for the convergence of this simulation.

The full non-linear integration of the EOM in time has the aim to gather information on the system state represented by acceleration $\ddot{r}$, velocity $\dot{r}$ and displacement r at a time $t + \Delta t$, from which all necessary information (forces and stresses) can be derived from. The procedure follows three steps: The first step consists of the establishment of the initial conditions of the three system states $\ddot{r}$, $\dot{r}$ and r at $t = 0$. The subsequent step calculates the three system states

at $t + \Delta t$ as a response to the momentary dynamic load vector based on the constant average acceleration. This is done by using a linearized incremental EOM by implementing tangential mass-, damping and stiffness matrices. These results must however not be correct since e.g. added mass and damping strongly depend on the the system state and are hence not linear, leading to an imbalance in the dynamic equilibrium equations. Ergo is an Newton-Raphson iteration performed on these equilibrium equations by introducing a displacement correction and altering the tangential matrices mentioned above accordingly, until an equilibrium is reached. The resulting system state $\ddot{r}$, $\dot{r}$ and r at $t + \Delta t$ are then, in the third step, implemented as the initial condition for the next time step.

The dynamic load vector mentioned above with which the floating body and the mooring system is interacting with is made up from the external loading; in this case the random seastate, the current profile and the wind force as defined in section 8.2. The seastate is defined by a JONSWAP wave spectrum and the current by the profile depicted in figure 8.6. Accordingly can a random seastate be realized in a time series by randomly creating waves of a specific height, period and phase, depending on their energy share defined in the wave spectrum. The generated random seastate depends on the wave seed number, which is by default set to one, ergo must this seed number be altered in order to generate multiple seastates of the same characteristic in terms of H_s and T_p but of difference appearance. This study generates ten random short-term survival seastates, each being one hour long. The total length of each seastate is however set to 4000 s in order to cut out the transient phase (set to 400 s) in the beginning of the simulation. Following DNV-GL (2015) is the duration of one time domain simulation (TDS) usually taken as 3 hours. However, since the required simulation length is governed by the number of maxima per unit time is the simulation time of one hour ($4000s$ minus $400s$ transient phase) considered reasonable. The body response is of a high frequency compared to conventional offshore structure, causing a sufficient amount of peaks to accumulate quickly, justifying a short TDS.

The relevant results of the time domain analysis are displacements and forces plotted against the simulation time. The post-processing of this data is done using the in-build post-processing tool allowing basic signal processing. Not only are low- and high pass filters applied but the program offers a Fast Fourier Transformation (FFT) to generate a response spectrum from the generated time series as a function of frequency. The FFT is in this context used to present a signal generated in the TDS (e.g. displacement or motion) in terms of frequency, which is convenient to compare TDS and frequency domain simulations. The spectrum generated with the help of the FFT can be analyzed further using the *root mean square* (RMS) value. The RMS represents the standard deviation within the spectrum and is a useful tool to characterize the response of a structure interacting with an irregular seastate. The RMS value can be directly calculated from the response spectrum using equation 11.1 (Rosén, 2017).

$$RMS = \sigma_\eta = \left(\int_0^\infty S_\eta(\omega) d\omega \right)^{\frac{1}{2}} \tag{11.1}$$

The RMS is not only used to describe motion- and acceleration limits, as is sometimes done for accelerations on the bridge of high-speed crafts, but also to compare the response to specific seastates with one another. The processed signal can then be exported to Excel for visualization purposes.

12 Resulting Intact Stability

Knowing the intact stability of the structure is immensely important for both the commission and the operation of the structure, as it shows the officials approving the farm that a save working environment is given and allows the operator running the farm to develop operational procedures. The stability will determine how and in which condition the farm can operate, as it e.g. limits the amount of gear that can be offloaded from the service vessel to the farm. The structure's stability is evaluated against the DNV-GL (2015) rules for stability for offshore structures to ensure the intact stability is adequate.

The intact stability is analyzed by implementing the panel- and the structural model into HydroD, as described in section 11. The structural model already carries all the information of the correct mass distribution given the embedded mass components embedded in the model, e.g. the greenhouse. Table 12.1 compares the initial stability calculated using the mass distribution in Excel described in section 6.4 and the results given from HydroD. The comparison shows a good agreement between both approaches. The small difference in deadweight (1.7%) is caused by the inaccurate representation of the beam structure, which causes the COG to be slightly lower in the HydroD model, resulting in a higher GM_0.

Table 12.1: The design loadcase as it is calculated by Excel and HydroD

	Deadweight $[kg]$	Displacement $[m^3]$	Draft $[m]$	COB (x,y,z) $[m]$	COG (x,y,z) $[m]$	GM_0 $[m]$
Excel	4592.7	4.538	0.234	(3.89, 0, 0.117)	(3.89, 0, 0.576)	29.3
HydroD	4514.0	4.469	0.233	(3.89, 0, 0.116)	(3.89, 0, 0.567)	29.7

The stability is estimated using the stability wizard as described in section 11. Figure 12.1 shows the GZ curve calculated by HydroD. The steep increase of the righting arm corresponds to the high GM_0 presented in table 12.1. The righting arm is decreasing after passing a heeling angle of 12° and reaching $GZ = 0\ m$ at 84°. This behavior is typical for a structure with such a low COG and such a wide waterplane area.

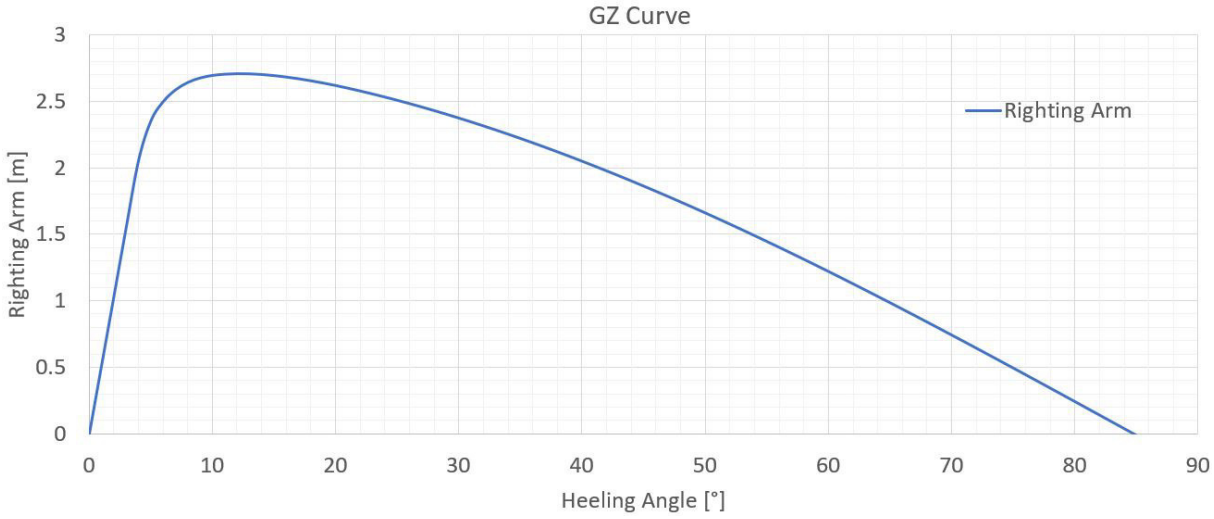

Figure 12.1: The GZ curve calculated by HydroD. The righting arm is evaluated against the heeling angle of the structure

The subsequent step is to compare the characteristics of the GZ curve against the DNV stability requirements. This is done in table 12.2, showing the required and achieved requirements. The stability is in compliance with the requirements except for the location of the maximum righting arm. The maximum righting arm should be beyond a heeling angle of 25°, which is not the case for this structure. The structure's ability to shift its center of buoyancy once certain heeling angle is surpassed is limited, leading to the high initial stability but resulting in the maximum righting arm to be prior to the required 25°. The structure's initial stability is however overall exceeding the class requirements and henceforth taken as sufficient.

Table 12.2: The characteristics from the GZ curve in figure 12.1 compared against the IMO intact stability requirements taken from DNV (2011)

	Required	Achieved	Unit
Area 30°	0.055	1.261	$[mrad]$
Area 40°	0.9	1.379	$[mrad]$
Area $30° - 40°$	0.03	0.118	$[mrad]$
GZ 30°	0.2	2.372	$[m]$
Location GZ_{max}	25	12	[°]
GM_0	0.15	29.69	$[m]$

The structure is furthermore evaluated by analyzing the wind heeling moment in the design- and survival condition defined in section 8.2. The wind is applied to the structure along with the wind-properties defined in section 11.1. The resulting heeling moment is compared against the structure's righting moment and presented in figure 12.2. Both heeling moment curves, are multiplied by a factor of 100 to better follow the trend of both graphs. The initial heeling moment is small when floating upright but increasing dramatically as the windward side lifts clear of the water. The wind heeling moment is hence not critical for the structure's stability, given the large difference between heeling- and righting moment. More critical is the heeling angle at which the main deck touches the waterline, which is at 22°, corresponding to an additional payload of 3 t on one side of the structure. This load is high but not unimaginable given that the structure acts as a working platform too and must hence be remembered during operations.

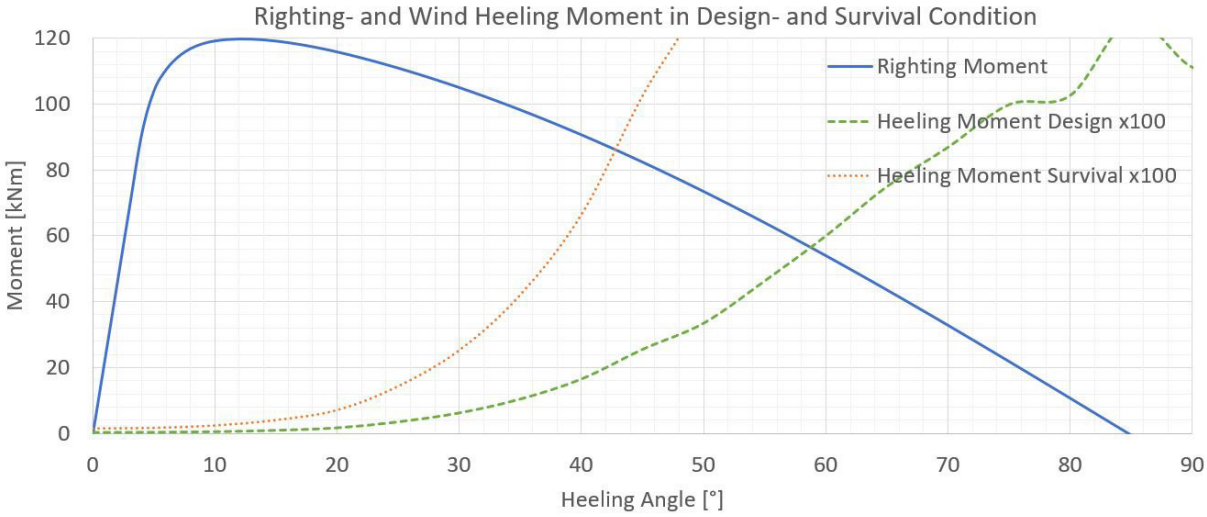

Figure 12.2: The righting moment (blue) is compared against the wind heeling moment in design- (green) and survival condition (orange). The later two are multiplied by 100 to follow their trend

13 Resulting Linear Wave Body Interaction

The linear WBI is calculated using potential theory and the panel model in HydroD, as described in section 11. Linear WBI describes a structure's response to wave frequency loads that are relatively easy and quick to calculate, allowing for an early initial estimation of the seaworthiness of a structure, since wave frequency loads are the dominating load fraction for most structures (Faltinsen, 1993). The RAOs as well as the added mass for heave, roll and pitch are extracted. Furthermore are the potential damping coefficients B_{ij} and the restoring coefficients C_{ij} extracted for the three DOF in question. The later of the two are used to estimate the natural periods T_n for heave, roll and pitch, which is necessary for the evaluation of the structure interacting with a specific seastate.

13.1 Response Amplitude Operators in Heave, Roll and Pitch

HydroD is used to calculate the RAOs in heave (RAO_{33}), roll (RAO_{44}) and pitch (RAO_{55}) for waves coming from all 360° directions, in 15° steps. Only heave, roll and pitch are considered, as these motions are dominated by the hydrostatic restoring, not the restoring supplied by the mooring system. The data is exported by Postresp and implemented in Excel for post-processing. Figure 13.1 shows the RAOs for heave (blue), roll (green) and pitch (orange) with waves coming from 0°, the negative x-direction.

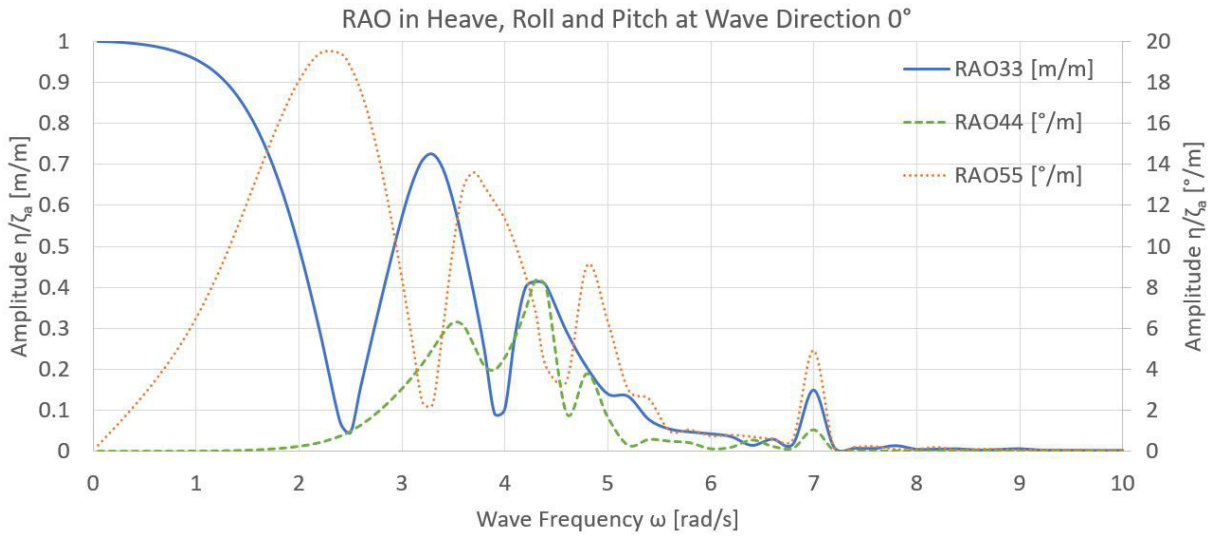

Figure 13.1: The RAOs for heave (blue), roll (green) and pitch (orange) are presented for a wave coming from the negative x-direction

The graph indicates that the response of the structure in the design condition is governed by a heave motion of the structure. The peak of RAO_{33} is at a wave-frequency of $\omega = 3.3\ \frac{rad}{s}$, in the vicinity of the design wave with a wave-frequency of $\omega_{Des} = 3.69\ \frac{rad}{s}$. The heave amplitude in the design operation condition is governed by wave radiation damping and viscous damping (not evaluated), the later being considered small, the former however large due to the large waterplane area. The survival condition on the other hand is governed by a pitch-motion (or roll-motion, depending on the orientation of the structure towards the dominant seastate, since RAO_{55} at 0° is equal to RAO_{44} at 90°). The largest response in pitch, 19.4° pitch rotation per

meter wave elevation, is found at a wave frequency of $\omega = 2.4\ \frac{rad}{s}$. This is right in the realm of the frequency band carrying the most energy in the survival seastate as the JONSWAP spectrum depicted in figure 8.5 in section 8.2 shows. This pitch amplitude is however low enough for the platform deck not to touch the still-waterline.

Further is the response in heave smaller than the wave elevation ζ_a, resulting in generally small wave-frequency motion amplitudes of the structure. This phenomenon is better understood when observing the second noteworthy phenomenon, the disorderly appearance of the RAOs. The trend of all three DOFs is not homogeneous but characterized by peaks and troughs, keeping dominant peaks from establishing. This is due to the nature of the geometry, more specifically due to the cancellation effects between the individual floaters. This effect is best explained using figure 13.2. The example shows a floating structure on columns that is interacting with an idealized wave. The heave in potential theory will be zero since the vertical excitation on the floaters cancel each other out. This effect is the most distinct if the distance between the geometrical center of the waterlines of each floater is half the wavelength $\frac{\lambda}{2}$, ergo if one floater stands in the trough of the wave and the other on the crest.

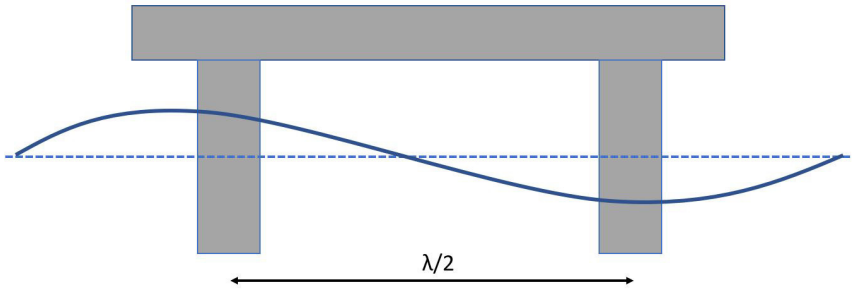

Figure 13.2: Heave motion is canceled as the heave excitation on one column is equal but opposite to the heave excitation on the column on the other end of the structure. This phenomenon is experienced if the floaters waterline center are $\frac{\lambda}{2}$, or a multiple of this, apart

Heave cancellation is also experienced by the floating farm when looking at RAO_{33} in figure 13.1. Focusing on the fist noteworthy trough at $\omega = 2.5\ \frac{rad}{s}$: the wave correlates to a wavelength of $\lambda = 9.86\ m$, meaning that trough and crest of this wave are 4.93 m apart, which corresponds closely to the distance the geometric center of the floaters on one side are apart from the geometric center of the floaters across the growing area, on the opposite side of the structure. A prove is the peak of RAO_{55} at that same frequency. The excitation in heave at this frequency is small, the excitation in pitch however large. This is easily understood when looking again at figure 13.2. The wave will cause the structure to pitch as one end of the structure is forced upwards and the opposite end downwards, resulting in a strong pitching moment. The cancellation- and excitation frequencies of heave and pitch are however not exactly matching up due to the rotationally symmetric geometry of the structure. Looking at figure 6.4 in section 6.2, it becomes obvious that the distribution of the floaters is not exactly symmetric over the x- and y-axis but rotationally symmetric causing the small roll-excitation observed in figure 13.1.

The cancellation behavior of the structure in heave is again observed at a wave-frequency of $\omega = 3.9\ \frac{rad}{s}$. The phenomenon is identical to the one described above with the difference that two subsequent waves cause the cancellation as the one end of the structure is interacting with the crest of wave a and the opposite end with the trough of wave b. However, the smaller λ

becomes, the more complex the response. The wavelength decreases to a point where the interaction between the wave and geometrical details on the floater arrangement, such as the gaps between the floaters, grow increasingly important.

The characteristics of the three RAOs differs for waves approaching the structure with a 45°-heading. Most noticeably is the excitation of all RAOs but RAO_{44} lower compared to a 0°-heading. Figure 13.3 exemplifies this behavior for RAO_{33}, RAO_{44} and RAO_{55} for waves with a 45°-heading. The amplitudes of the peaks for heave and pitch are lower, while the amplitude of the roll-motion grew, compared to a 0°-heading, as RAO_{44} follows the pitch-motion for long waves (low wave frequencies). The first trough of the heave excitation, the first heave-cancellation, is at a slightly larger wave-frequency compared to the case discussed earlier, which nevertheless happens for a similar reason as for the 0°-heading described above. The question remains, why the wave causing the cancellation at a 45°-heading is shorter compared to the wave causing the cancellation in a 0°-heading, given that the structure's diagonal dimension is larger (see section 6.2, figure 6.4) than the dimension in x a wave with a 0°-heading faces?

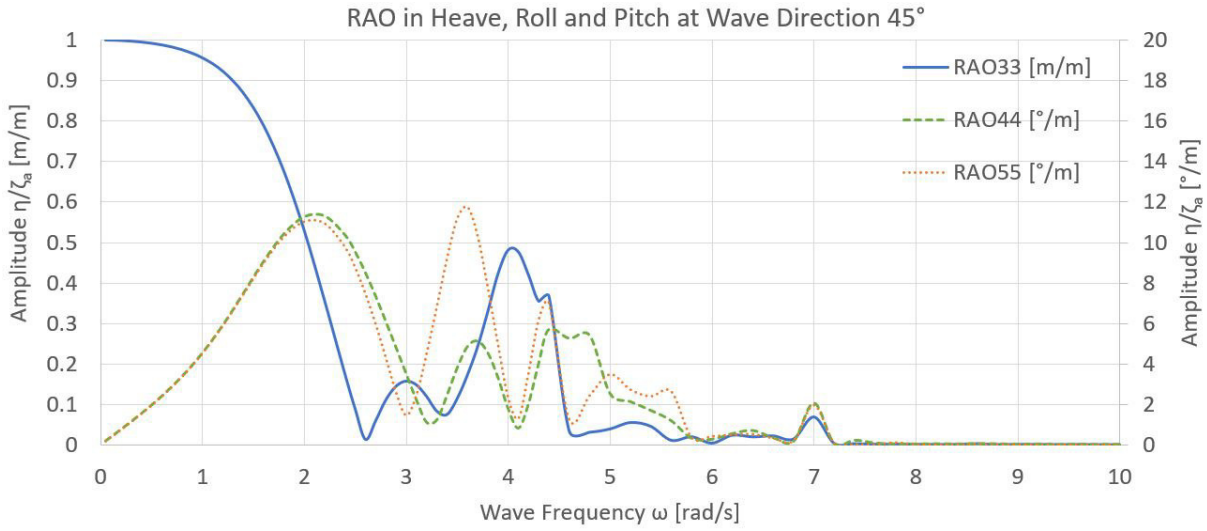

Figure 13.3: The RAOs for heave (blue), roll (green) and pitch (orange) are presented for a wave coming with a 45°-heading onto the structure

The heave cancellation at a wave frequency of $\omega = 2.6\ \frac{rad}{s}$ can be explained with the example presented in figure 13.4. The figure shows a platform supported by a floater interacting with a wave, with λ being within the vicinity of the length of the floater. The floater in this scenario is interacting with the wave trough and half of two wave crests within one wavelength. The upward excitation of the two half wave crests is hence counteracted by the wave trough at the center of the floater, resulting in a cancellation of the heave excitation.

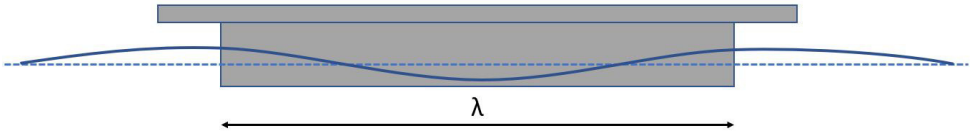

Figure 13.4: The heave excitation of the two wave crests of one wave cancel with the wave trough of that same wave if the structure's floater length matches with the wavelength λ or a multiple of it

This behavior is analogous for the structure evaluated in this thesis as the side view of the structure depicting a view along the diagonal in figure C.1 appendix C shows. The wave frequency of $\omega = 2.6\ \frac{rad}{s}$ corresponds to a wavelength of $\lambda = 9.12\ m$, which closely relates to the diagonal distance of the structure's floater arrangement, leading to the heave cancellation. The quasi continuous floater arrangement along the diagonal causes a strong pitch- and roll motion at a wave frequency of $\omega = 2.2\ \frac{rad}{s}$. This is due to the heave motion at this frequency causing a rotational motion around the axis orthogonal to the wave-heading, as the wave-ward corner of the structure is lifted while the opposite corner interacts with a wave trough. The rotational motion caused by this can be decomposed into a pitch- and a roll motion to equal parts, as the close proximity of both graphs in figure 13.3 shows. This climax of roll and pitch marks furthermore the point where the rotational symmetry of the structure starts to have a noticeable effect. Roll and pitch start to diverge considerably, as the interaction between small wavelengths with the complex floater arrangement becomes increasingly manifold.

The last noteworthy characteristic, that all RAOs analyzed have in common, is a small peak at a wave frequency of $\omega = 7\ \frac{rad}{s}$. The peak is not large for non of the considered motions, what is however interesting is the circumstance that the peak exists for every motion at the exact same frequency. The excitation as been almost zero for all three motions, heave, roll and pitch for waves of slightly smaller frequency and drop right back down as soon as $\omega = 7\ \frac{rad}{s}$ is passed. The solution is found when setting the wavelength of this specific frequency ($\lambda = 1.26\ m$) in relation with the dimensions of one floater ($1.2\ m\ x\ 2.0\ m$). The reason for this is hence related to the heave-cancellation example shown in figure 13.4. The graphic exemplifies how the excitation in heave is canceled if $\lambda = l_{floater}$, ergo if the wavelength λ is equal to the floater length in the wave-propagation direction $l_{floater}$, since the excitation of two half wave crests equals out with the one wave trough. This further implies, that the strongest excitation in heave the body can experience is if $1.5\lambda = l_{floater}$, thus if two full wave crests and one wave trough act upon the floater. Consequently is a rotational motion around the diagonal axis triggered if one floater on one corner of the structure is excited, which is again decomposed into a roll- and a pitch motion, analog to the case with waves coming from a 45°-heading discussed above.

This behavior is confirmed when looking at figure 13.5. The figure shows the Wadam offbody points described in section 11 at a wave frequency of $\omega = 7\ \frac{rad}{s}$ and a heading of 0°. The longitudinal floater, in terms of the wave direction, at the bottom right corner is interacting with 1.5λ, while the transverse floaters above it are only interacting with one wave length (remembering that the offbody points do not exactly touch the floaters, letting the floaters appear bigger then in reality). The heave-excitation on the transverse floaters is hence zero, while the heave excitation on the longitudinal floater on the bottom right corner is maximal, causing the whole structure to rotate around the diagonal axis. The result is the excitation of heave, roll and pitch, since the a wave frequency of $\omega = 7\ \frac{rad}{s}$ causes heave cancellation on transverse floaters and heave excitation on longitudinal floaters, triggering a rocking motion of the structure as all three motions are engaged simultaneously. The overall excitation of the structure is however small as the RAOs suggest, since only half of the eight floaters experiences heave excitation.

The correctness of the calculations in HydroD can partly be evaluated by looking at the RAOs in roll and pitch. The square geometry of the structure allows this conclusion, since waves coming from a 0°-, a 90°- or a 180°-heading are interacting with the same floater arrangement, as the panel model in figure 11.3 shows. The only difference is the arrangement of the walkways, which causes the moment of inertia around the x-axis to diverge with 0.98% from the moment

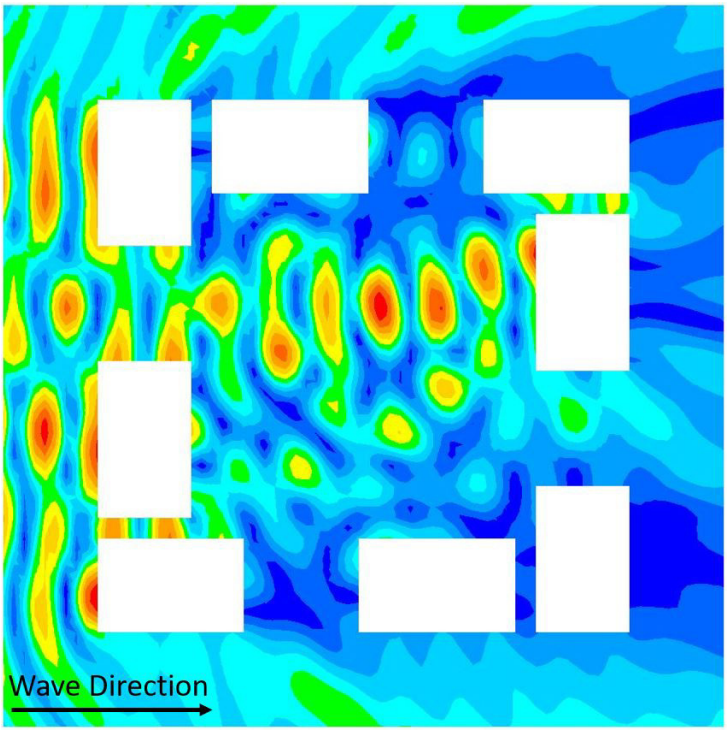

Figure 13.5: Explanation of the rocking motion of the structure

of inertia around the y-axis. The influence this discrepancy has on the linear WBI of a 0°- and a 90°-heading is negligibly small as is shown in the following. The impact the rotational symmetric geometry has on the RAOs of roll and pitch is shown in figure 13.6. Both graphs, the green one for RAO_{44} for waves coming from a 90°-heading and the the blue graph depicting RAO_{55} for waves coming from 0°-heading, are essentially indistinguishable, as should be the case given the square geometry. Furthermore proves the small divergence in moment of inertia not to have a noticeable effect on the RAOs.

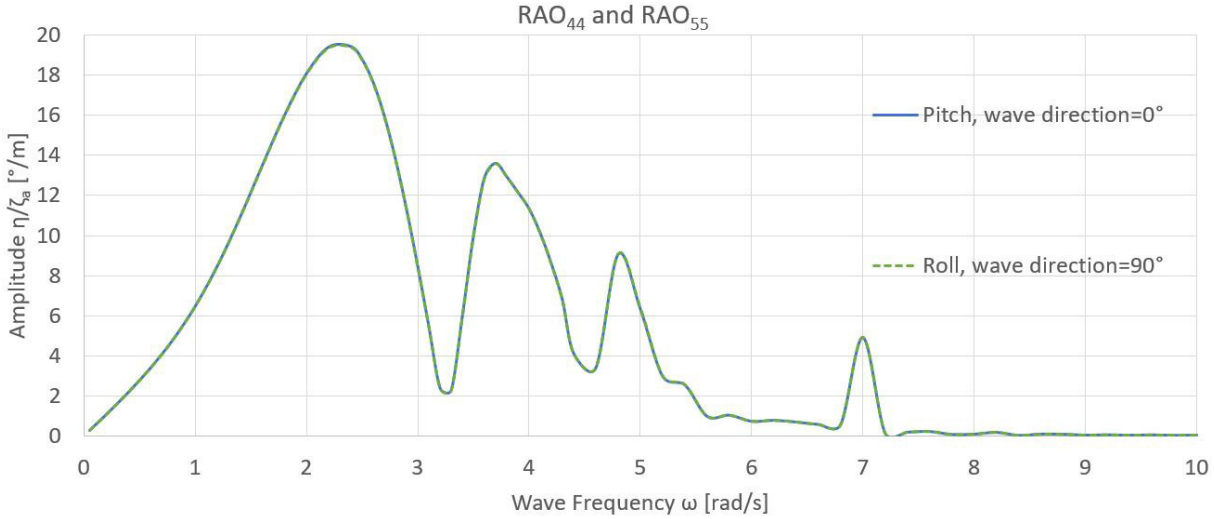

Figure 13.6: The RAO in pitch and roll are compared. RAO_{44} (green) is interacting with a wave coming from 90° and RAO_{55} (blue) with a wave from 0°. Both graphs are identical

Further analyzing RAO_{33}, RAO_{44} and RAO_{55} for an increased number of headings confirms this assumption, as figures C.2, C.3 and C.4, depicting the interaction between waves from multiple headings and the square geometry, show. The RAO in heave is only distinguishable for waves coming in on the side of the structure and waves coming onto the diagonal, while the RAOs in roll and pitch differentiate between waves coming from a 0°-, a 90°- , a 45°- and 135°-heading. Waves coming from directly opposite directions, e.g. 0° and 180°, however trigger the same response. Ergo is an analysis of a range of waves coming from 0° and 180° sufficient for the calculation of the linear RAOs in heave, roll and pitch. However, proving the symmetric behavior of the RAOs does not confirm that the excitation amplitudes of the RAOs presented is correct. It nevertheless proves that the approach chosen to calculate these RAOs is the correct one since the presented behavior is as expected.

13.2 Hydrodynamic Coefficients

The hydrodynamic coefficients added mass A_{ij}, potential damping B_{ij} and the restoring coefficients C_{ij} are resulting from the EOM in all six DOF of a floating body, allowing for a total of 36 added mass- and damping coefficients, from which many are zero due to the symmetry of the body. The first two, added mass and damping, are steady state hydrodynamic forces due to forced harmonic motion of the pressure field of the fluid (Faltinsen, 1993) that result from the multiplication with an acceleration, in the case of added mass, and velocity for the damping coefficients. The restoring coefficients, important for the fixing of the natural periods (Greco, 2018), describe a load resulting from the rigid body deflections from its neutral floating position and the subsequent change in buoyancy.

When performing a linear WBI are the hydrodynamic coefficients important mainly for the estimations of natural frequencies in the DOF that engage a restoring force. Natural frequencies are important as they show which wave frequencies are to be avoided. Should the exciting frequency be in the realm of the natural frequency of the structure can the motion amplitudes of the structure be substantial, given small damping. The natural frequency is calculated using equation 13.1 as the square root of the resorting coefficient C_{ij} divided by the mass M_{ij} plus added mass A_{ij}.

$$F_n = \left(\frac{C_{ij}}{M_{ij} + A_{ij}} \right)^{\frac{1}{2}} \tag{13.1}$$

The added mass however is highly frequency dependent, making the identification of the natural frequency not straight forward. Figure 13.7 shows this behavior. The graph compares the added mass in heave $A33$, roll $A44$ and pitch $A55$ as they develop over the oscillation frequency range.

The most accurate way to estimate the natural frequency of a floating structure is to do a full-scale motion decay test, where the structure is moved from its equilibrium position and released. The resulting movement of the structure oscillates with its natural frequency. The estimation of the natural frequency from linear WBI on the other hand is not as apparent due to the frequency dependent added mass, which raises the question which added mass to use for the calculation. The other parameters, M_{ij} and C_{ij} are constant throughout the frequency range. Table 13.1 lists these hydrodynamic coefficients.

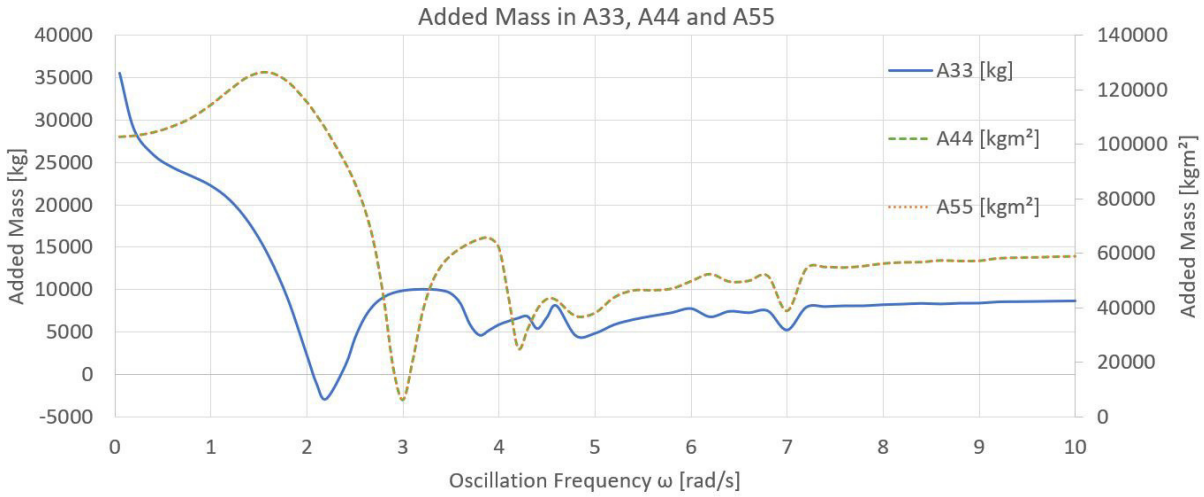

Figure 13.7: The added mass in in heave A33, roll A44 and pitch A55 are compared with one another

Table 13.1: The linear hydrodynamic coefficients C_{ij} and M_{ij}

Vector	ij	C_{ij}	M_{ij}
Heave Heave	33	190200 $\frac{kg}{s^2}$	4514 kg
Roll Roll	44	13144000 $\frac{kgm^2}{s^2}$	28100 kgm^2
Pitch Pitch	55	13144000 $\frac{kgm^2}{s^2}$	28300 kgm^2

The natural frequency calculated with equation 13.1 is hence only dependent on added mass as A_{ij} is a function of frequency. This is easily understood when looking at figure 13.8. The with itself non-dimensional added mass in heave $A33$ is plotted against the with itself non-dimensional natural frequency in heave $Fn33$ calculated using equation 13.1. The plot shows how the natural frequency behaves disproportional to the added mass. It also shows that the added mass has become negative at an oscillation frequency of 2.2 $\frac{rad}{s}$. This phenomenon is unusual but not unheard of, as Faltinsen (1993) points out, especially when analyzing structures with multiple floaters, e.g. catamarans.

What is of interest when analyzing figure 13.8 is the intersection between the estimated natural frequency and the dotted orange diagonal. This curve represents the input frequency being equal to the resulting natural frequency. The natural frequency of a body in linear theory can be found at the point where the estimated natural frequency intersects the excitation frequency. A detailed look at the natural frequency curve in figure 13.8 shows that this is the case at three instances, as there are three interceptions between $Fn33$ and the diagonal. The motion of the platform can hence be excited at three instances, the first at $\omega = 3.4$ $\frac{rad}{s}$, the second at $\omega = 3.6$ $\frac{rad}{s}$ and the third at $\omega = 4.0$ $\frac{rad}{s}$, depending on the phase shift between excitation- and response frequency.

However does this not mean that the structure at resonance is necessarily experiencing very large motion amplitudes resulting in a resonance catastrophe. Damping plays an important role when analyzing a structure's motion, as it reduces motion amplitudes. Yet, linear theory is only regarding potential damping, omitting viscous damping such as friction damping and eddy-making damping, making the complexity of damping obvious. This is complicated further

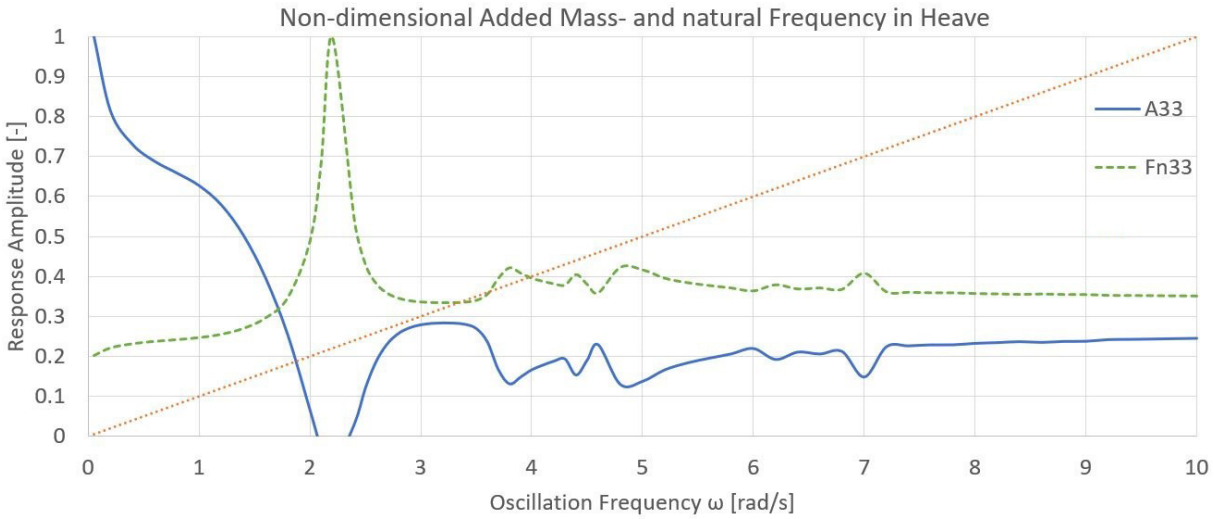

Figure 13.8: The non-dimensional added mass in heave $A33$ is plotted alongside the non-dimensional natural frequency in heave $Fn33$. The dotted orange diagonal represents the curve where input frequency and resulting frequency are equal

by the complexity of the floater arrangement. The dotted green graph representing the non-dimensional radiation damping in heave in figure 13.9 exemplifies this. The figure indicates a strongly varying damping, which is especially complex in the oscillation frequency band from 3.8 $\frac{rad}{s}$ to 4.8 $\frac{rad}{s}$ and comparably large given that the maximum damping has a maximum amplitude of 34.7 $\frac{kNs}{m}$ at 2 $\frac{rad}{s}$. The RAO in heave mirrors this complex behavior. The figure further indicates that the three frequencies identified above as being able to cause resonance have no evident effect on the RAO in heave. The complexity of the damping as well as the floater arrangement seam to prevent the constitution of a noticeable peak in $RAO33$. Cancellation effects as described in section 13.1 seam to have a much greater impact on the motion amplitudes of the structure.

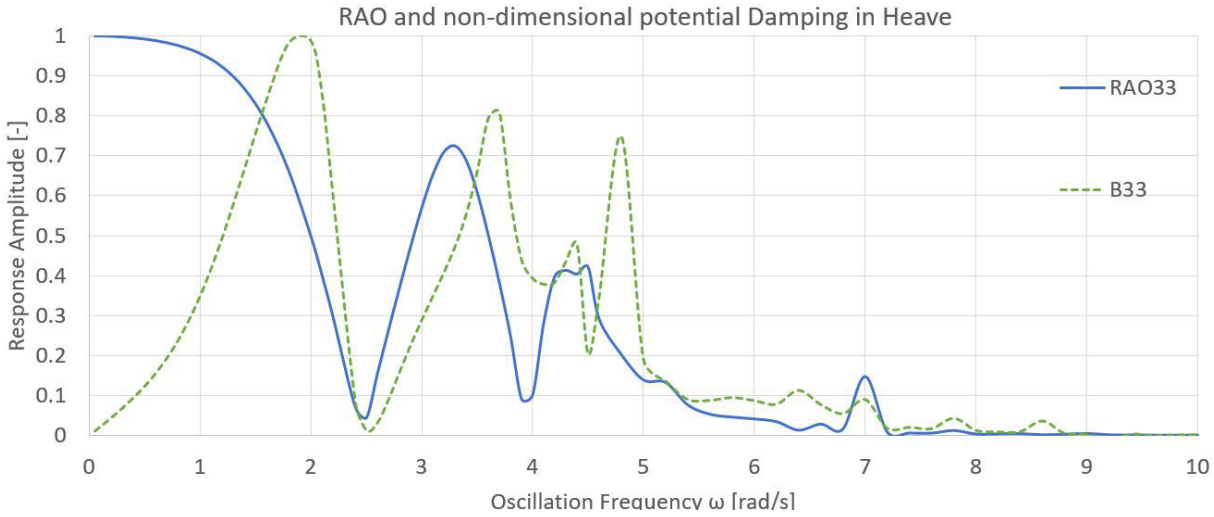

Figure 13.9: The RAO in heave $RAO33$ is plotted alongside the non-dimensional radiation damping in heave $B33$

The complex added mass and damping behavior over the oscillation frequency range makes the prediction of natural frequencies vague. Hence must another indicator be used to measure how well suited the structure is for a given seastate. The RAOs in combination with the seaspectra expected for the OS $S_\zeta(\omega)$ could fulfill this purpose, as the resulting response spectra $S_R(\omega)$ allows for this validation. The negligence of the natural frequencies does however not apply for the time-series evaluation of the structure interacting with a mooring system, as this introduces restoring forces in surge, sway and yaw as well as it changes the restoring- and damping coefficients for heave, roll and pitch.

13.3 Linear Motion Response

The response spectrum in a specific DOF pictures the energy of the motion in this DOF that is transferred from the surrounding seastate to the floating body. Figure 9.5 already showed how a response spectrum $S_R(\omega)$ is product of the RAO in the respective DOF and the defined wave spectrum $S_\zeta(\omega)$ following equation 13.2.

$$S_R(\omega) = H^2(\omega) * S_\zeta(\omega) \tag{13.2}$$

The response of the floating body is analyzed in the relevant DOFs heave, roll and pitch. The response $S_R(\omega)$ is found for the design- and survival condition with waves coming from all directions onto the body. Figure 13.11 depicts the heave response for the floating body interacting with 0°-heading in both design and survival condition. Comparing the survival heave response spectrum with the survival wave spectrum in figure 8.5 shows that only a part of the energy contained in the seastates is transferred to the floating body, since the peak of the wave spectrum and the response spectrum are not aligned but lay 0.5 $\frac{rad}{s}$ apart, as figure 13.10 shows.

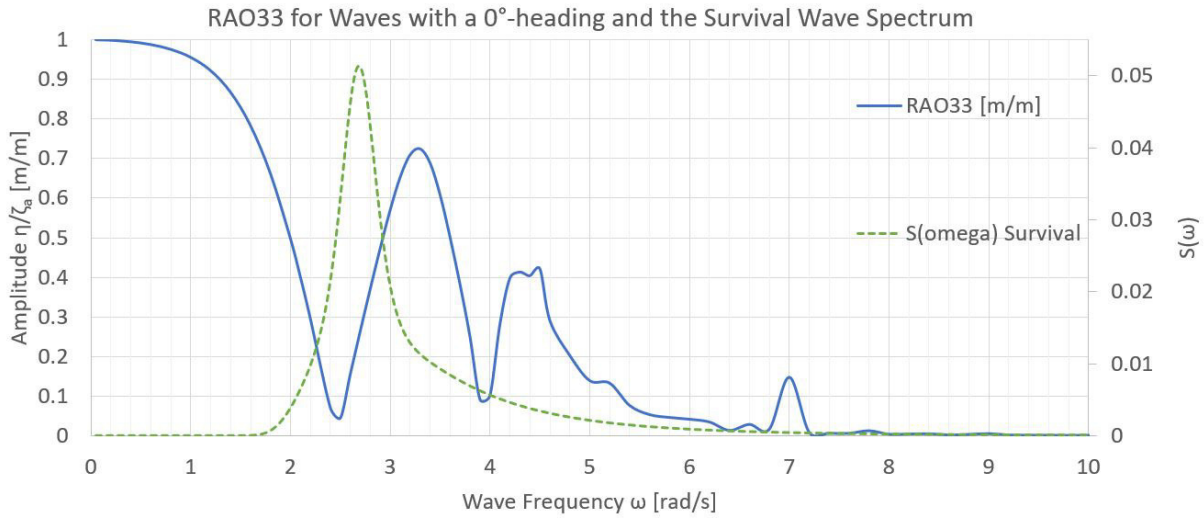

Figure 13.10: The RAO in heave is interacting with the survival seastate coming at a 0°-heading. Only part of the energy contained in the seastate is transferred to the body as the peak of $S_\zeta(\omega)$ does not align with RAO33

This behavior differs for the design response as the peak of the design wave spectrum aligns well with the design response spectrum, causing the design- and survival response spectrum to not vary strongly from each other, given that the energy carried in both seastates varies greatly

from each other. This heave response in the design seastate is further amplified by the peak of the RAO in heave at around 3.4 $\frac{rad}{s}$. $S_R(\omega)$ in heave for the design- and survival condition shown in figure 13.11 depicts the mechanisms described above.

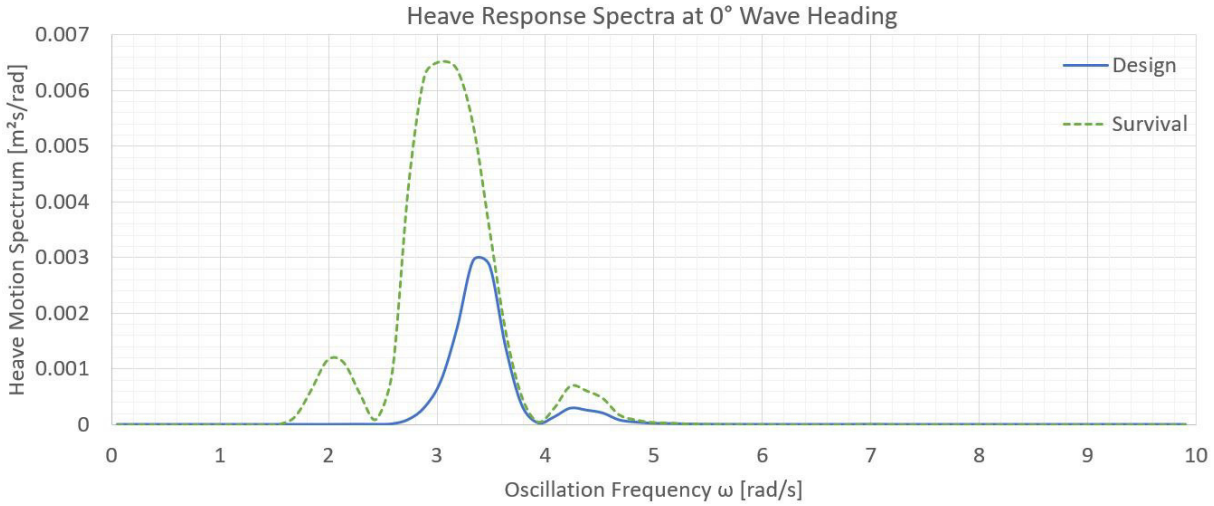

Figure 13.11: The linear un-moored heave response of the floating structure to the design- and survival seastate presented in section 8.2

The response differs depending on the heading the waves are coming with onto the structure. It is henceforth important to also observe $S_R(\omega)$ for waves coming from different directions. Figure 13.12 depicts the heave response spectrum in the survival condition for waves coming from a 0°-, a 45°- and a 90°-heading. The change in heading has a strong effect on the heave response spectrum since the floater arrangement the incoming wave interacts with differs depending on the heading, changing the ratio between incoming wavelength and floater dimension in the wave propagation direction. The peak at $\omega = 3.0\frac{rad}{s}$ vanishes almost completely, while the secondary peaks close to the right and left of the primary peak increase slightly. This low amplification can be explained with the RAO in heave for waves coming with a 45°-heading depicted in figure C.2 in appendix C. This RAO only marginally interacts with the frequency band the survival seastate in figure 8.5 carries most of its energy in. A further result extracted from figure 13.12 is that the response for waves coming with a 0°- and a 90°-heading are identical, again emphasizing the rectangular shape of the structure.

The response is also analyzed for roll- and pitch motion. The RAO in pitch depicted in figure 13.1 already showed that pitch motion dominates the rotational motions. This can be confirmed when observing figure 13.13 depicting the roll- and pitch motion in both design and survival condition. The pitch response at survival condition is 40 times larger then the roll response at survival condition. Furthermore is the amplitude difference of the pitch motion between the design- and survival seastate much greater as is the case for the roll motion. Looking at RAO_{55} yields the answer: the peak of the survival wave spectrum is right in the vicinity of the first peak of RAO_{55} while the design wave spectrum peaks right at the first trough of RAO_{55}. This behavior can not be observed for the roll-motion response, as there is barely any area beneath RAO_{44} where the survival wave spectra peaks. Ergo is the amplitude difference for the roll response when comparing design- and survival condition small.

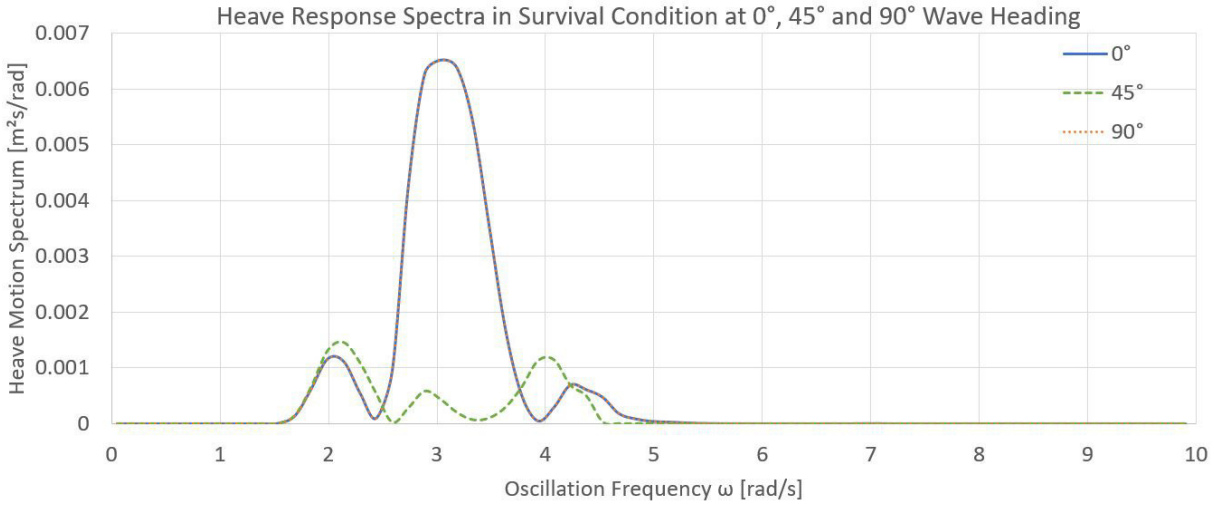

Figure 13.12: The heave response in the survival condition is compared for waves with a 0°-, a 45°- and a 90°-heading. The dominant peak of the heave response to waves with a 0°-heading vanishes almost completely as the RAO for waves coming with a 45°-heading is moved from the frequency band the survival seastate carries most of its energy in

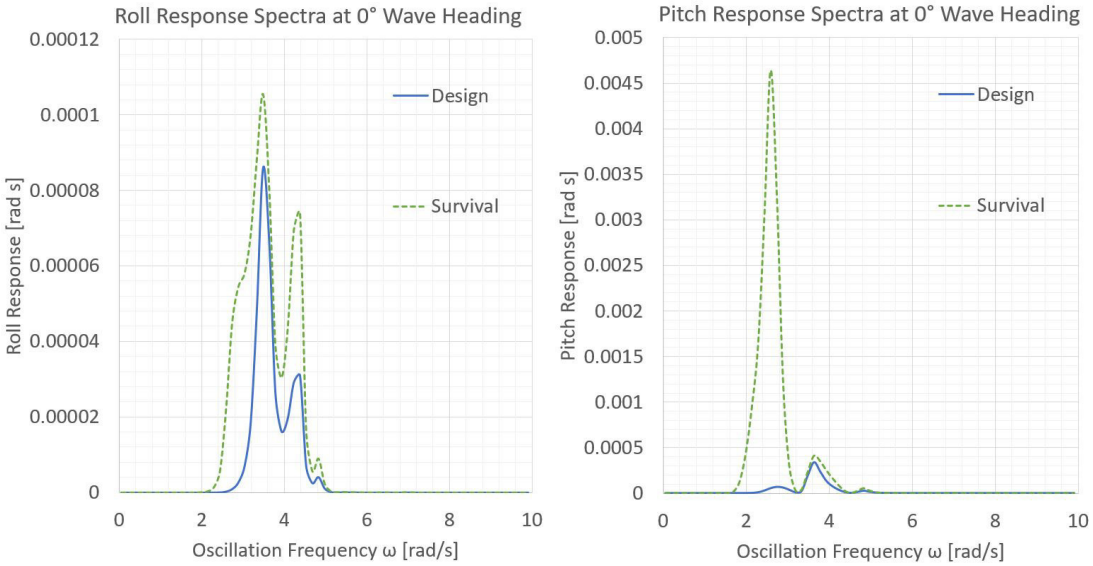

Figure 13.13: The roll- and pitch motion response interacting with the design- and survival seastate. The fundamentally different behavior of the roll- and pitch motion is due to the peculiar shape of RAO_{55}, causing a large response in the survival seastate and a small response in the design seastate

The motion response in the design case is dominated by comparably small heave motions which are complemented by small roll- and pitch motions. The survival response contains a similar ambiguity: The heave motion is not strongly amplified, the pitch motion on the other hand is noteworthy. Overall is the linear motion response of the un-moored structure low, referring to the design roll- and pitch motion or the survival heave motion, as the paring of wave spectrum and transfer spectrum results in overall low motion amplifications.

14 Resulting Nonlinear Body Motions and Mooring Response

The response of a moored body interacting with a random sea is a highly non-linear one as seastate, body motions, mooring motions and tensions affect one other. Section 11.3 already emphasized that a time-domain analysis is required in the case of a highly frequency dependent added mass, which is the case following section 13.2, and if dynamic loads and the investigation of natural periods is important. The knowledge of dynamic loads is vital for the conformation of the integrity of the mooring system. Furthermore are the natural periods of the moored structure, for which linear potential theory can not present satisfactory results, fundamental for the estimation of the structure's motion characteristic and henceforth the operability of the structure.

14.1 Natural Frequencies of the Moored Structure

The station keeping of the mooring system has an elementary influence on the motion characteristics of the floating body, especially the translatory motions surge and sway. The mooring system introduces additional restoring coefficients into the system, causing oscillatory motions where there where previously none, as is the case for the translatory motions η_1, η_2 and the rotatory motion η_6 around the z-axis. These restoring coefficients are however of a different nature as the restoring coefficients which where mentioned earlier, e.g. section 13.2, as they are not due to a change in displaced volume but due to multiple changes in the mooring line arrangement. For one is the displacement of the mooring line changing if the floating body is e.g. forced sideways from its natural position. This engages the mooring line and in this case causes the CW to lift, which introduces a restoring force into the system opposing the external force. This mechanism is presented in figure 14.1 with the gray model showing the system in its equilibrium and the blue model showing the system as it is forced from its natural position.

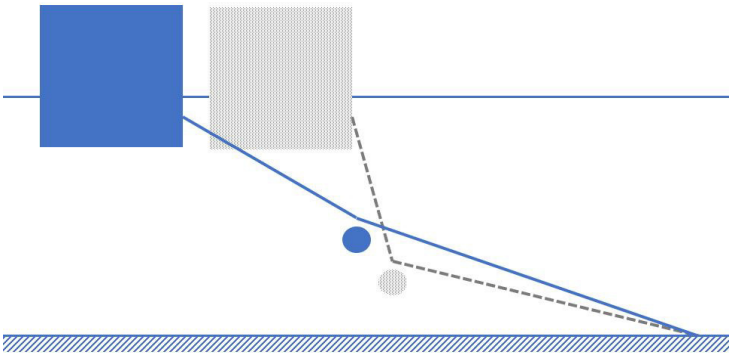

Figure 14.1: One factor contributing to the restoring forces introduced to the system is the displacement of the mooring line arrangement, in this case the straightening of the mooring line and the lifting of the CW. The gray model represents the system in equilibrium and the blue model when it is forced from its natural position

The second noteworthy contributor to the restoring supplied by the mooring system is the elasticity of the mooring line. Especially in deep- and ultra deep taut line mooring arrangements is the elasticity of the synthetic rope providing almost all the restoring force, since the elastic elongation of synthetic mooring line used in ultra deep mooring arrangements is substantial. This is the difference to a chain link mooring line, as the elongation of steel chain is a fraction of that of synthetic rope, ergo is the restoring force from catenary chain link mooring arrangements

dominated by the displacement of the line in the watercolumn. The mooring arrangement as presented in this study is counter intuitively governed by the displacement of the mooring line, regardless of the mooring line consisting largely of synthetic rope. This is due to the comparably short length of the mooring line and the mooring arrangement itself. The restoring of the CW-mooring arrangement relies on the CW changing its position in the watercolumn to generate the restoring force necessary.

The mooring systems does however not only introduce a restoring force but also a damping force. Damping describes the dissipation of energy from the system, which uses different mechanisms to do so. Usually is the damping supplied by a mooring system dominated by the interaction between the mooring line and the surrounding body of water, thus friction and eddy-making damping. The damping coming from the mooring system is in this case however small since damping from mooring arangements similar to the one discussed here can be considered minimal following Gao and Moan (2009). Furthermore is non-linear damping, friction- and eddy-making damping on the structure not accounted for. The reason is that the structure is first of all operating within a diffraction-dominated environment, as figure 9.2 shows, and second of all is the negligence off viscous damping leading to more conservative results concerning the motion amplitudes of the body and hence the loads on the mooring arrangement.

The mooring system introduces a restoring force allowing an oscillatory motion. Any oscillatory motion can be excited and cause resonance which can impair operations and in the worst case lead to substantial damage to the installation, if an external excitation oscillates with a similar frequency as the natural frequency of the structure. The knowledge of the characteristics of the natural frequencies is hence crucial. In terms of heave oscillations are especially first order wave loads important while second order loads can be of significance when analyzing surge and sway motions and must hence be accounted for when the later motions are critical for the structure's operation. This emphasizes an important point when analyzing the motions of moored structures: certain motions are of a greater importance than others, depending on the purpose of the structure. In the case of the support structure for hydrophylic crop analyzed in this report is the surge and sway motion of greater importance then e.g. the heave motion, as the cramped water surface at the OS prohibits large horizontal motions of the platform. Furthermore are surge, sway and yaw motions analyzed as they are governed by the restoring forces introduced by the mooring system, not the hydrodynamic restoring. Surge, sway an yaw do not substantially change the whet-surface area and are ergo not engaging hydrodynamic restoring.

The natural frequency of the system is in the case not calculated as is done previously by estimating the added mass A_{ij} as well as the damping coefficients C_{ij} and implementing them into equation 13.1. Section 13.2 already showed the flaws of this method caused by the complexity of the geometry. This complexity is even greater when introducing the mooring arrangement. The estimation of the necessary hydrodynamic coefficient becomes vague, as the restoring coefficient becomes a combination of hydrostatic restoring due to the change in whetted surface area, non-linear mechanical restoring due to the change of mooring line position in the water and elastic restoring due to the elasticity of the synthetic fiber lower part of the mooring line. Ergo is the natural frequency estimated by conducting a numerical motion decay test in SIMO.

The numerical motion decay test is conducted by releasing the body from an off-balanced floating position. The body is moved from its natural position by defining a force that is switched off after a specific time interval. The static solution will find this static equilibrium from which the

dynamic solution is initiated from. The time interval and therefore the presence of the defined force ends 100 s into the TDS after which the restoring forces within the system (buoyancy forces, line tensions, etc.), that previously counteracted the defined force, initiate an oscillating motion in the DOF the specified force is previously defined in.

The motion decay in heave is realized by forcing the platform downwards with a force equal to a weight of 2.5 t. This causes the structure to be 13 cm deeper submerged. Figure 14.2 shows the system's behavior after being released. The oscillation quickly dies down due to the large radiation damping and adapts a beat interference behavior caused by the mooring lines. To go further into the unusual shape of the decay of the heave motion: the heave oscillation gets passed from the structure onto the mooring arrangement, which in turn starts oscillating, drawing the energy stored in the motion from the structure. This however starts exciting the structure to move again, causing the the beat in interference to establish depicted in figure 14.2. The negligence of viscous damping on the structure further prevents small amplitude oscillations from dying out quickly. The plot does however allow for the estimation of the natural period in heave of the moored system by measuring the time between each zero-upcrossing. The natural frequency in heave Tn_{33} can be measured to be $Tn_{33} = 1.314\ s$ and the natural frequency in heave Fn_{33} to be $Fn_{33} = 4.783\ \frac{rad}{s}$. Comparing this value with the design- and survival wave spectrum in figure 8.5 shows that the natural frequency in heave is well outside the frequency band carrying most of the energy in both seastates.

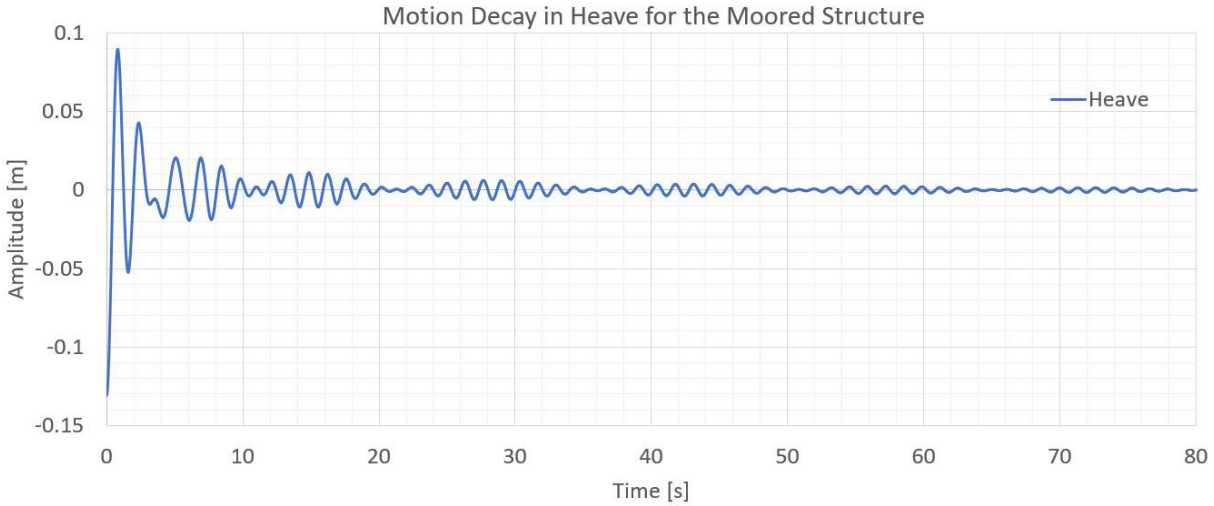

Figure 14.2: The heave motion decays quickly due to the large radiation damping. Small oscillations however are slow to die down due to the absence of viscous damping of the body motions. The natural frequency in heave can be measured as $Fn_{33} = 4.783\ \frac{rad}{s}$

The analysis of the linear potential WBI furthermore showed that pitch motion is critical, especially in the survival condition. Ergo is the motion decay in pitch evaluated as well. The application of a moment of 77.8 kNm forces the structure to pitch 3.4°, subsequently switching of the moment then causes the structure to pitch, resulting in the motion decay pictured in figure 14.3. The resulting natural period is at $Tn_{55} = 1.493\ s$ corresponding to $Fn_{55} = 4.209\ \frac{rad}{s}$, a slightly lower natural frequency compared to the heave motion. However must the inaccurate representation of the inertia be mentioned here resulting from the negligence of the flowerbeds, which, when modeled correctly, would cause the natural frequency to be slightly higher. What

is similar to the heave motion decay too is the behavior of the pitch decay. The oscillation in pitch adapts a beat interference due to the interaction between mooring system and structure, similar to the phenomenon described in the heave motion decay above.

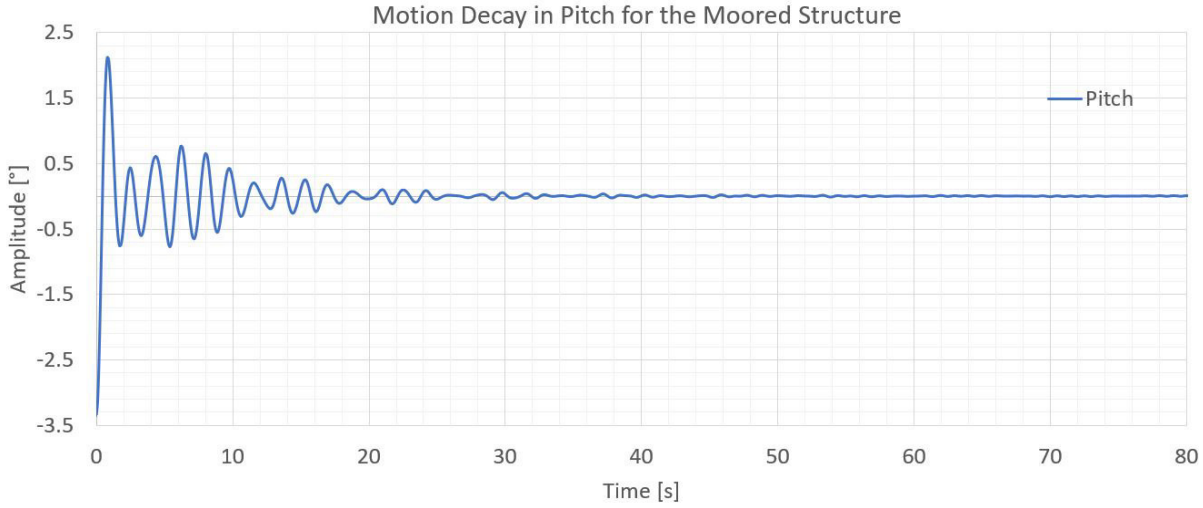

Figure 14.3: The natural period is slightly larger then Tn_{33} at $Tn_{55} = 1.493\ s$

Resonance can also be excited in surge and sway. These motions are usually characterized by large periods and slow decay due to the limited linear wave-radiation damping. The natural period in surge and sway is determined in the same manner as for the heave motion, with the difference that only the restoring force of the mooring system is engaged. A force of 3 kN is applied in the x- and y-direction to estimate the natural frequency for surge- and sway motion, which displaces the structure 1.5 m from its natural position. The structure is then released and starts oscillating with a frequency of $Fn_{11.22} = 0.437\ \frac{rad}{s}$ corresponding to a natural period of $Tn_{11.22} = 14.393\ s$. This is small compared to conventional off-shore structures, which natural periods in surge and sway are in the order of minutes (100 s to 200 s following Faltinsen (1993)).

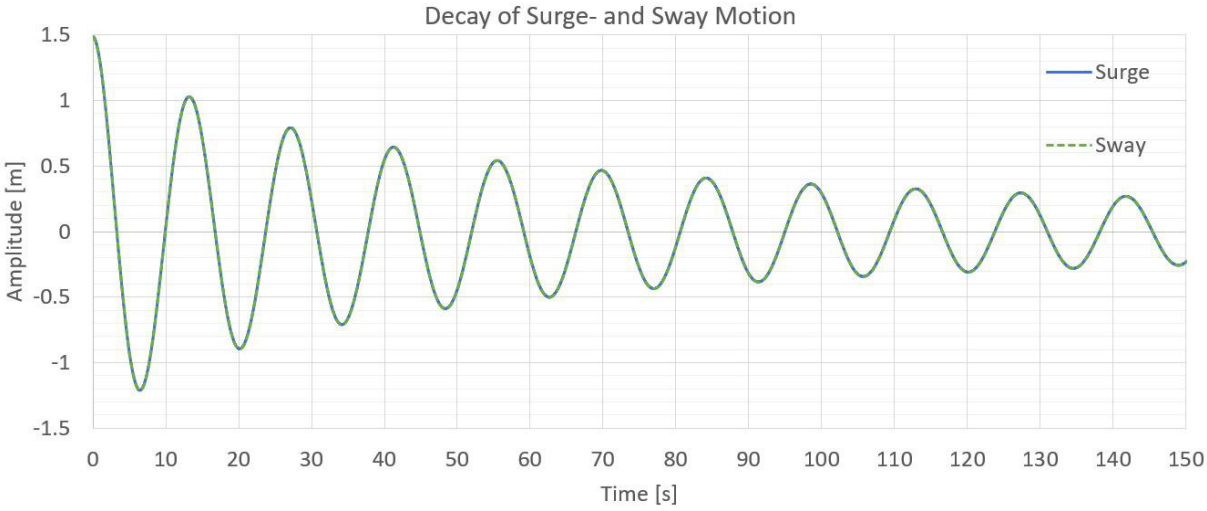

Figure 14.4: Both surge and sway motion are exactly the same due to the geometry of the structure. The low frequency motions give small motions velocities resulting in a low damping

The environment the structure analyzed in this report however puts the relatively small natural period back into perspective. The excitation of surge or sway motions from linear wave loads only is in this area of the Baltic Sea practically impossible due to the sheltered location of the ocean farm. Second-order difference-frequency loads however are able to excite these motions. Section 9.3 already emphasized how difference frequency loads are oscillating with large periods and are hence likely to cause resonant large-amplitude surge and sway motions of the moored structure. If these second order loads are critical or not depends on the magnitude compared to the wave frequency loads. Figure 14.4 depicts the motion decay in surge and sway. Both motions decay slowly compared to the heave motion due to the slow oscillatory motion, resulting in small viscous damping on the mooring lines. Both motions are exactly the same due to the geometry of the structure. It is important to mention that the motion amplitudes and slow decay presented in figure 14.4 represent a conservative estimate due to the negligence of viscous damping on the structure. The results of the numerical motion decay tests are summarized in table 14.1.

Table 14.1: The resulting natural periods and -frequencies from the numerical motion decay test in heave, pitch, surge and sway

	Fn $[\frac{rad}{s}]$	Tn $[s]$
Heave	4.783	1.314
Pitch	4.209	1.493
Surge & Sway	0.437	14.393

14.2 Time Domain Analysis

The time domain analysis in SIMO is carried out to gather information about the motion of the moored structure and the response of the mooring arrangement when interacting with an irregular seastate. The DNV-GL (2015) offshore standard defines three guiding criteria: The ultimate-, the accident- and the fatigue limit state (ULS, ALS & FLS). The ULS allows a first assessment of the mooring arrangement, ergo is the ULS the guiding criterion for the subsequent analysis. The ULS environment is defined by the survival seastate, the worst case current condition and the survival wind condition, the later applied as a steady force as detailed in section 8.2. The parameters set for the simulation are of utmost importance for the reliability of the solution and the convergence of the solution. Vital parameters such as time-step, simulation time, wave time-series length, wave time-series time increment and the accuracy are collected in table 14.2.

Table 14.2: The presented parameters govern the simulation procedure in SIMO-RIFLEX

Simulation length	4000	[s]
Simulation time step	0.01	[s]
Wave time-series length	4000	[s]
Wave time-series time increment	0.1	[s]
Newmark-β; β/γ	0.25/0.5	
Energy Accuracy	1×10^{-5}	[N]
Displacement Accuracy	1×10^{-5}	[m]

14.2.1 Rigid Body Motions

The body is excited to move in all six DOFs with varying amplitudes, depending on the seastate and the DOF in question. The EOM is solved at each time step of the TDS and the results for rigid body motions and mooring line tensions are stored. Figure 14.5 depicts an extract of this TDS, presenting the survival condition wave elevation, the heave motion response alongside the mooring line tension at the fairlead 3 as an example. Figure D.1 in appendix D presents the full TDS without the transient phase ($0s - 400s$) for the wave elevation and heave response in the survival condition. The heave motion amplitude compared to the wave elevation shows what the heave ROA in section 13.1 already suggests: the overall heave amplification is small.

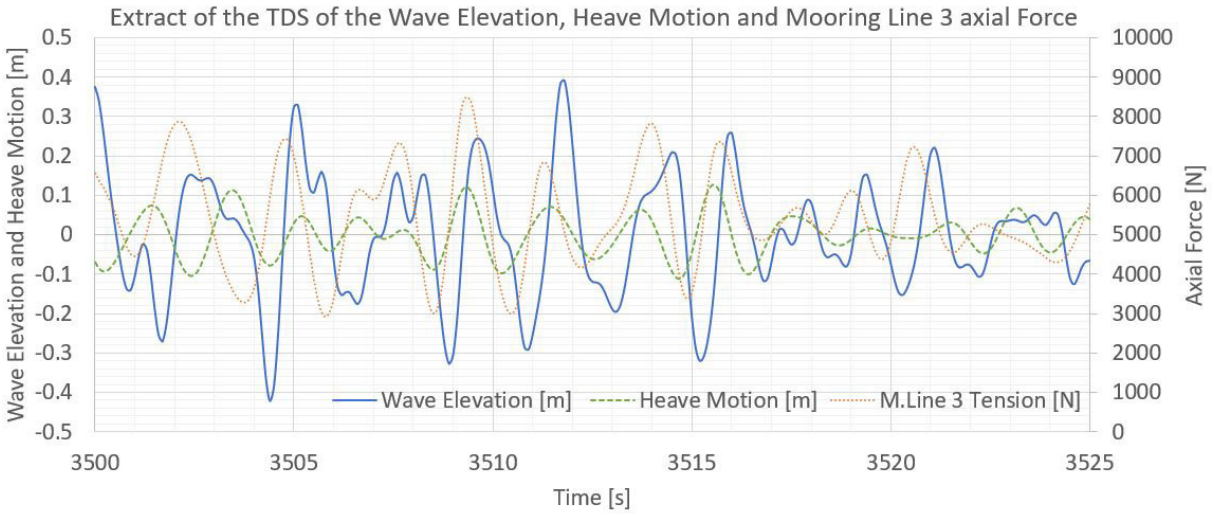

Figure 14.5: An extract of the TDS shows the wave elevation (blue-solid) alongside the heave motion of the structure (green-dashed) together with the mooring line tension at fairlead 3 (orange-dotted) interacting with a survival seastate

The analyzed motions in surge-, sway- and heave of the structure reveal that the surge motion is of both the largest amplitude and the largest mean offset in the design and survival case, as is presented in table 14.3. The data is the mean of ten individual runs with ten different wave seeds in the design and survival condition respectively, following the DNV-GL (2015) recommendations. This is done to reduce the statistical uncertainty, as one wave seed produces only one random wave time series. Hence are multiple wave seeds necessary to generate multiple wave time-series with the same characteristics in terms of significant wave height and peak period. The structure's response is ergo more reliable if it is taken as the mean of the maximum peaks of the ten runs performed.

The large mean offset in surge is explained by the strong wind force acting on the body while the displacement amplitude is caused by the interaction with the seastate. The small offset in sway is caused by the current flowing perpendicular to the dominant wave direction. A small offset in heave is also noted which is due to the additional weight coming from the mooring system. The heave and sway motion is dominated by the motion amplitudes rather than the mean offset, the later being the case for the surge motion, emphasizing that the mean load in surge due to wind is much larger than the mean load in sway caused by the current, and the mean load in heave due to the mooring arrangement weight. The lower mean submergence of the structure in the

survival case is due to the increased mooring line tension caused by the lager mean wind load in surge direction that physically pulls the structure downwards. The biggest heave submergence together with the still-water draft of 23.4 *cm* amounts to a dynamic submergence of 51.4 *cm* below the still-waterline, which leaves about 8 *cm* of reserve buoyancy. There is however a strong likelihood of greenwater on deck due to unfortunate phase shifts between the heave- and wave motion and the strong winds. Overall is the displacement of the structure the largest in the survival condition, due to the strong wind load acting in surge direction and the current acting in sway direction.

Table 14.3: TDS global motion response in the ULS and the design case, averaged from ten TDSs

Motion	Seastate	Max. Offset [m]	Max. Displacement Amplitude [m]	Mean Offset [m]
Surge	Design	1.99	0.79	1.20
	Survival	3.14	0.94	2.20
Sway	Design	0.19	0.18	0.01
	Survival	0.29	0.25	0.04
Heave	Design	-0.17	0.13	-0.04
	Survival	-0.33	0.28	-0.05

The motion response of the structure can also be presented as a response spectrum in terms of frequency, analog to the linear-theory response spectrum in section 13.3. The FFT command in the SIMO tool *port processor task* is used to present the heave amplitude as a function of frequency. The response spectrum can be plotted by squaring the amplitude and dividing it by twice the frequency step ($2 * \Delta\omega$). Figure 14.6 depicts the response spectrum in heave of the structure interacting with the design- (blue) and with the survival condition (green). The scattered plot in the background represents the peaks of the response spectrum and the lines in the foreground the smoothed response spectra. The respective design and survival JONSWAP wave spectra generated by SIMO are presented in figure D.2 in appendix D. The accuracy, how well the time series generated by SIMO compares to the waves spectra presented in figure 8.5, can be confirmed by the RMS of the respective spectra given in table 14.4.

Table 14.4: The RMS of the exact wave spectra and the ones generated by SIMO respectively

	Exact [m]	TDS [m]	Deviation [%]
RMS_{Des}	0.090073	0.090004	0.08
RMS_{Sur}	0.208921	0.208635	0.13

The first information that can be drawn from figure 14.6 is that the response peak for the design spectra is right in the vicinity of the frequency band carrying the most energy in the design JONSWAP wave spectra at 3.5 $\frac{rad}{s}$, around the frequencies identified in section 13.2 (refer to figure 13.8) that are likely to cause heave motion excitation. The survival heave response spectrum on the other hand is outside the peak of the survival JONSWAP wave spectrum which lies at 2.7 $\frac{rad}{s}$. The peak of the survival spectrum is more difficult to identify but can be pinned down to lie around 3.1 $\frac{rad}{s}$. This offset from the frequency band carrying the most energy in the seastate is the explanation for the comparably small difference between the design- and heave response spectrum, which was already observed for the linear frequency domain body motions

in section 13.3. Another particularity of the survival heave response spectrum is the formation of multiple peaks of varying height. The main peak does not distinguish itself as strongly from the surrounding ones as is the case for the design heave response spectrum, indicating that a greater variety of wave frequencies interacts with the structure. A further particularity is that the resonant heave motion only marginally excited. The heave response spectrum shows only a small peak in the vicinity of the natural frequency in heave at $Fn_{33} = 4.783\ \frac{rad}{s}$.

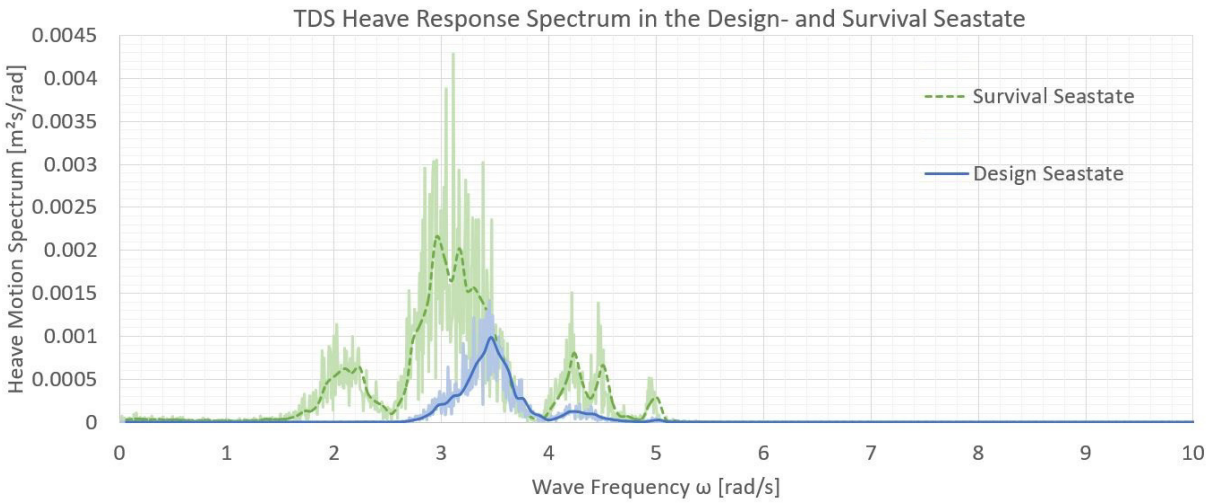

Figure 14.6: Comparison between the TDS heave response to the design- (blue-solid) and the survival seastate (green-dashed). The scatter plots in the background show the peak response spectra while the lines represent the smooth response spectra

The heave response can furthermore be compared to the linear response spectrum generated by HydroD. Figure 14.7 depicts the heave response spectra comparison between the linear theory results (green-dashed) and the TDS results (blue-solid) for the structure interacting with the design- (upper) and the survival condition (lower). The foremost observation is that the shape of both TDS heave response spectra is in good agreement with the shape of the linear heave response spectra. This indicates that the additional stiffness in heave due to the mooring system, which was not accounted for in the linear analysis in HydroD, has not been of such an extend as to gravely shift the TDS response spectra towards a higher frequency.

The second trend that can be identified from both figures is that the TDS results show generally lower motion amplification than the linear theory results, which is further confirmed by the RMS value of the respective response. The RMS for the TDS is 17.3 % smaller than the linear results in the design condition and 12.9 % smaller in the survival condition. This behavior can be explained by the friction damping implemented by SIMO acting on the mooring lines only, limiting the heave response amplitude. This damping is especially large in the realm of large amplitude heave motions, ergo motions of high heave motion velocity, resulting in larger damping. Of interest is furthermore the TDS result in the frequency band from $\omega = 4\ \frac{rad}{s}$ to $\omega = 5\ \frac{rad}{s}$ in the survival heave response spectrum. The TDS heave response has twice the amplitude then predicted by linear theory, which can only be explained by the systems natural frequency in heave. Fn_{33} is identified by a motion decay test of the structure and the mooring system carried out in SIMO and hence unavailable for the linear analysis. HydroD was hence not able to capture this affect and predict larger heave amplification at this frequency.

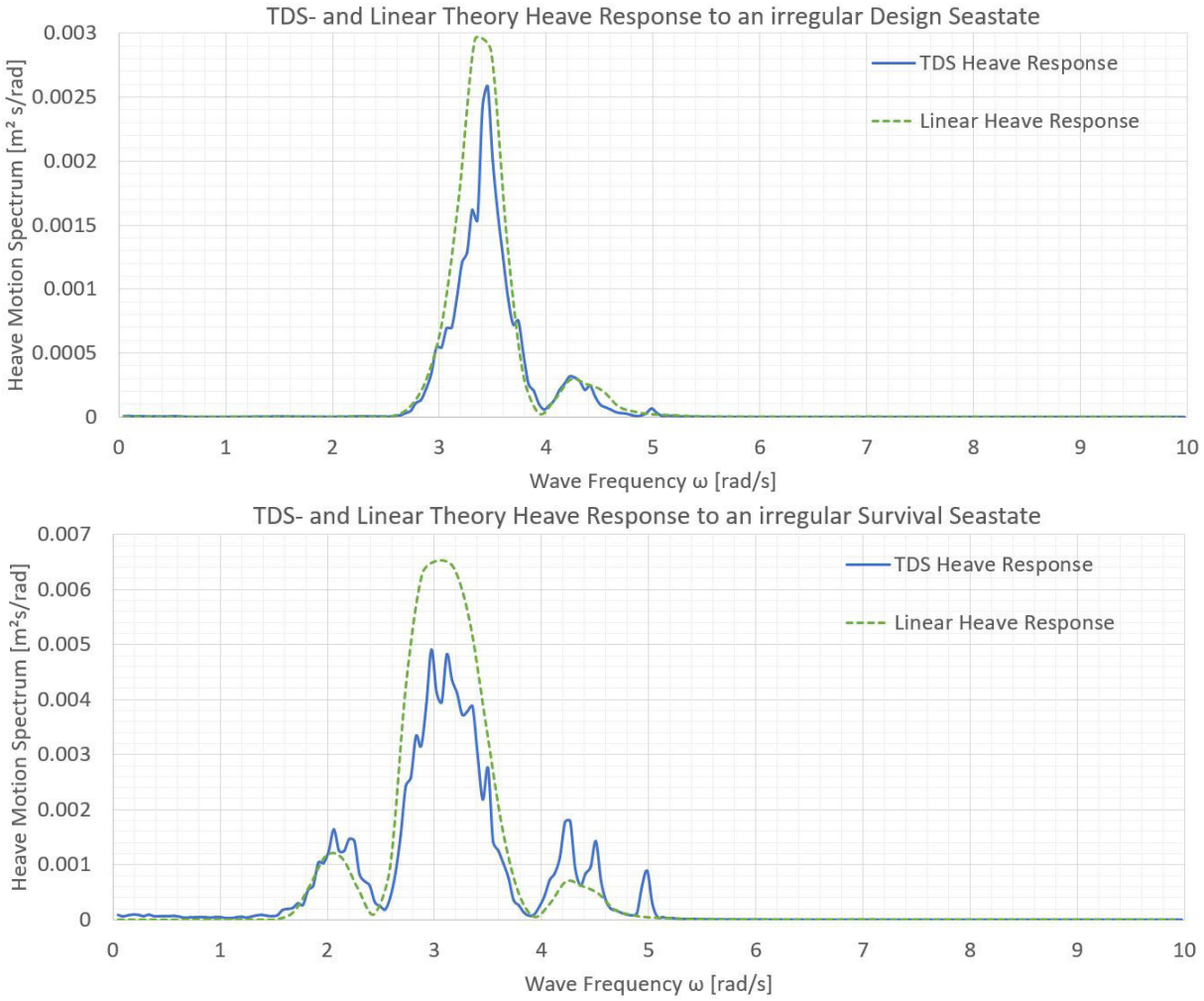

Figure 14.7: Comparison between the TDS heave response and the linear theory heave response of the structure interacting with a design- (upper) and a survival seastate (lower)

Beside the heave motion is the surge motion of the structure the most important motion to analyze, given that the structure operates at close quarters to other installations such as the algae- and mussel collectors. The surge motion further shows to have the largest displacement potential, as presented in table 14.3 and compromises a more complex behavior than the heave motion, as will be shown. The surge motion response of the structure facing a design- and a survival seastate is presented in figure 14.8.

Two characteristics of the plots presented in figure 14.8 immediately catch the eye: For one are the peaks for both spectra below $\omega = 1.5\ \frac{rad}{s}$, ergo representing low frequency (LF) motions. For another is the design response spectrum for the first time larger than the survival response spectrum, although the energy contained in the survival seastate is much higher. The later claim is supported by comparing the RMS value for both TDS surge motion spectra, which show that the RMS in the design case ($RMS_{11.Des} = 0.193\ m$) is 19.4 % higher than the RMS in the survival case ($RMS_{11.Sur} = 0.161\ m$). Both effects have to do with the circumstance, that short waves tend to trigger more pronounced second order effects than long waves, which

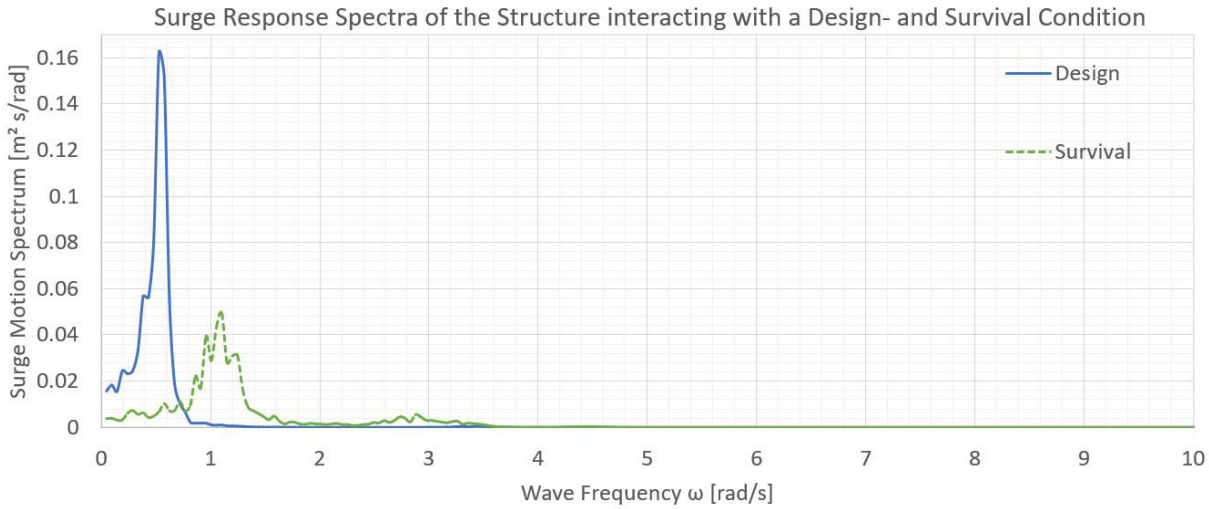

Figure 14.8: TDS surge response spectrum of the structure interacting with the design (blue-solid) and the survival condition (green-dashed)

is the case especially for the design condition (Gao, 2019), since the wave frequency (WF) load of the individual short wave is too high in frequency in order to trigger noteworthy WF surge motions of the structure.

The wave loads in surge acting onto the structure can be extracted from SIMO and are presented as spectra for the design seastate in figure 14.9. The plot comparing the first- and second order wave force response spectra of the design seastate shows that the second order forces are small compared to the first order forces, which, in comparison to the surge response spectrum in the design case in figure 14.8, allows the conclusion that the WF forces are not causing noteworthy surge motions. Looking at the surge response in greater detail reveals that the design surge response spectra peaks at around $\omega = 0.5\ \frac{rad}{s}$ which is in direct vicinity of the natural surge frequency $Fn_{11.22} = 0.437\ \frac{rad}{s}$ triggering high motion amplitudes.

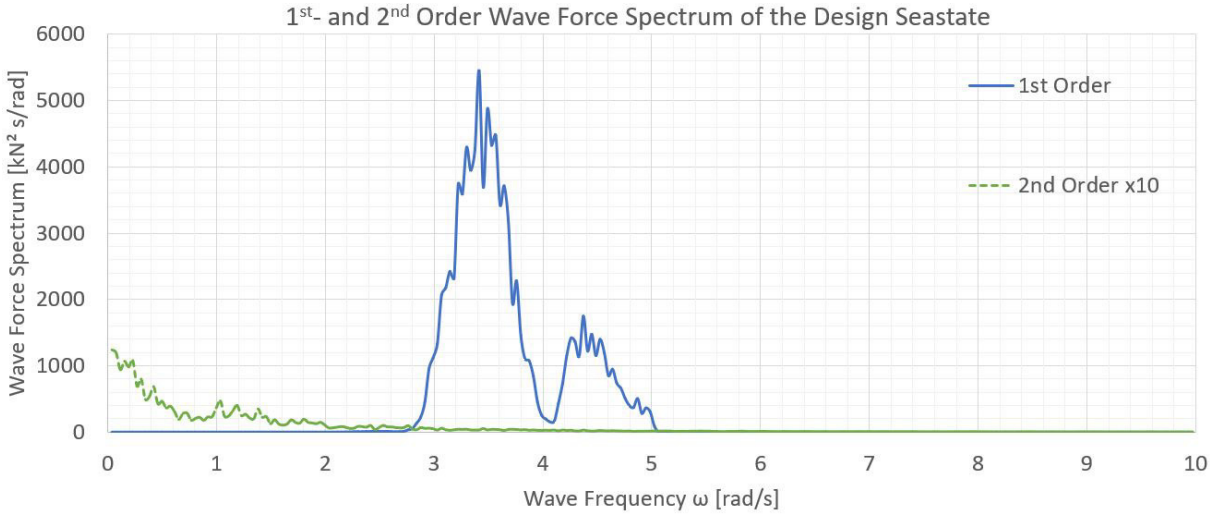

Figure 14.9: First- (blue-solid) and second order wave force response spectra (green-dashed) of the design seastate. The second order wave force response spectrum is multiplied by the factor 10

The peak of the survival spectrum is more difficult to explain as it compromises a highly nonlinear effect: The wind force acting on the body significantly stretches the windward mooring lines (lines three and four referring to figure A.1), which causes the mooring arrangement to react increasingly stiff, as large parts of the restoring force are supplied by the elastic elongation of the synthetic fiber mooring lines, not the displacement of the CW. This increased stiffness alters the restoring coefficient thereby dynamically shifting the natural frequency of the structure towards a higher frequency. The stiffness however still varies greatly with the instantaneous position of the structure causing not an isolated peak to form but a relatively wide frequency band of increased surge amplification to form from 0.8 $\frac{rad}{s}$ to 1.4 $\frac{rad}{s}$, as can be seen in figure 14.8.

The surge motions are for the large part caused by second order difference frequency wave loads, as the inexistence of a surge motion peak in the realm of WF loads in figure 14.8 shows. Further analyzing LF- and WF motions of the structure is hence important. Which motions are considered LF and WF respectively is decided upon using the surge response spectrum from figure 14.8. The frequency dividing LF- from WF motion is taken to be $\omega = 0.6\ \frac{rad}{s}$ in the design case and $\omega = 1.55\ \frac{rad}{s}$ in the survival case. Low- and high pass filtering of the TDS in SIMO enables the distinction between WF- and LF motions, as is depicted in figure 14.10. The two plots show a cut-out from the time series of the surge motion of the structure interacting with the design- (upper) and survival condition (lower). The difference between the design- and the survival condition is comparably large, analog to the surge response plot. The LF surge response of the structure in the design condition is much greater than the WF surge response, which is not the case in the survival condition. LF- and WF surge response of the structure in the survival condition are more difficult to distinguish from one another.

To better analyze LF- and WF motions it is useful to evaluate the characteristics of the LF and WF motions. The behavior of the moving natural surge period already witnessed in the surge response spectra finds itself again in the average motion period for the design- and survival condition in the upper plot of figure 14.11. The average LF surge motion period of the structure in the design condition is at 13.65 s, right beside the natural period in surge of the undisturbed structure $Tn_{11.22} = 14.393\ s$. The additional stiffness of the mooring system due to the wind- and wave loads also has an effect on the natural surge period in the design case, as the small shift of the motion response period towards a higher frequency shows. The effect is however not as pronounced as it is in the survival condition. The mean surge motion period at the survival condition is at 6.14 s, less than half than at design condition. The greater mean global offset presented in table 14.3 causes the mooring lines to stretch, resulting in a dramatically increased restoring coefficient causing the natural surge period to drop significantly. The WF motion periods are of almost the same length for both conditions, suggesting that WF motions have less to do with the stiffness of the mooring arrangement but with the WF loads acting upon the structure, which are much greater in the survival case than in the design case, as a comparison between the first order wave forces for the design- and the survival seastate in figure D.4 shows.

The characteristic of a small difference between LF- and WF surge motion in the survival case and a large difference in the design case can also be observed when looking at the mean and maximal amplitudes of the LF- and WF frequency surge motions in the design- and survival condition respectively. The lower diagram in figure 14.11 depicts these motion amplitudes. The observation made looking at the design TDS in figure 14.10 that WF surge motions are of less importance in the design condition is confirmed by the large amplitude difference between the LF- and WF surge motion in the design case. The mean of the WF surge displacement

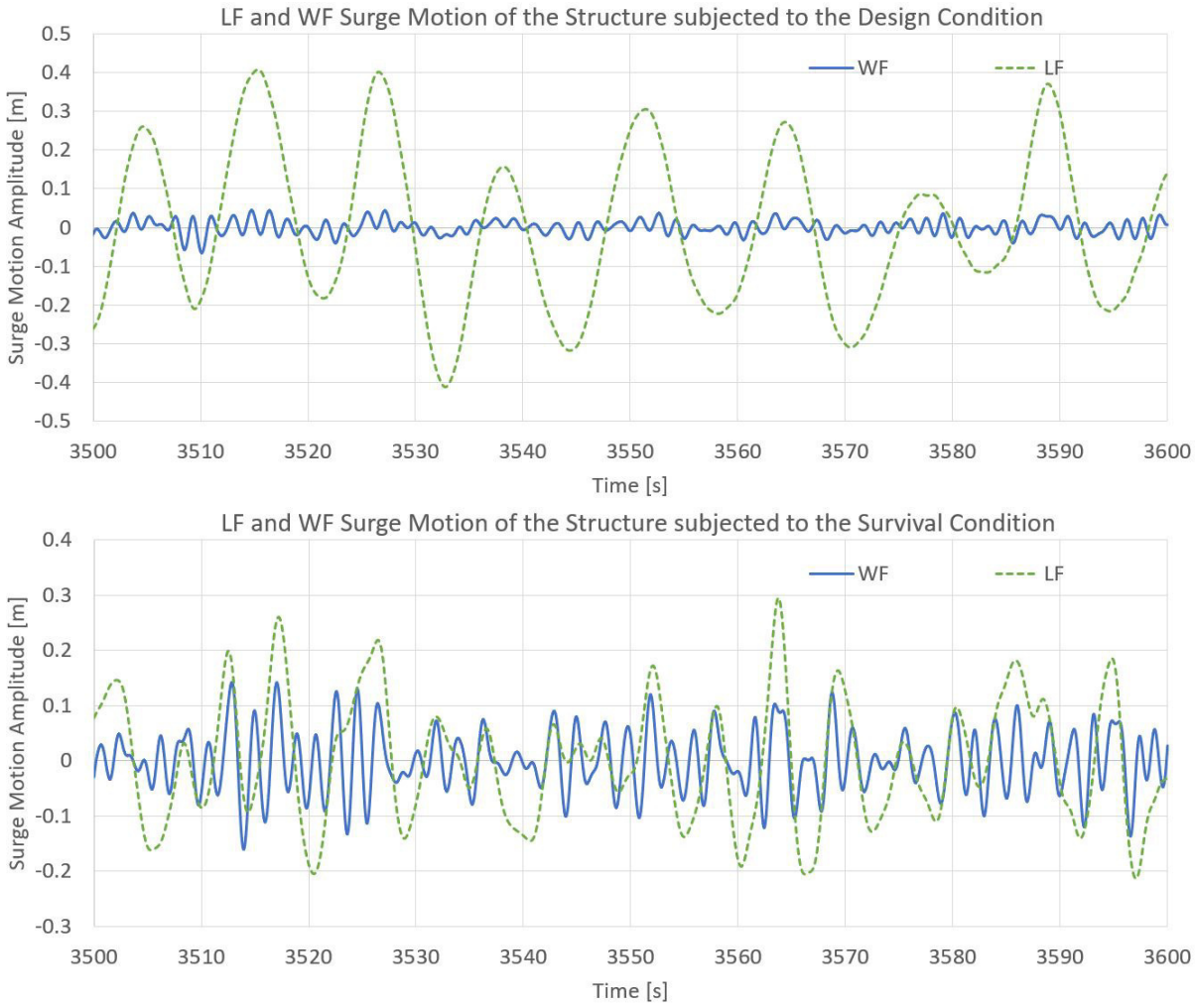

Figure 14.10: LF and WF surge motion TDS of the structure interacting with the design- (upper) and survival condition (lower)

in the design condition is only 9 % of the mean LF surge displacement, whereas the mean of the WF surge motion amplitude in the survival case is already 40 % of the mean LF surge motion.

Furthermore is the max LF surge motion amplitude in the design case bigger than in the survival case, which is in line with the surge motion response spectra in figure 14.8 but seemingly contradicts table 14.4 clearly stating that the largest global displacement amplitude occurs in the survival case. This comparison does however not hold since the overall displacement, the global displacement amplitude, closer to sum of the LF- and WF maxima is, which is bigger in the survival case. What can be said is that the movement of the structure in a survival seastate is more violent, since the LF motion amplitude is only marginally smaller than in the design condition. The WF motions are even larger, while the motion period of the LF motion is cut in half, resulting in disorderly, jerking motion characteristic.

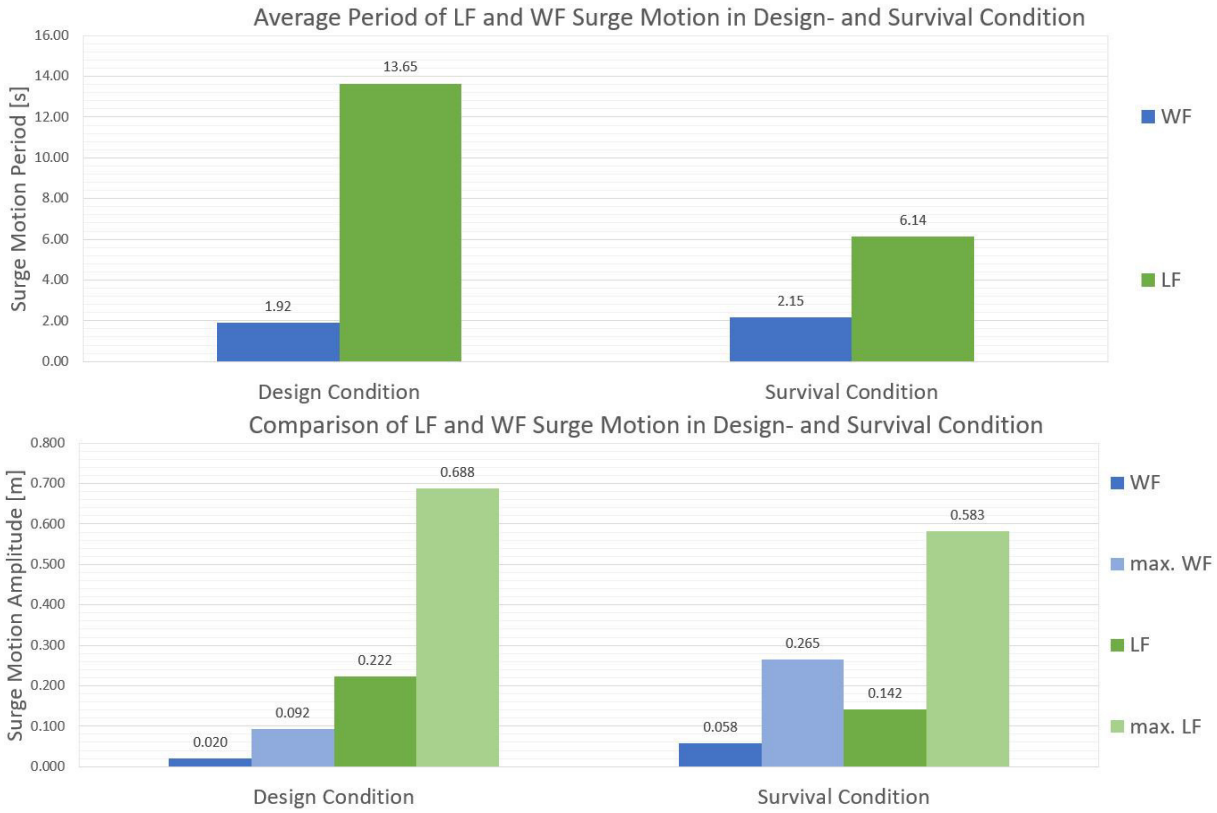

Figure 14.11: LF and WF surge motion TDS of the structure interacting with the design- (upper) and survival condition (lower)

14.2.2 Mooring Line Forces

Line failure possibly resulting in a freely floating structure is one of the greatest dangers when operating the structure. Due to the OS in the Bight of Kiel in direct vicinity of the shipping route connecting the Baltic- with the North Sea trough the NOK could the freely floating structure cause malice as it would interfere with the busy lock-traffic. Hence is accurately estimating the loads acting upon the mooring lines to correctly choose lines able to withstand the expected loads of utmost importance. This has a direct influence on the structure's overall cost as for mooring purposes appropriate synthetic fiber lines are increasingly expensive the stronger the line. As the mooring arrangement makes a large share of the overall installation cost given that the structure itself is low-cost design, could the overall cost be brought down significantly by carefully choosing the right mooring line type and cross section.

The mooring line forces are extracted from the TDS in SIMO, which allows to measure forces in the individual elements the mooring line is made up from. Two points, shown in red and blue in figure A.1, are chosen to measure the forces in each mooring line: The first point is right at the fairlead of the structure since this is the point where the biggest mooring line forces are expected, as the whole weight of the mooring arrangement is supported by the fairleaders. Though the capacity of the mooring arrangement at this location is not critical, given that the upper part, the part connecting the CW and the structure, is made from high-capacity steel chain, is the knowledge about loads at this point important for the manufacturer of the structure to correctly dimension the capacity of the fairleaders.

The second point where force is measured is right beneath the CW, connecting the synthetic fiber line with the CW. This point is critical in the aspect that the biggest loads in the lower part of the mooring arrangement can be expected at this location. Furthermore is the connection between the synthetic line and the steel chain a point known to fail due to wear as the steel deteriorates the fibers. Although this phenomenon can not be simulated with SIMO, knowing the load at this point allows to better establish a safety mechanism, e.g. a thicker rope, to prepare for this phenomenon. The axial force acting within the mooring line is presented by SIMO as depicted in figure 14.12. The graph shows the axial force at fairlead 3 in a survival condition. The time window is exemplary as it shows the complex reaction of the mooring system as well as a whipping phenomenon at $t = 3506\ s$ caused by the jerking motion of the structure already mentioned in section 14.2.1.

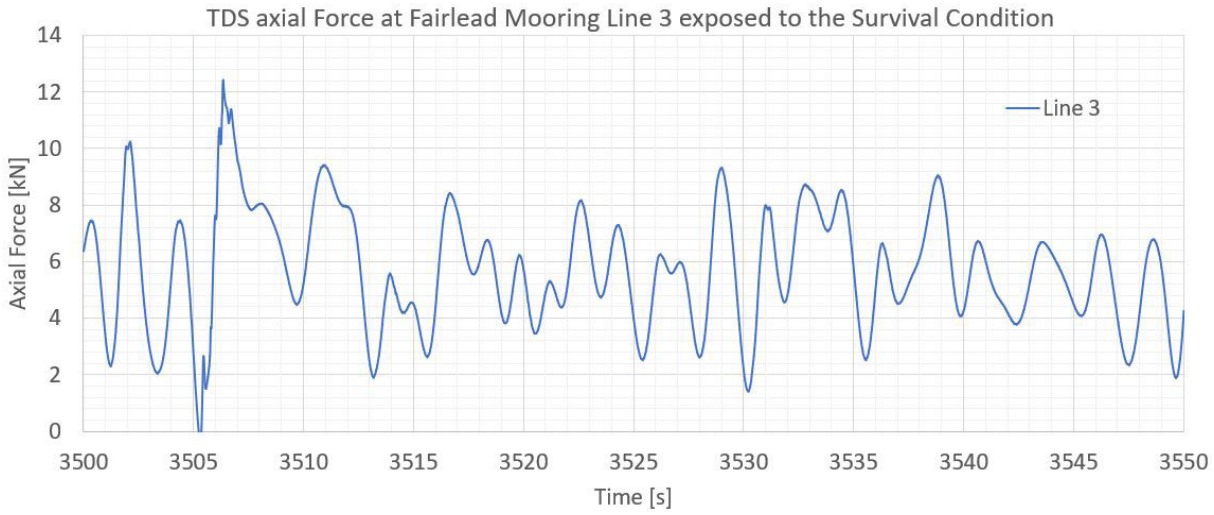

Figure 14.12: TDS of the axial force acting in line 3 at the fairlead when the moored structure is subjected to the survival condition

Before going into the magnitude of the forces and the effect this has on the mooring line used, it is important to know which motions and loads cause the axial forces in the mooring lines. The easiest way is again to plot an axial force response spectrum, which is done in figure 14.13 for line 3 as line 3 is the most heavily loaded line in the mooring arrangement. Figure 14.13 depicts the axial force at fairlead 3 in the design- and the survival condition. The load is the greatest in the survival condition, however do both spectra compromise a peak in the LF range and one in the WF range, whereas the later is significantly larger than the LF peak, especially in the design case. This corresponds well with the mean- and maximal axial force period in figure D.6, which shows that the mean period is in the realm of the WF loads, while the maximal period corresponds to the natural period in surge of the structure in the design- and survival condition respectively.

The question remains which motion causes the peaks in line tension. A distinction between WF- and LF force components in the design case becomes obvious, with the WF forces being of greater magnitude than the LF forces. The origin of the LF force component is easily found when looking at the surge motion response spectrum for the design case in figure 14.8: LF surge motions cause the LF loads. It is however noteworthy that surge motions are not the leading

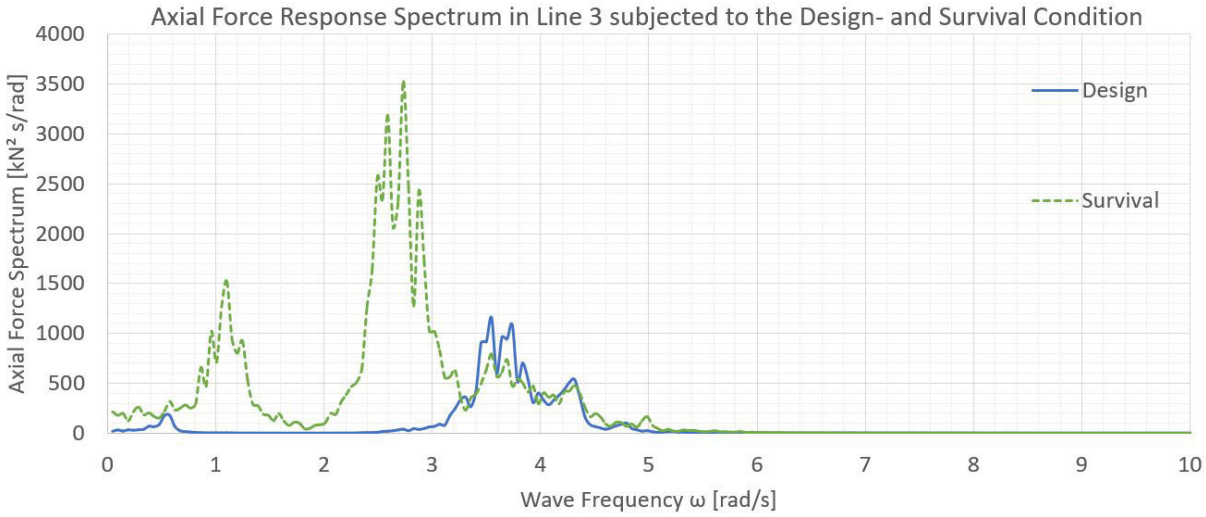

Figure 14.13: The axial force response spectra on fairlead 3 are presented for the structure in the design- (blue-solid) and survival condition (green-dashed)

cause of rope tension, given that the surge motion is governing the motion characteristic of the structure. The motion causing the bulk of axial forces is the heave motion of the structure interacting with the design condition. The peak force is in the realm of the heave motion response peak, as the comparison of figure 14.13 with figure 14.7 shows. This seams to falsify the assumption made in section 13.1, that heave is governed by hydrostatic restoring. Looking at the good coherence between the linear potential theory- and TDS results in figure 14.7 however shows that the influence of the restoring force from the mooring system on the heave motion characteristic is negligible, as the TDS results would have otherwise been shifted, confirming the statement, that the heave motion is *dominated* by hydrostatic restoring, is still true.

The cause of the dominant peak in the axial force response spectrum for the survival case is however not found in the heave motion response of the structure. The LF force response peak in figure 14.13 can be explained analog to the design case with the LF surge motion, the WF peak can however not be explained in the same matter. While the LF peak is in the frequency band identified earlier as the natural period in surge for the moored structure in the loaded condition (tight mooring lines), is the cause of the WF force response found in the pitch motion of the structure. This can be shown looking at figure 14.14 depicting the pitch motion response spectra of the structure in the design- and survival case. The spectrum compares well to the linear pitch motion response presented earlier in figure 13.13, ergo a small pitch amplification in the design condition and a large amplification in the survival condition. Now comparing the survival condition axial force response spectrum in figure 14.13 with the survival condition TDS pitch motion response spectrum in figure 14.14 shows a good coherence between the pitch motion response peak with the WF force response peak.

The pitch motion causing the peak mooring line loads in the survival condition further explains the whipping phenomenon already witnessed in the TDS force plot in figure 14.12. It is easy to imagine the structure violently pitching, tugging on the mooring lines. The mooring loads in the design condition are ergo caused by surge- and heave motions while surge- and pitch motions are responsible for the bulk of the loads in the survival condition. The term *bulk* is used since heave motions also marginally contribute to the mooring loads in the survival condition.

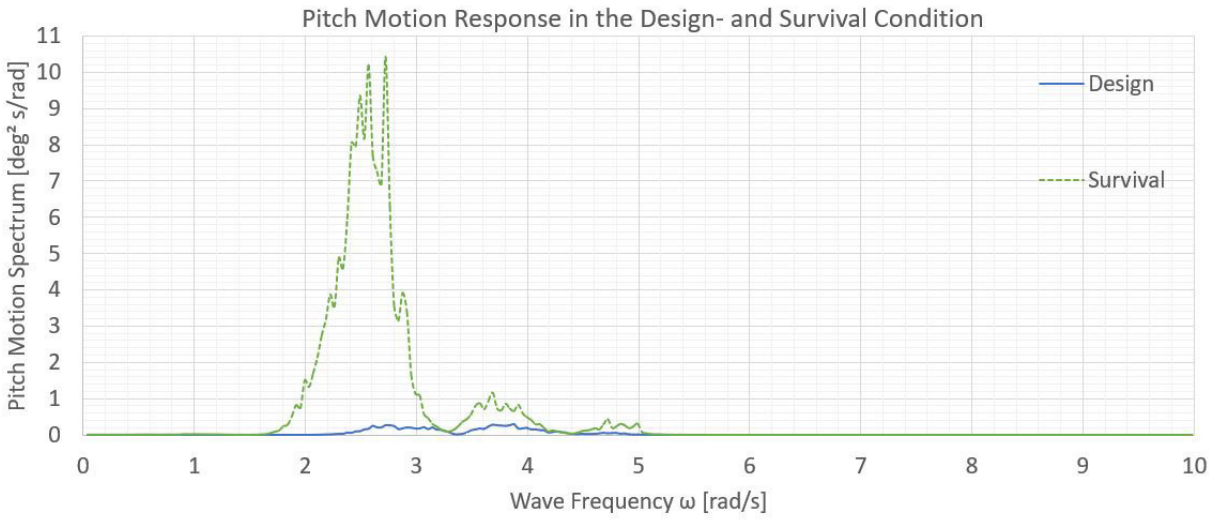

Figure 14.14: TDS pitch motion response spectra of the structure in the design- and survival condition

Looking at the magnitude of the forces shows the hypothesis approved, that the windward lines are especially loaded. Figure 14.15 presents the axial force at the CW and the fairlead of each mooring line in the design- and survival condition. The force values represent the mean of ten runs with ten different wave seeds for the design- and survival condition and is gathered analog to the global motion response in table 14.3. Further is only the mean of the fairlead force presented as it proved to be greater than the mean force at the CWs. In both conditions, design- and survival-, is mooring line 3 the most heavily loaded one. This is due to the wind- and wave loading acting along the global x-axis and the current along the y-axis. The resulting force vector is hence aligned the closest with mooring line 3.

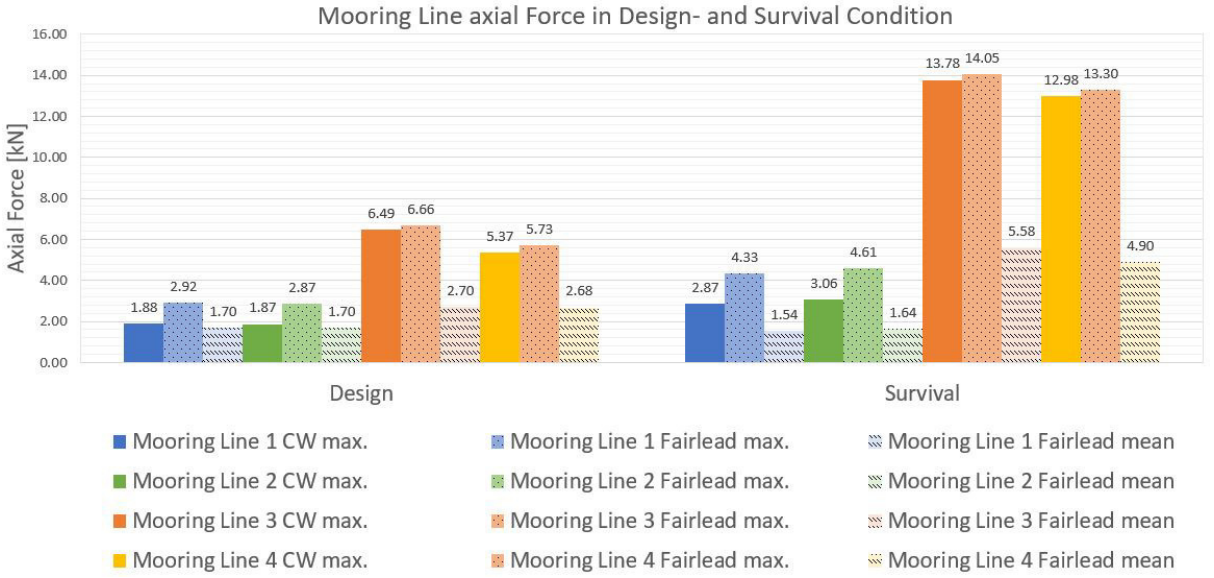

Figure 14.15: The most probable mean- and max. axial forces on the mooring system taken from a total of ten runs measured at the fairlead and the CW in the design- and survival condition

The strength of the components can now be chosen based on the loads on the mooring system in figure 14.15. In order to apply to widely accepted standards, the minimum braking strength (S_{MBS}) of the mooring system components is based on the DNV-GL (2015) offshore standard. The standard considers the most probable mean- and max. loads experienced by the mooring arrangement alongside a safety factor for mean- and dynamic (dyn) tension, following equation 14.1.

$$S_{MBS} \geq \frac{T_{C.mean}\gamma_{mean} + T_{C.dyn}\gamma_{dyn}}{0.95} \tag{14.1}$$

The method used requires the definition of a *consequence class* which influences the safety factor for the mooring lines. Two consequence classes are available: consequence class 1, where a mooring system failure resulting in consequences such as loss of life, capsizing or sinking, and collision with adjacent platforms is unlikely, and consequence class 2, where the consequences mentioned above are possible. After considering that no one will be aboard the structure during the ULC, that capsizing is unlikely due to the GM being at $GM = 29.7\ m$ and that there are no adjacent platforms in sight is consequence class 1 applied to this installation. The factors γ_{mean} and γ_{dyn} are hence chosen as $\gamma_{mean} = 1.10$ and $\gamma_{dyn} = 1.50$. The characteristic mean tension $T_{C.mean}$ and the characteristic dynamic tension $T_{C.dyn}$ are taken from figure 14.15 as $T_{C.mean} = 5584\ N$ and $T_{C.dyn} = 14050\ N$. Equation 14.1 hence gives the minimum breaking strength of every component of the mooring system as $S_{MBS} = 28649.9\ N = 28.7\ kN$.

The mooring arrangement parts can consequently be chosen based on the S_{MBS}. For the chain however comes another requirement into effect, which is already mentioned in section 10: the chain needs to be a long-link chain in order to pull up the mooring arrangement for inspection. In order to fit the crane hook into the individual chain links is the Trawlex® long-link chain chosen, with an inner diameter of 26 mm $*$ 100 mm and a link thickness of 16 mm. This chain fulfills the strength requirement too as its S_{MBS} is at 392.4 kN. The rope chosen is a polypropylen/polyethylen rope, commonly referred to as *polysteel* or *danline*. It comes in various thicknesses, from 6 mm to 32 mm in 2 mm steps. Looking at the strength requirement only would a 14 mm thick rope with a breaking strength of 35.4 kN already be sufficient. However, considering the wear in this environment and that neither a FLC nor an ALC was conducted, recommends the author the use of an at least 16 mm thick rope with a breaking strength $\geq$ 44.9 kN. This already in-cooperates another effect observed at the OS: barnacles, small mussels with sharp corners, settle on the rope, especially where the rope surface is not smooth due to knots or splines, ergo on attachment points between two components. Repetitive movement now causes the barnacle shells to cut through the outer fibers of the line, weakening it. Additional rope thickness can hence ensure that the S_{MBS} is not undercut.

15 Operability

The operability is an integral part of any concept design of a structure. The operability is in this aspect a measure of how well suited an installation is to carry out a given task in a given environment, ergo to which degree the structure enables these operations, to which extends it allows for these operations in increasingly bad seastates and how long these operations will be possible given which maintenance. This permits the one running the farm to estimate which revenue can be created by purchasing this structure. A good operability study hence supplies information about the response towards certain environments, defines a limit up to which operations are possible and consequently estimates a downtime based on these limits and the environmental data gathered at the OS. Furthermore is data about the operational life span supplied along with recommendations on how to service and maintain the structure to ensure functionality.

Conducting an operability study is in this thesis however difficult due to the lack of information about important aspects. One critical aspect is the missing information on how operations on the farm are carried out, which could be used as a guideline on how to limit the deployment of the structure. Hence are the NORDFORSK (1987) criteria applied to on the one hand give a general task to be carried out and on the other to roughly define tolerable motions of the structure. In this case was the vertical acceleration RMS limit set to $0.1g$, which, following NORDFORSK (1987), still allows for "Intellectual work by people not so well adapted to ship motions. For instance scientific personal (...)". Comparing this guideline to the RMS of the potential theory heave acceleration response spectrum in figure E.1 giving $RMS_{33.Sur} = 0.025g$ shows that even the heave acceleration in the survival case is below the allowed acceleration threshold, emphasizing that accelerations of the structure are not the limiting factor when it comes to operations on the farm.

Even if detailed acceleration limits are available for the tasks carried out on the structure would an operability estimation be difficult due to the absence of environmental data at the OS. This is the reason the environment is defined following maximal values, in this case wind speeds, as information on neither wind speeds nor wave heights are to the author's knowledge available. This however makes the estimation of the downtime of the structure difficult, given that the likelihood of the wind speeds reaching 6 bft and 9 bft is unknown. What can however be proclaimed is that the times of high wind speeds occur mostly in the winter season, a season the plants on the structure and hence the operations on the farm lay mostly dormant, suggesting a low downtime of the structure.

16 Conclusion

The thesis about the concept design of a support structure for hydrophyilic crop commences with describing the setting the structure is aimed to be operating in. The concept of aquaculture, halophytic farming and MU-IMTA is explained. Subsequently is the concept development of the structure discussed by summarizing what has been found out in the foregone project thesis and how the experience working at the OS of the OFK altered the previous design resulting in a concept design of a floating structure passively irrigated by seawater. The methods and tools used to further analyze the structure are consequently laid out followed by a presentation of the results gathered with the methods described, which are discussed concludingly.

The result of the work is a concept design of a passively irrigated structure with a good likelihood to supply a support enabling the growth of Salicornia, moored with a hybrid taut line CW four-point mooring system. Although the structure's net-growing area of 11.6 m^2 deviates from the initial 25 m^2 growing area requirement, which was reduced to decrease the structure's complexity and making the installation manageable for the OFK, enables the structure the farming of Salicornia in multiple modular and hence interchangeable flowerbeds. The for the production of Salicornia unfavorable ratio between growing area and total deckspace (11.6 m^2 to 60.5 m^2) offers on the other hand enough capacity to carry out research and to ease planting and harvesting of products within and surrounding the platform, sharpening the initial profile of the structure to act as a nucleolus of a MU-IMTA.

The motion characteristic of the structure, as linear- and time domain simulations confirmed, is complex but overall suited for the intended purpose considering the generally low amplifications of rigid body motions. The high linear wave radiation damping alongside the unconventional floater arrangement contribute to the absence of dominating motions response peaks causing substantial motion amplification. The low response amplitudes are further put into perspective regarding that viscous damping on the structure and the modeling of the flowerbeds is neglected. Modeling of the later would significantly lower the motion amplitudes in heave and pitch as the water would flow in and out of the flowerbeds seriously increasing viscous damping, while modeling of the former would dominantly reduce the horizontal displacements in surge in sway.

The negligence of sum-frequency effects on the other hand does not have a large effect on the generally moderate body motion amplifications, as the mooring arrangement stiffness in surge, sway, roll and pitch is relatively low. Although the stiffness in heave is substantial due to the large water plane area is the error introduced by neglecting sum-frequency effects limited, as the potential damping in heave is large, making strong heave amplifications unlikely. Although the rigid body motions in all DOF are generally low must these be regarded when operating the structure. Ergo, answering the question if operations can be carried out at the design condition: Probably no. The surge motions of the structure would make a safe mooring of the support vessel to the structure unfeasible. The greatest obstacle would however be the wind, which would make any activity on the platform surrounding the growing area challenging. Furthermore causes the mean displacement in surge during the survival condition the mooring line to interfere with the mussel collectors surrounding the farm, as wind force tightens the mooring line. This will consequently cause a loss of mussels from the collectors. This risk is however inevitable, since a larger CW weight is operationally not feasible and passable, as the survival condition is expected to be rare.

Hydroelasticity is also neglected in the present work. The body is considered to be rigidly moving and not being deformed by the interaction with the environment. The change in the body's hydrostatic coefficients due to hydroelasticity is however considered limited since the overall dimensions of the structure are still considered large compared to the dominant wave height and length, making strong hogging and sagging phenomena unlikely. Further requires the estimation of hydroelasticity a far greater knowledge of the structure's construction details and hence an analysis with a whole different aim which is not covered here.

The mooring arrangement designed performs well, given the harsh limitations set for it, e.g. the small footprint- and cost efficient ease of installation requirement. The CW guarantee that the mooring lines stay clear of the mussel collectors on the one hand and on the other hand shift the natural period in surge well outside the first order wave excitation frequencies. The unconventional hybrid mooring line setup, with the implementation of chain link on the upper parts and synthetic fiber line on the lower, reduces the investment cost of the mooring arrangement further enabling the OFK to easily monitor the mooring line, all while keeping the additional weight of the total mooring arrangement at a minimum, maximizing the payload capacity of the structure. The survival case however revealed the flaw of the mooring system: Should the constant horizontal wind load become too large is the mooring system only marginally able to cope with first and second order wave force peaks, as the restoring force at this point is mainly provided by the elongation of the synthetic fiber lines, not the displacement of the CW, as the most heavily loaded mooring line is fully stretched out. This limits the mooring arrangements capabilities to absorb dynamic peak loads and shifts the natural surge period towards higher frequencies and hence towards the realm of the wave frequencies of the survival seastate. However is the survival condition defined as to be extremely rare in this part of the Bight of Kiel. It is furthermore quite likely that the greenhouse collapses under the strong wind loads, reducing the overall wind load on the structure by 85 %, making a full stretch of the mooring lines unlikely. Overall is the presented structure well capable of performing the task at hand.

17 Future Work

The work presented concentrates on the fundamentals necessary to establish a working concept design. Many important factors are inevitably left out and essential questions are not discussed. Especially the mooring analysis lacks important information. The presented thesis does not consider neither the ALC nor the VLC, as DNV-GL (2015) requires. The consequence, what would happen if line 3 breaks, can only be crudely estimated. To prevent this from happening and enable lines 1, 2 and 4 to take the additional load, should this accident happen, is the recommended line strength 164 % that of the DNV requirement. Furthermore is the FLC of the mooring arrangement not considered. This is especially critical as the fatigue behavior of synthetic fiber mooring lines is much more complex compared to conventional mooring chain and hence more difficult to estimate. DNV-GL (2015) guidance note 111 emphasizes that the mooring line stiffness of synthetic fiber lines increases over time, among other changes in the characteristic of the line, shifting the the natural response period of the system towards higher frequencies.

Besides the negligence of important operational conditions as the ones mentioned above is viscous damping on the structure neglected as well. Motion damping of the structure only comes from linear waves-radiation damping while viscous damping is only regarded on the mooring lines, as a SIMO default. This has an impact as it causes the motion, especially motions connected with little potential damping, to experience larger oscillation amplitudes then in reality. This however enables a conservative estimate. Including viscous damping of the structure and the flowerbeds could hence improve the significance of the results.

Furthermore is the mooring system in its present form not optimized. The length of the individual components as well as the weight of the CW was chosen based on technical and operational feasibility as well as the avoidance of contact with surrounding installations, not on the performance of the mooring system itself nor the loads on the mooring lines. The motion characteristics of the structure could be better and the mooring hardware more fit for the intended purpose, would the mooring arrangement be optimized.

The last flaw in the general mooring system analysis is the negligence of waves, wind and current coming onto the structure from different directions. Only head sea waves and wind as well as current perpendicular to the x-axis are considered, as this arrangement best represents the future working condition at the OS in the Bight of Kiel. However could thereby be cases left out which would result in much higher loads on the structure, e.g. if the waves came from 45° of port- or starboard side. An optimization spiral of the mooring system, seastates coming from different headings and the analysis of the ALC and FLC are not carried out, leaving territory to be explored by adjacent examinations of the mooring arrangement.

There are further flaws in this report, most notably the precise definition of environmental conditions. Except for the current at the OS, which was measured by CRM in 2017 and 2018, is the basis of the environmental condition solely defined by the wind speed, 6 bft and 10 bft respectively. The later information is based on the BC set by the OFK, not measured wind speeds at the OS. Although the resulting wave height calculated following Engineers (2008) compares well to the maximal wave charactersitics observed by Captain Finnberg (2019), does this still not give a likelihood of occurrence of these seastates. Performing operability estimations and estimating a down-time of the vessel is hence difficult, as mentioned in section 15. Covering this

gap could ergo greatly improve the present report, adding an important piece of information vital for the OFK to plan the operations on the MU-IMTA at the OS. Furthermore is the wind applied as a constant load, not a fluctuating one, as is usually the case. Important interactions between the fluctuating wind load and the structure, such as resonant low frequency surge motions due to wind, are thereby neglected. Future assessments of the structures interaction with the environment should hence evaluate this behavior too.

The structure functioning as a nuclei of a highly integrated aquaculture was also not given the necessary attention. The influence of e.g. mussels growing under the farm on the motion characteristic of the structure, should the structure be extended in a similar way at a later stage, is neglected in the WBI calculations. This also compromises multi-body motions, e.g. between a service vessel and the structure or the structure and an adjacent structure, which would change the WBI and could increase the loads on the mooring lines significantly. Furthermore are other class relevant calculations not carried out, such as a damage stability analysis of the structure. All in all are many details, such as a detailed concept of a adjustable flowerbed support mentioned in section 6.2 to alter the flowerbed submergence, missing in the present report and should be addressed prior to ordering the structure at the manufacturer.

References

Abdelly, C., Debez, A., Smaoui, A., and Grignon, C. (**2010**). "Halophyte-Fodder Species Association May Improve Nutrient Availability and Biomass Production of the Sabkha Ecosystem." *Tasks for Vegetation Science: Sabkha Ecosystems*, 46: 85–94.

Altieri, M. A. (**2016**). *Modern Agriculture: Ecological impacts and the possibilities for truly sustainable farming*. University of California, Berkley, CA, USA.

Brorsen, M. (**2007**). *Non-linear Waves*, volume 9. Department of Civil Engineering, Aalborg University, Aalborg, Denmark. Lecture Notes.

Buck, B. H., Nevejan, N., Wille, M., Chambers, M. D., and Chopin, T. (**2017**). *Aquaculture Perspective of Multi-Use Sites in the Open Ocean*. Springer, Berlin, Germany.

Chakrabarti, S. K. (**2005**). *Handbook of Offshore Engineering*, volume 2. Elsevier, Kidlington, Oxford, United Kingdom.

Crossland, C., Kremer, H., Lindeboom, H., Marshall Crossland, J., and Le Tissier, M. (**2005**). *Coastal Fluxes in the Anthropocene - The Land-Ocean Interactions in the Coastal Zone Project of the International Geosphere-Biosphere Programme*. Springer, Berlin Heidelberg, Germany, 1 edition.

Cummins, W. (**1962**). *The Impulse Response Function and Ship Motions*. David Taylor Model Basin, Bethesda, MA, USA. Technical Report.

Delights, E. (**2018**). *Fresh Sea Beans*. Okemos, MI, USA. URL: http://www.earthy.com/Fresh-Sea-Beans-from-Earthy-Delights.aspx (2018-12-06), Website.

DNV (**2010**). *Recommended Practice DNV-RP-C205: Environmental Conditions and environmental Loads*. Det Norske Veritas, Hoevik, Norway. Technical Standard.

DNV (**2011**). *Rules for Classification of Ships DNV-RU-Pt.3Ch.3: Hull Equipment and Safety*. Det Norske Veritas, Hoevik, Norway. Technical Standard.

DNV-GL (**2015**). *Offshore Standard DNVGL-OS-C301: Stability and watertight integrity*. DNV GL, Hoevik, Norway. Technical Standard.

DNV-GL (**2019**). *Sesam user course at Marintek, NTNU*. DNV GL, Trondheim, Norway. Lecture Notes.

Engel-Netze (**2019**). *Katalog 2019-2020*. Engel-Netze GmbH und Co. KG, Bremerhaven, Germany. Sales Catalogue.

Engineers, U. A. C. o. (**2008**). *Coastal Engineering Manual*. U.S. Army Corps of Engineers, Washington, D.C., USA. Technical Standard.

Faltinsen, O. M. (**1993**). *Sea Loads on Ships and Offshore Structures*. The Press Syndicate of the University of Cambridge, New York, USA.

Finnberg, C. M. (**2019**). *Wave Conditions in the inner Bight of Kiel*. Pilot Association North-Baltic Sea Canal II, Kiel, Germany. (2019-02-27), Personal Communication.

Gao, Z. (**2019**). *First and Second Order Wave Load Impact on Motion Response of Floating Structures*. NTNU, Trondheim/Kiel, Norway/Germany. (2019-05-28), Personal Communication.

Gao, Z. and Moan, T. (**2009**). "Mooring system analysis of multiple wave energy converters in a farm configuration." *Proceedings of the 8th European Wave and Tidal Energy Conference, Uppsala, Sweden*.

Google (**2019**). *Google Maps Kiel*. Alphabet Inc., Mountain View, CA, USA. URL: https://www.google.de/maps/place/Kiel/ (2019-02-18), Website.

Greco, M. (**2018**). *Sea Loads*. Dept. of Marine Technology, NTNU, Trondheim, Norway. Lecture Notes.

Hall, N. (**2015**). *Shape Effects on Drag*. Glenn Research Center, Cleveland, OH, USA. URL: https://www.grc.nasa.gov/www/k-12/airplane/shaped.html (2019-03-24), Website.

Hamed, K. B., Magné, C., and Abdelly, C. (**2014**). "From Halophyte Research to Halophytes Farming." *Tasks for Vegetation Science: Sabkha Ecosystems, Cash Crop Halophyte and Biodiversity Conservation*, 4: 135–42.

Holm, P., Buck, B. H., and Langan, R. (**2017**). *Aquaculture Perspective of Multi-Use Sites in the Open Ocean*. Springer, Berlin, Germany.

Huhnt, M. (**2018**). *Preliminary Concept Design of a Support Structure for Hydrophilic Crop*. Norwegian University of Science and Technology NTNU; Royal Institute of Technology KTH, Trondheim, Norway. Project Report.

Jahn, M. (**2019**). *Construction of a Floating Farm*. Alu Bau GmbH., Büdelsdorf, Germany. (2019-02-07), Personal Communication.

Lewis, E. V. (**1989**). *Principles of Naval Architecture*, volume 3. The Society of Naval Architects and Marine Engineers, Jersey City, NJ, USA.

Lovatelli, A., Aguilar-Manjarrez, J., and Soto, D. (**2016**). *Expanding mariculture farther offshore - Technical, environmental, spatial and governance challenges*. Food and Agriculture Organization of the United Nations, Rome, Italy.

Musselman, L. J. and Wiggins, h. J. (**2013**). *The Quick Guide to Wild Edible Plants : Easy to Pick, Easy to Prepare*. Johns Hopkins University Press, Baltimore, MD, USA.

Newman, J. N. (**1974**). "Second order, slowly varying forces on vessels in irregular waves." *International Symposium Dynamics of Marine Vehicles and Structures in Waves*, pages 182 – 8.

Nissen, N. (**2019**). *Ocean Farm Operations*. Ocean Farm Kiel, Kiel, Germany. (2019-01-21), Personal Communication.

NORDFORSK, T. N. C.-o. P. o. S. P. o. S. (**1987**). *Assesment of Ship Performance in a Seaway*. Nordic Co-operative Organization for Applied Research, Copenhagen, Denmark. Technical Standart.

Ogilvie, T. F. (**1964**). *Recent Progress toward the Understanding and Prediction of Ship Motions*. David Taylor Model Basin, Washington, D. C., USA. Technical Report.

Rosén, A. (**2017**). *Introduction to Seakeeping*. KTH Centre for Naval Architecture, Stockholm, Sweden.

S. Haas, Y. R., Schröder, J., Bronnmann, J., Jooss, F., Loy, J., and Schulz, C. (**2015**). *Konzeptionierung einer umweltverträglichen, marinen Aquakultur in Schleswig Holsteinischen Ostseeküstengewässern*. Christian-Albrechts-Universität, Gesellschaft für Marine Aquakultur mbH, Kiel/Büsum, Germany.

SINTEF-Ocean (**2018**). *RIFLEX Manuals*. Sintef Ocean, DNV-GL, Trondheim, Norway.

Staufenberger, T. (**2018**a). *Ocean Farm*. Ocean Farm Kiel, Kiel, Germany. (2018-10-23), Personal Communication.

Staufenberger, T. (**2018**b). *Salicornia demand*. Ocean Farm Kiel, Kiel, Germany. (2018-11-16), Personal Communication.

Staufenberger, T. (**2019**). *Water Density in the Bight of Kiel*. Ocean Farm Kiel, Kiel, Germany. (2019-01-23), Personal Communication.

Ventura, Y., Eshel, A., Pasternak, D., and Sagi, M. (**2015**). "The development of halophyte-based agriculture: past and present." *Ann Bot*, 115(3): 529–40.

Weller, S., Johanning, L., and Davies, P. (**2013**). *Best practice report - mooring of floating marine renewable energy devices*. University of Exeter, Exeter, United Kingdom.

Yvonne, V., Wegi, A. W., Malika, M., Zerekbay, A., Inna, K.-G., Muki, S., Tzachi, M. S., and Moshe, S. (**2011**a). "Effect of seawater concentration on the productivity and nutritional value of annual Salicornia and perennial Sarcocornia halophytes as leafy vegetable crops." *Scientia Horticulturae*, 128(3): 189–96.

Yvonne, V., Wegi, A. W., Muki, S., Tzachi, M. S., Brandon, C. K., Shabtai, C., Zion, S., Rui, S., and Moshe, S. (**2011**b). "Effects of day length on flowering and yield production of Salicornia and Sarcocornia species." *Scientia Horticulturae*, 130(3): 510–6.

A Mooring

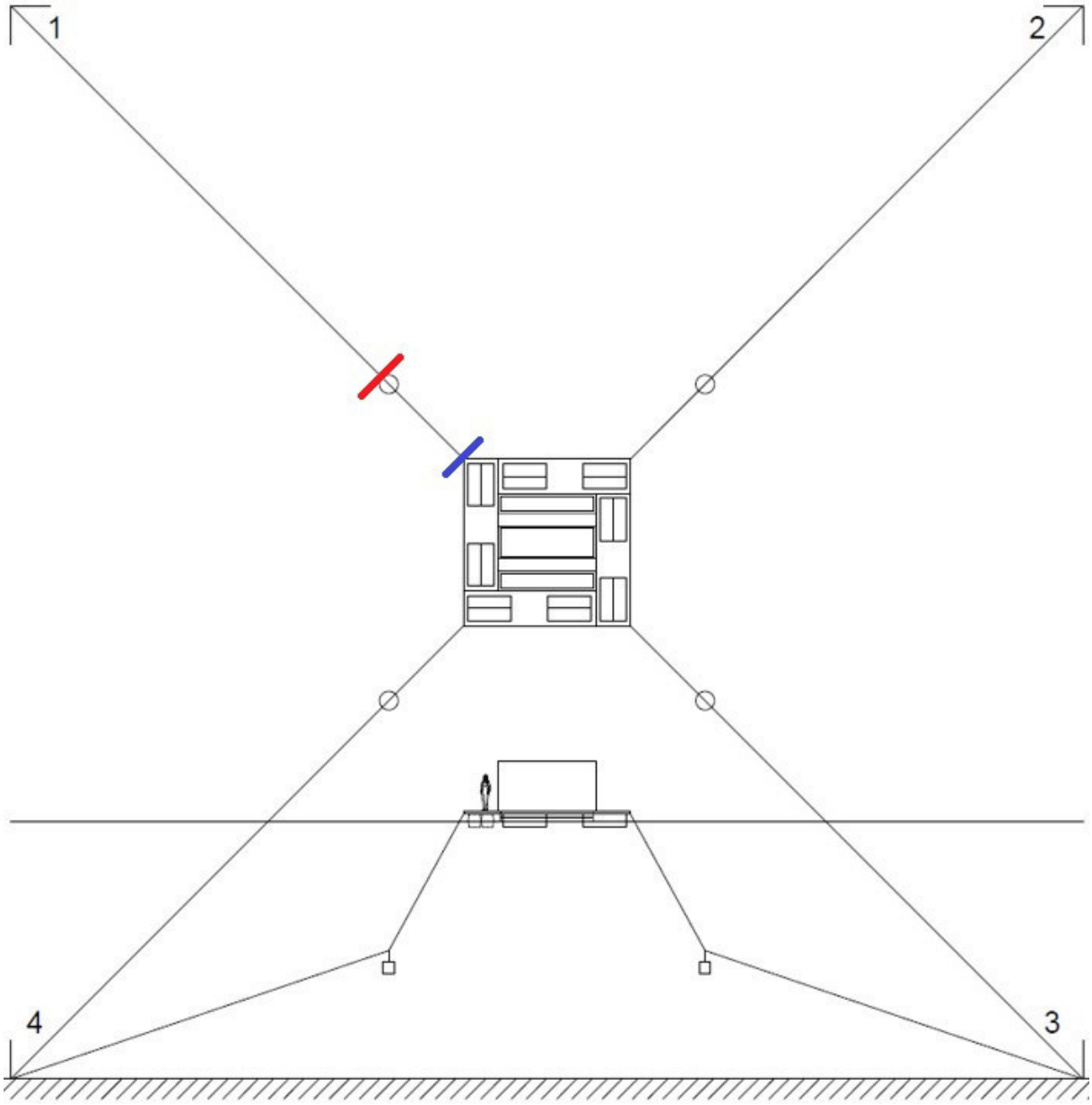

Figure A.1: The top- and side view of the clump-weigh mooring system. The footprint is a square area of 50 m x 50 m, indicated by the anchors (arrows) at the end of the mooring lines attached at the four corners of the arrangement. The round objects depict the clump-weights and their position. The red and blue marks show where the mooring line forces are measured in each mooring line

B HydroD Drag Coefficients

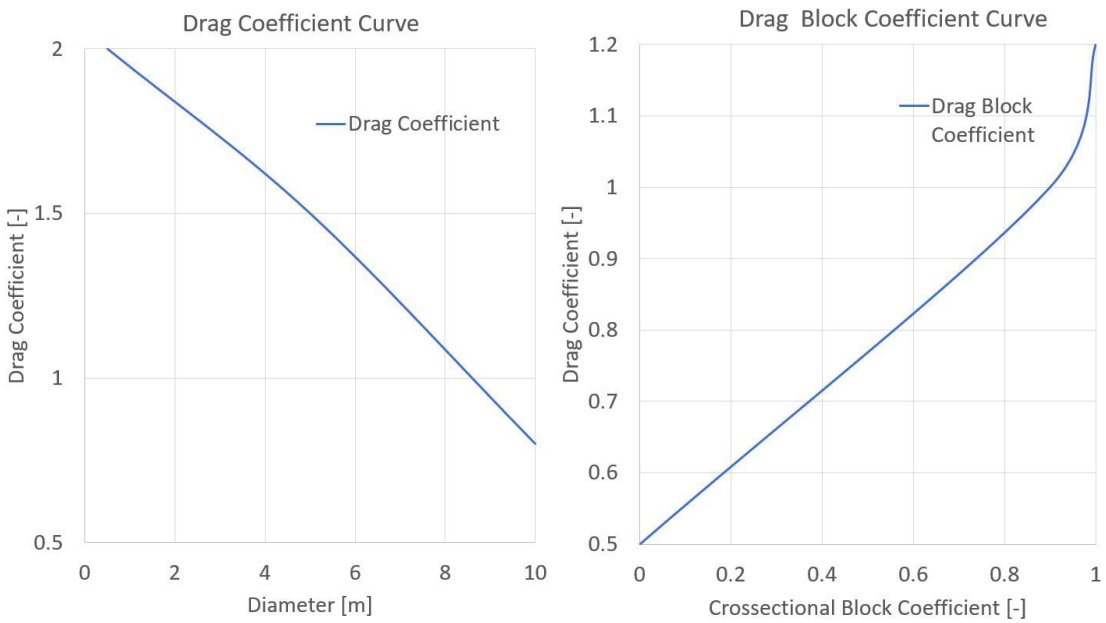

Figure B.1: The two graphs depict the default drag- and block drag coefficient curve as it is used in the HydroD intact stability wizard. The default is chosen since there is no knowledge of the drag characteristics of the structure

C RAOs in Heave, Roll and Pitch

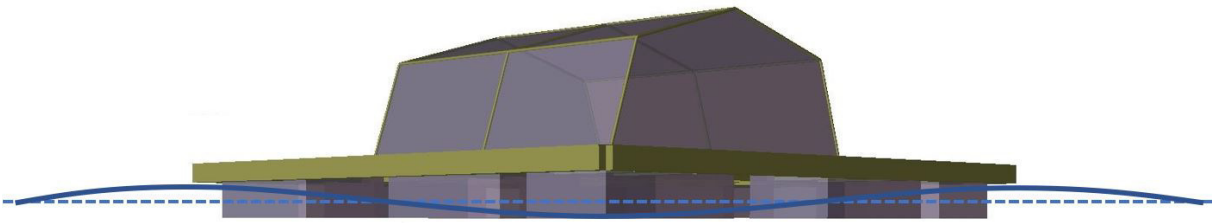

Figure C.1: The side view of the structure shows how the floater arrangement resembles the example case in figure 13.4 in section 13.1

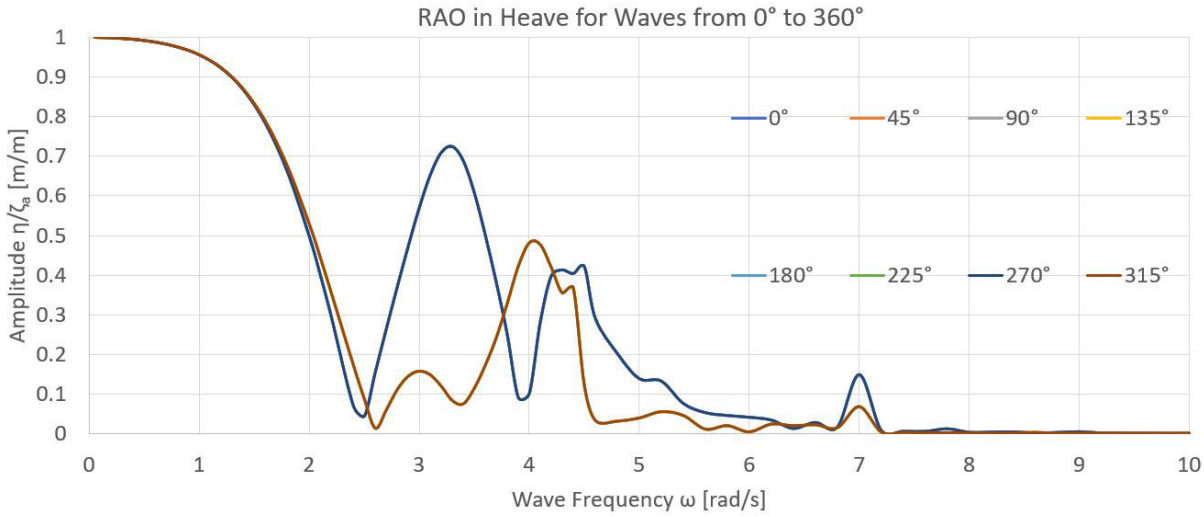

Figure C.2: RAO_{33} for waves coming from a 0° to a 360°-heading. The structure's response distinguished only between waves coming onto the sides of the structure and the waves coming onto the diagonal.

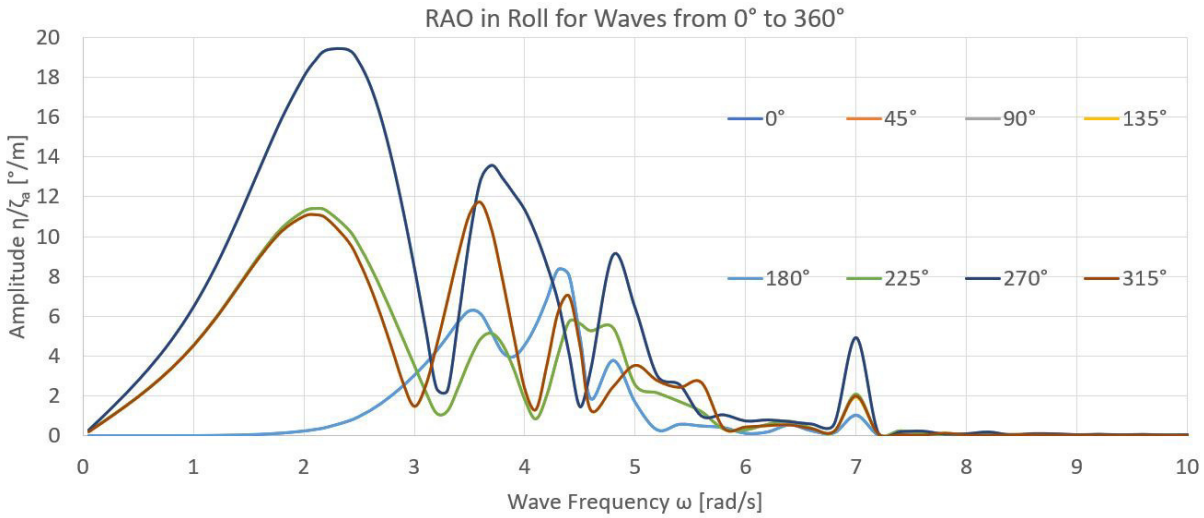

Figure C.3: RAO_{44} for waves coming from a 0° to a 360°-heading. Only the RAOs from wave directions opposing each other are identical, e.g. 0° and 180° and 45° an 225°

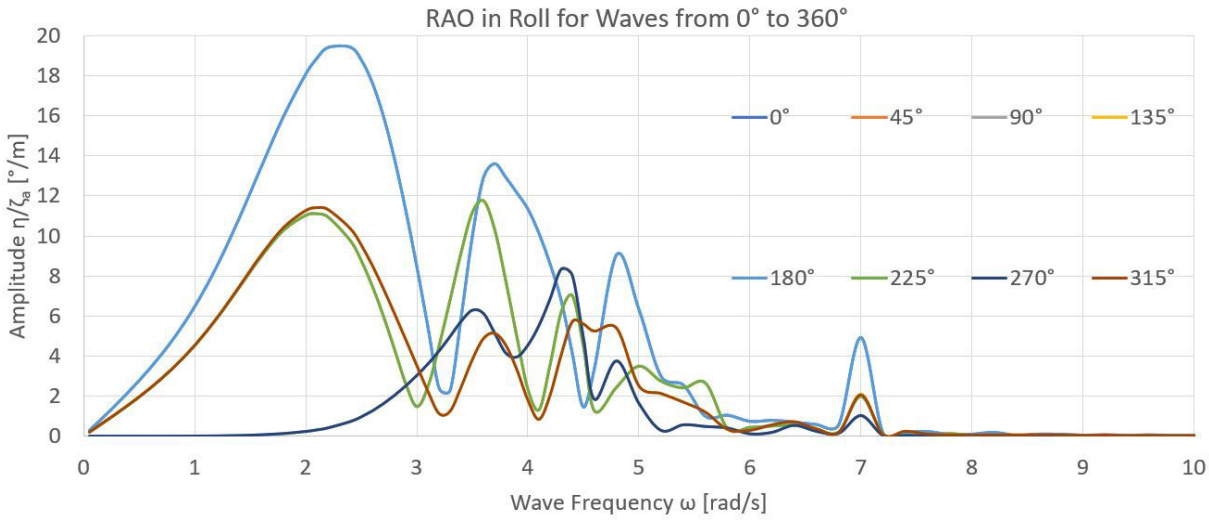

Figure C.4: RAO_{55} for waves coming from a 0° to a 360°-heading. Only the RAOs from wave directions opposing each other are identical, e.g. 0° and 180° and 45° an 225°. The difference to RAO_{44} is that the RAO_{55} is 90° phase shifted to RAO_{44}

D Simulation Time Series and Spectral Results

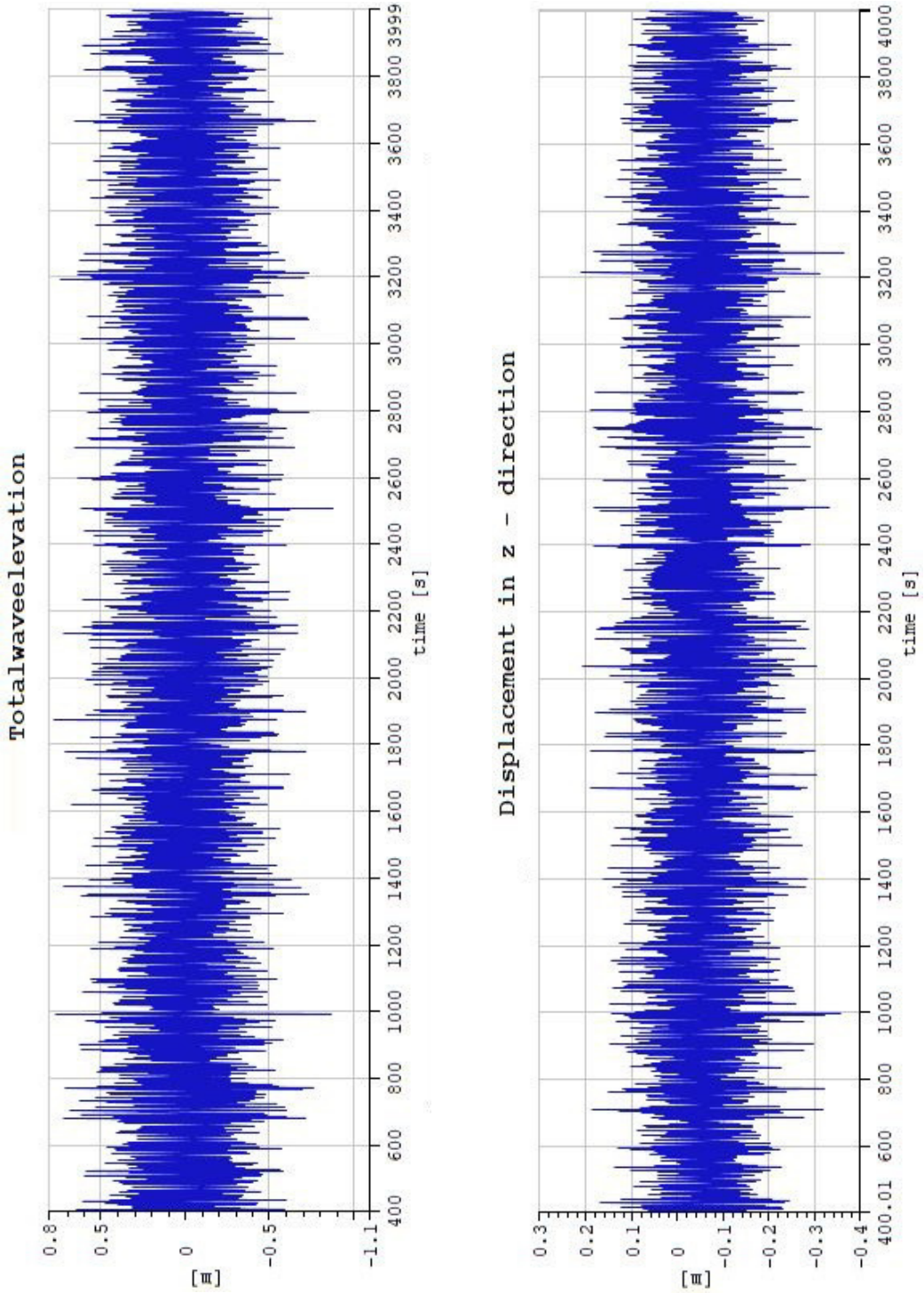

Figure D.1: The full TDS omitting the transient phase (0s − 400s) is presented for the wave elevation (left) and heave motion of the structure (right) in the survival condition

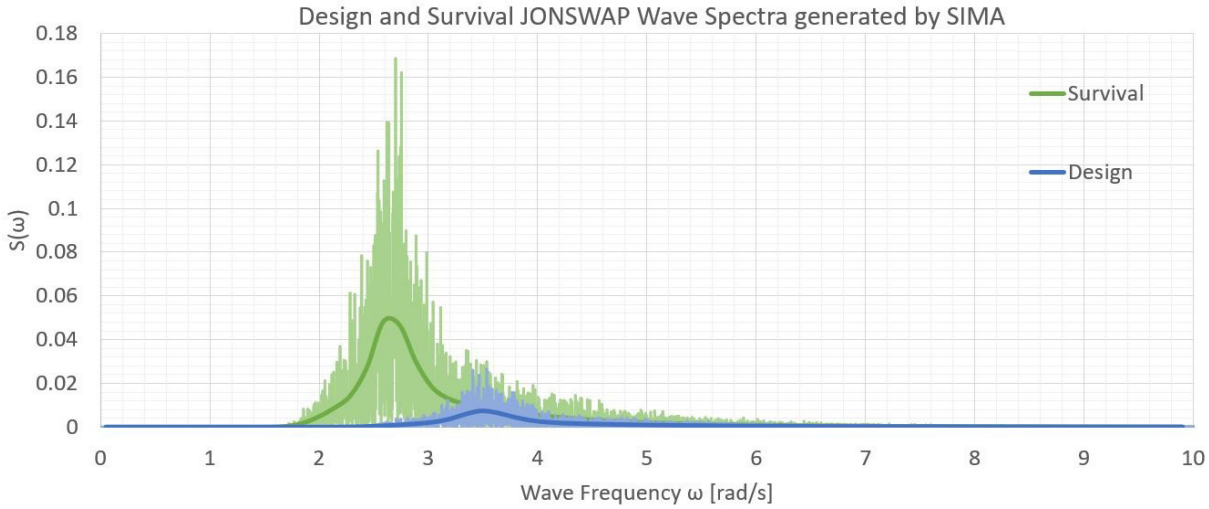

Figure D.2: Comparison of the design and survival JONSWAP wave spectra as are generated by SIMO

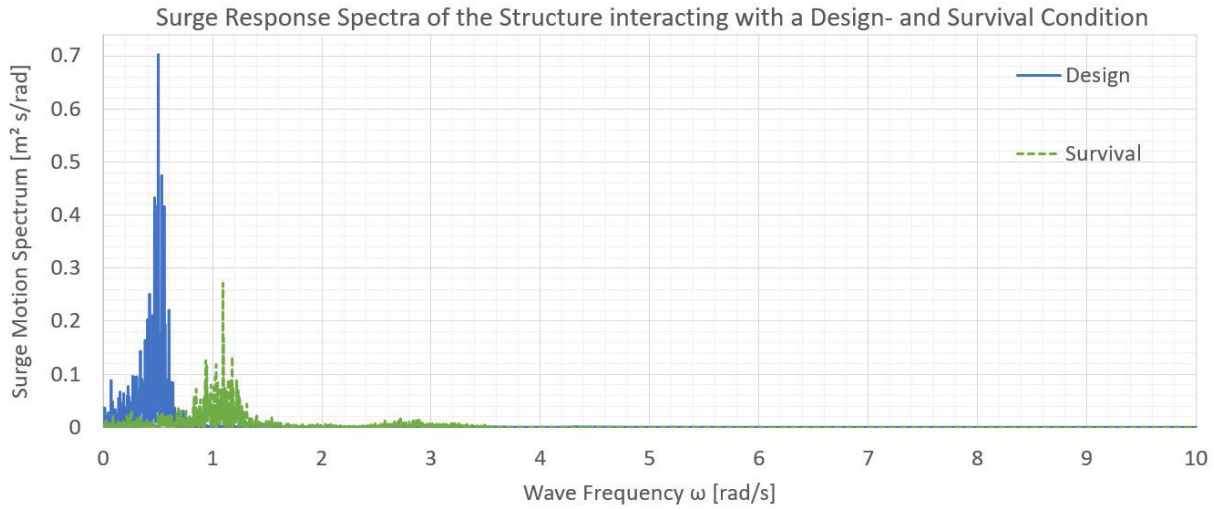

Figure D.3: The surge response spectra for the structure interacting with the design- (blue-solid) and the survival condition (green-dashed)

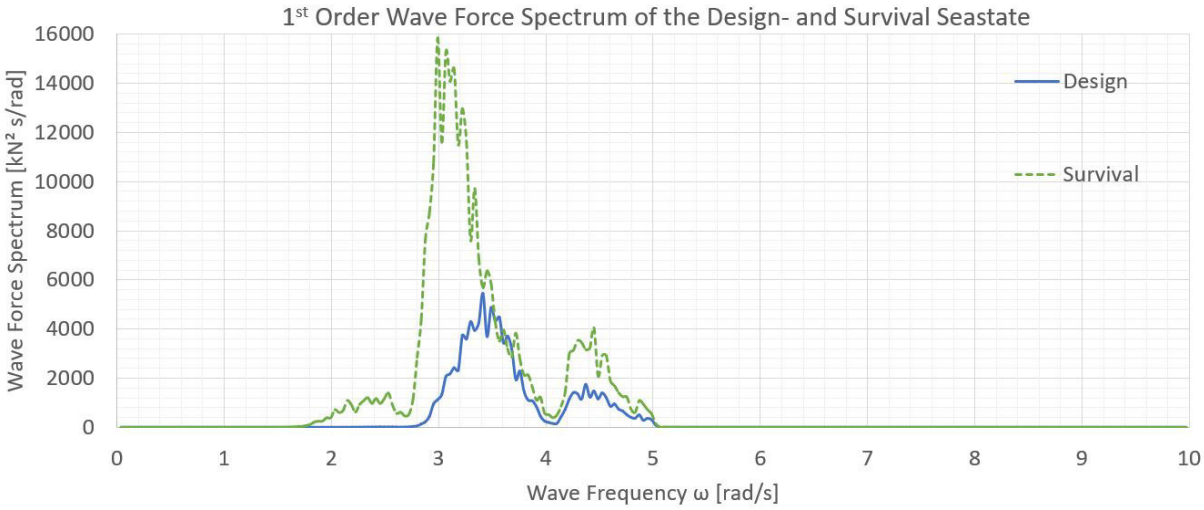

Figure D.4: Comparison between the first order wave forces of the design- (blue-solid) and the survival seastate (green-dashed)

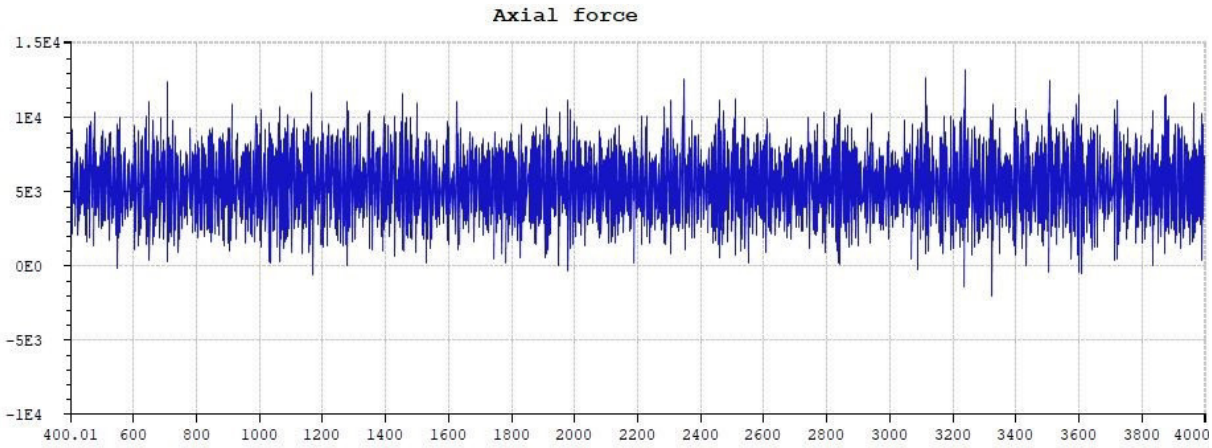

Figure D.5: Full time series of the line tension in mooring line 3 interacting with the survival condition

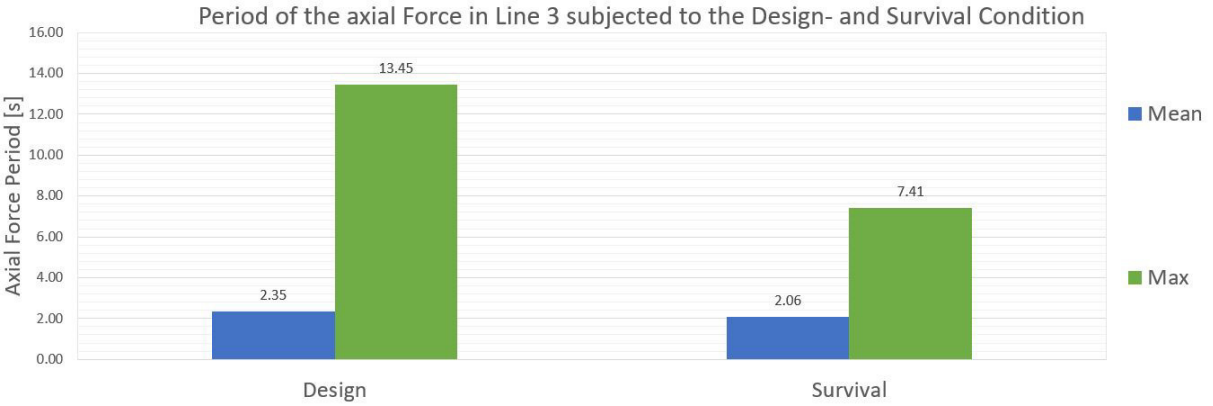

Figure D.6: The mean- and maximal period of the axial force in fairlead 3 subjected to the design- and survival condition

E Operability

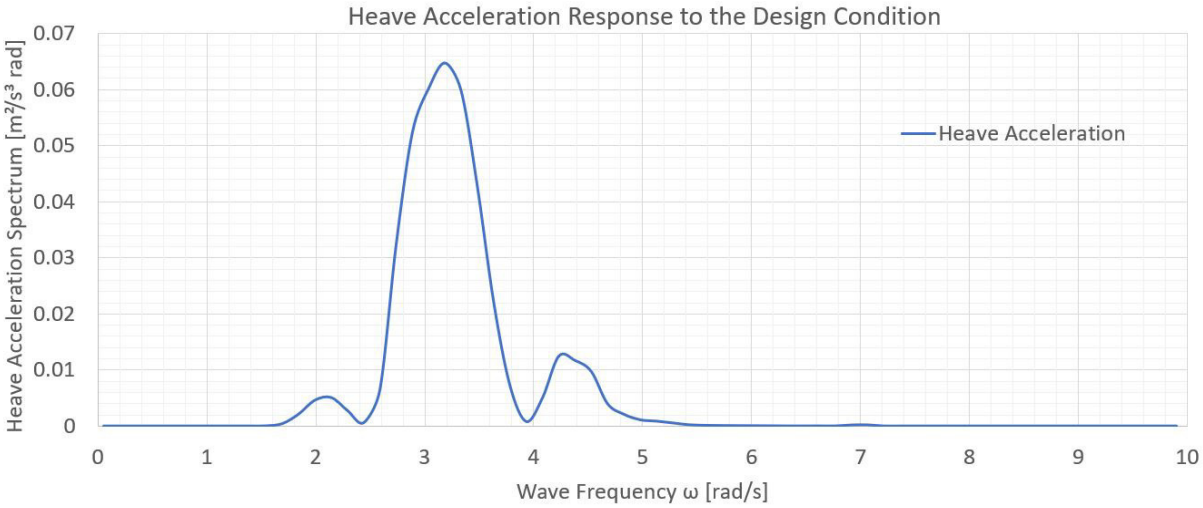

Figure E.1: The heave acceleration spectrum of the structure subjected to the survival condition

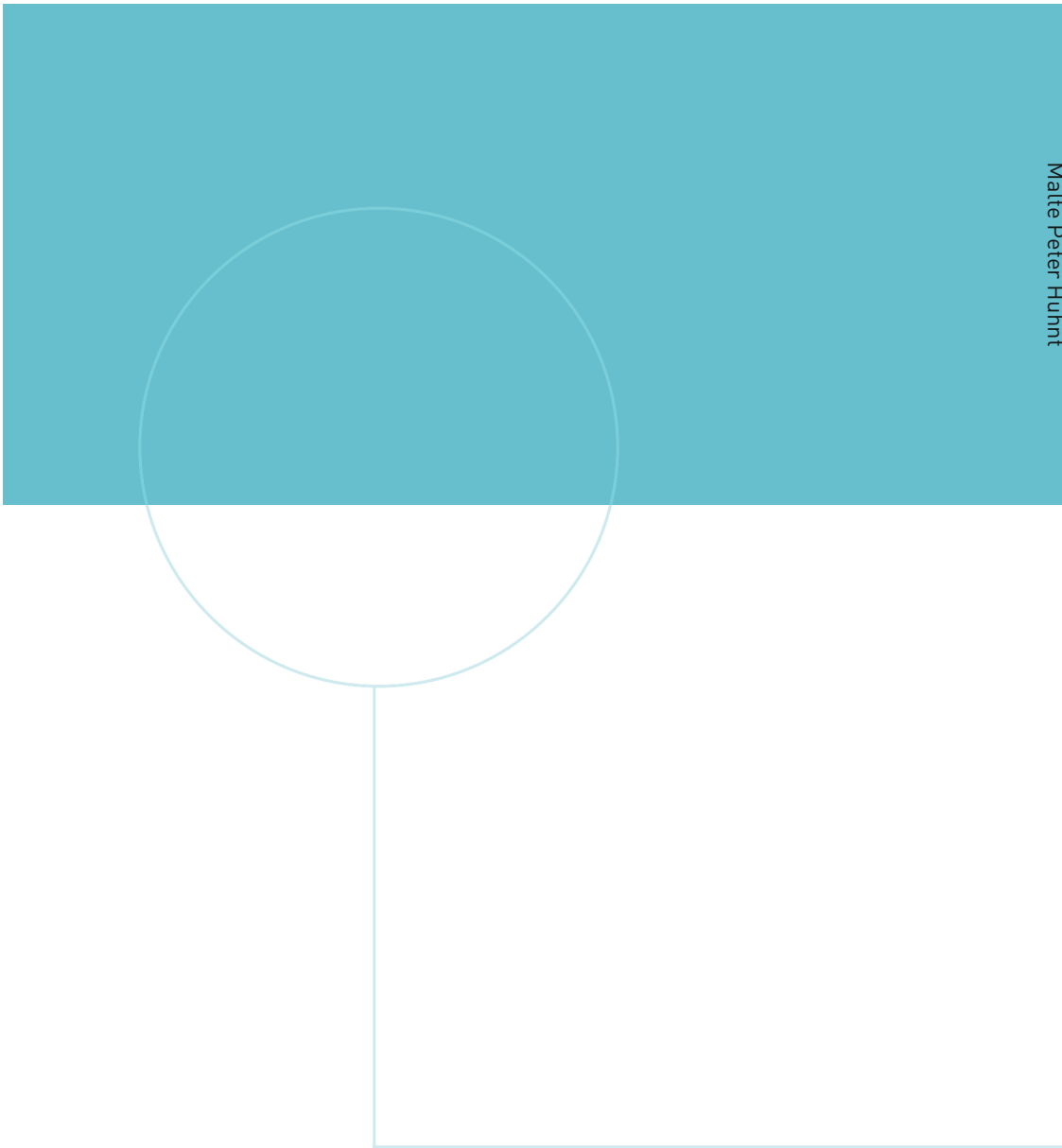

Malte Peter Huhnt

NTNU
Norwegian University of
Science and Technology